

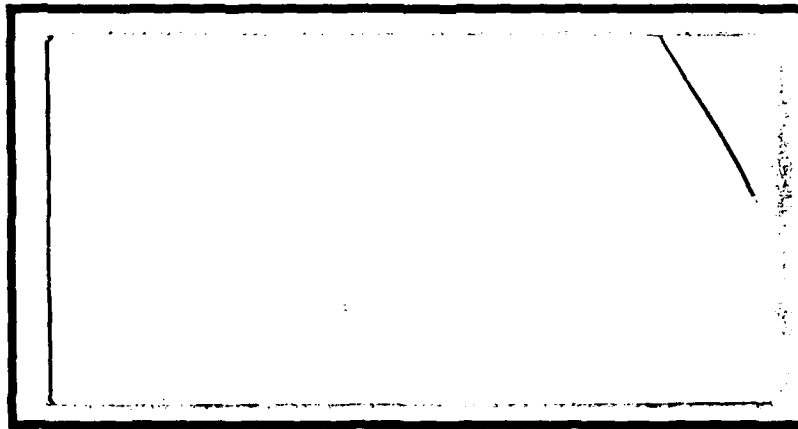
DTIC FILE COPY

1

AD-A202 617



DTIC  
 ELECTE  
 JAN 18 1989  
 S & H D



DEPARTMENT OF THE AIR FORCE  
 AIR UNIVERSITY

**AIR FORCE INSTITUTE OF TECHNOLOGY**

Wright-Patterson Air Force Base, Ohio

**DISTRIBUTION STATEMENT A**  
 Approved for public release  
 Distribution Unlimited

89 1 17 008

①

AFIT/GAE/AA/88D-7

DAMAGE INITIATION IN TWO-DIMENSIONAL,  
WOVEN, CARBON-CARBON COMPOSITES

THESIS

James C. Dendis  
Captain, USAF

AFIT/GAE/AA/88D-7

DTIC  
ELECTE  
S JAN 18 1989 D  
QH

Approved for public release; distribution unlimited.

AFIT/GAE/AA/88D-7

DAMAGE INITIATION IN TWO-DIMENSIONAL,  
WOVEN, CARBON-CARBON COMPOSITES

THESIS

Presented to the Faculty of the School of Engineering  
of the Air Force Institute of Technology  
Air University  
In Partial Fulfillment of the  
Requirements for the Degree of  
Master of Science in Aeronautical Engineering

James C. Dendis, B.S.

Captain, USAF

December 1988

Approved for public release; distribution unlimited

Table of Contents

	Page
Preface . . . . .	ii
List of Figures . . . . .	iv
List of Tables . . . . .	viii
Abstract . . . . .	ix
I. Introduction . . . . .	1
a. Motivation . . . . .	1
b. Purpose . . . . .	4
c. Material Description . . . . .	5
d. Background . . . . .	13
II. Theory . . . . .	21
a. Failure Criteria . . . . .	21
b. Finite Elements and Damage Initiation . . . . .	30
III. Experimentation . . . . .	41
a. Objective . . . . .	41
b. Specimen Preparation . . . . .	41
c. Test Equipment . . . . .	44
d. Test Procedure . . . . .	49
IV. Results and Discussion . . . . .	53
a. Maximum Load Test Results . . . . .	53
b. Finite Element Predictions . . . . .	64
c. Incremental Load Test Results . . . . .	72
V. Conclusions and Recommendations . . . . .	84
Bibliography . . . . .	88
Appendix A: NASTRAN™ Input File for L/d = 4 Model . . . . .	91
Appendix B: Failure Criteria Section of the L/d=4 Model Post Processor FORTRAN Code . . . . .	93
Appendix C: Experiment Raw Output Data . . . . .	95
Vita . . . . .	118

<input checked="" type="checkbox"/>
<input type="checkbox"/>
<input type="checkbox"/>
<input type="checkbox"/>
<input type="checkbox"/>



Availability Codes	
Dist	Avail and/or Special
A-1	.

## Preface

This study experimentally and analytically examines the phenomena of failure initiation in 3-Pt bend specimens of Advanced ACC-4 Carbon-Carbon composite material. Carbon-Carbon composites are emerging as a modern substitute for high temperature "super alloys" currently used in hot sections of today's jet engines. Because failure of the jet engine frequently leads to loss of the aircraft in military jet fighters, applications of Carbon-Carbon composites will depend on our ability to predict how and why parts made from such material will fail. This knowledge can then be used to design fail-safe parts that will be able to take advantage of the attractive properties of such an exotic material.

In any research project, many individuals offer their time and talent to help the author accomplish the task, and this one is no exception. I'm especially grateful to Mr Ted Fecke, my sponsor, who provided the material and motivation for this study. I'm also indebted to Major Paul Copp, my advisor, for his patience, enthusiasm, guidance and insight that made this thesis a reality. And I wish to thank: Dr N. J. Pagano, for his valuable input in the selection of this topic; Mr Jay Anderson, for everything associated with the Instron tester and the AFIT labs; Major John Mol, for his ideas on the test fixture; Mr Scott Theibert and company for their expertise and material support; Major Joe Hager,

for lessons in microphotography; Mr Bob Lewis, for explaining "correct" specimen preparation and micrographing; Mr Rick Bacon for SEM photos, and Dr A. Jackson for the image scanner.

Finally, I especially want to thank Dale and Karen Cope, whose friendship helped maintain my perspective and sense of humor throughout the past eighteen months. I really couldn't have made it this far without you.

## List of Figures

Figure	Page
1. The 8-Harness Satin Weave . . . . .	7
2. SEM Micrograph of Typical Polished Cross- Section, $L/d = 4$ (25x) . . . . .	8
3. Optical Micrograph of Typical Polished Cross- Section (200x) . . . . .	9
4. Typical SEM Photos of Polished Edge (50x) . . . . .	12
5. Close-up of Weave Geometry at Edge (100x) . . . . .	12
6. Shear Stress $\sigma_{xz}$ (psi), $N = 100$ , $P = 100$ lbs, $L/d = 4$ . . . . .	36
7. Normal Stress $\sigma_z$ (psi), $N = 100$ , $P = 100$ lbs, $L/d = 4$ . . . . .	36
8. Copp's Exact Shear Stress Distribution (4), $c/h = .25$ , $L/h = 2.0$ . . . . .	37
9. Copp's Exact Normal Stress Distribution (4), $c/h = .25$ , $L/h = 2.0$ . . . . .	38
10. Shear Stress $\sigma_{xz}$ (psi), $N = 500$ , $P = 100$ lbs, $L/d = 4$ . . . . .	39
11. Normal Stress $\sigma_z$ (psi), $N = 500$ , $P = 100$ lbs, $L/d = 4$ . . . . .	39
12. Left Half of Finite Element Model, $L/d = 4$ . . . . .	40
13. Test Specimen Cutting Pattern . . . . .	43
14. Experimental Fixture Diagram . . . . .	47
15. Equipment Schematic . . . . .	48
16. Steel Beam Load-Displacement Curve, Test Case . . . . .	52
17. Test Results, Maximum Load vs. $L/d$ Ratio . . . . .	54
18. Top Ply Fracture, $L/d = 15$ , $R = 100\%$ , (100x) . . . . .	56

19.	Top Ply Fracture Under Indenter, L/d = 5, #4, R = 100%, (100x) . . . . .	57
20.	(a) Pre-Failure, Top Ply Fracture, Indenter Contact Zone, L/d = 15, #3, R = 100%, (50x) . . .	58
20.	(b) Post-Failure, Top Ply Fracture, Indenter Contact Zone, L/d = 15, #3, R = 100%, (50x) . . .	58
21.	(a) Indenter Contact Zone, <u>Front Face</u> , L/d = 15, #2, R = 100%, (200x) . . . . .	59
21.	(b) Indenter Contact Zone, <u>Back Face</u> , L/d = 15, #2, R = 100%, (100x) . . . . .	59
22.	(a) 3/16" Right of Center at N.A., <u>Front Face</u> , L/d = 15, #2, R = 100%, (50x) (no cracks) . . .	61
22.	(b) 3/16" Left of Center at N.A., <u>Back Face</u> , L/d = 15, #2, R = 100%, (100x) (cracked) . . .	61
23.	(a) Cracks Beneath Top Ply, 3/16" Left of Center, L/d = 5, #4, R = 100%, (100x) . . . . .	62
23.	(b) Close-up on Center of Figure 23 (a) above, (400x) . . . . .	62
24.	Shear Stress $\sigma_{xz}$ (psi), Carbon-Carbon, N = 500, R = 100%, L/d = 4 . . . . .	65
25.	Normal Stress $\sigma_z$ (psi), Carbon-Carbon, N = 500, R = 100%, L/d = 4 . . . . .	65
26.	Tsai-Wu Failure Criteria, L/d = 4, R = 100% . . .	67
27.	Tsai-Hill Failure Criteria, L/d = 4, R = 100% . .	67
28.	Copp's Exact Elasticity Solution Tsai-Hill Failure Contour (4) . . . . .	68
29.	Tsai-Wu Failure Criteria, L/d = 15, R = 100% . .	69
30.	Tsai-Hill Failure Criteria, L/d = 15, R = 100% .	69
31.	Experimental and Finite Element Load vs Displacement Curves, L/d = 4 . . . . .	71
32.	Tsai-Wu Failure Criteria, L/d = 4, R = 70% . . .	73
33.	Tsai-Hill Failure Criteria, L/d = 4, R = 70% . .	73
34.	Tsai-Wu Failure Criteria, L/d = 4, R = 50% . . .	74

35.	Tsai-Hill Failure Criteria, L/d = 4, R = 50%	74
36.	Tsai-Wu Failure Criteria, L/d = 15, R = 85%	75
37.	Tsai-Hill Failure Criteria, L/d = 15, R = 85%	75
38.	Outer Ply Fracture at Right Support Pin, L/d = 4, R = 45% (200x)	79
39.	Initial Cracks at N.A., 1/4" Right of Center, L/d = 4, R = 54% (400x)	80
40.	Outer Ply Fracture at Right Support Pin, L/d = 4, R = 72% (100x)	81
41.	Crack in N.A. Layer, 1/4" Right of Center, L/d = 4, R = 72% (400x)	82
42.	SM-1000 Load Cell Calibration Curve	96
43.	RH 225A-300 LVDT Calibration Curve	97
44.	Load-Displacement Curve, Specimen 2/4-1, R=100%	98
45.	Load-Displacement Curve, Specimen 2/4-2, R=100%	99
46.	Load-Displacement Curve, Specimen 2/4-4, R=100%	100
47.	Load-Displacement Curve, Specimen 2/4-5, R=100%	101
48.	Load-Displacement Curve, Specimen 2/4-3, R=50%	102
49.	Load-Displacement Curve, Specimen 2/4-3, R=60%	103
50.	Load-Displacement Curve, Specimen 2/4-3, R=80%	104
51.	Load-Displacement Curve, Specimen 2/4-3, R=100%	105
52.	Load-Displacement Curve, Specimen 2/5-1, R=100%	106
53.	Load-Displacement Curve, Specimen 2/5-3, R=100%	107
54.	Load-Displacement Curve, Specimen 2/5-4, R=100%	108
55.	Load-Displacement Curve, Specimen 2/5-5, R=100%	109
56.	Load-Displacement Curve, Specimen 2/5-2, R=50%	110
57.	Load-Displacement Curve, Specimen 2/5-2, R=60%	111
58.	Load-Displacement Curve, Specimen 2/5-2, R=80%	112

- 59. Load-Displacement Curve, Specimen 2/5-2, R=100% . 113
- 60. Load-Displacement Curve, Specimen 2/15-1, R=100%. 114
- 61. Load-Displacement Curve, Specimen 2/15-2, R=100%. 115
- 62. Load-Displacement Curve, Specimen 2/15-3, R=100%. 116
- 63. Load-Displacement Curve, Specimen 2/15-4, R=100%. 117

List of Tables

Table	Page
1. Elastic Properties of ACC-4 . . . . .	11
2. Average Yield Strengths of Uncoated ACC-4 (23) . .	11
3. Equipment List . . . . .	45
4. Pmax Test Results Summary . . . . .	53
5. Experimental and Finite Element Maximum Displacements . . . . .	70
6. Incremental Load Test Reversal Points, L/d = 4 .	77
7. Incremental Load Test Reversal Points, L/d = 5 .	77

## ABSTRACT

The Air Force and its prime contractors are currently investigating the use of advanced Carbon-Carbon (C/C) composite materials to build critical jet engine components which must operate under very high temperatures. Catastrophic structural failures of these combustor and turbine parts (a turbine blade for example) usually destroys the rest of the engine. Typically, the engine casing can rupture causing fires and perhaps the loss of the aircraft. The serious consequences of such failures require a thorough understanding of the damage mechanisms of the material used in such critical parts, so that designs may avoid, or at least minimize the consequences of component failures.

C/C composites possess a tensile modulus about 40 times the value of the shear modulus. Thus shear failures are of primary concern in designs using this material. Experimental and analytical investigation of the damage initiation under tensile loads usually follows standard tensile tests used to generate material properties data, a reasonable sequence of events given that tensile failures of two-dimensional C/C composites are not greatly different from tensile failures of other fiber-reinforced composites. However, the engineering community agrees that "standard" experiments for measuring shear strength in C/C composites produce widely varying results, partly because of varying

failure modes achieved in such tests. Since many researchers use the ASTM-2344 "Apparent Interlaminar Shear" bend test to generate shear property data, this thesis examines damage initiation in C/C resulting from this three-point bend test. Specifically, this thesis contributes to the understanding of shear failures in C/C by experimentally investigating damage initiation in fourteen two-dimensional, woven, warp aligned C/C beams. Failure load and damage indications were recorded on load versus mid-span displacement curves. The specimens were photographed under high magnification (micrographed) for pre- and post-test comparisons of the cross-section of the laminate. Only a few of these micrographs appear in this document because of the limited space. Approximately 200 photos were obtained through either an optical or Scanning Electron Microscope (SEM) in the course of this investigation and are on file with the department. These experiments show that three point bend failures of C/C composites are complex and the cracks are three dimensional in nature. In all our specimens, the outer ply fractured at the contact points before any internal damage was detected, and this fracture occurred at as little as fifty percent of the ultimate load. Following the outer ply failures, internal cracks formed simultaneously in the second layer plies around the contact region, and in the plies bracketing the neutral axis of the beam. In short span beams, the

cracking spreads to other plies between the neutral axis and the contact points while in the long span beams, cracking remains generally confined to these initiation areas but widen and lengthen much more than cracks in the short span specimens.

In addition, a NASTRAN™ finite element model was developed and used in a linear elastic analysis to predict model stress fields. These stresses were analyzed with both the Tsai-Wu and Tsai-Hill combined stress failure criteria to predict damage initiation sites and loads in the test specimens. Results show that a simple linear finite element analysis of the specimens can be used to predict failure initiation when the stress field is evaluated using one of these combined stress field failure criteria. Finite Element Analysis also shows that the linear model predicts displacements within only four percent of the experimentally measured displacements, up to the ultimate load, despite the extensive cracking observed in the actual test specimens.

The most significant recommendations are to study laminates other than the purely orthotropic lay-ups considered here, and to investigate parametrically the effects of significant variances in strength and material properties. Also, additional work with varying indenter sizes and load rates would be useful in determining how test equipment can influence test results.

Damage Initiation in Two Dimensional, Woven  
Carbon-Carbon Composites

I. Introduction

a. Motivation

The development of the airplane has always hinged on the development of a propulsion system capable of sustaining thrust many times its own weight. In fact, the Wright brothers were the first to succeed in powered flight because they realized commercially available engines at that time were unsuitable, and built their own high horsepower-to-weight engine which powered the first Wright Flyer. Even today, the high speed and vertical climb capabilities of modern fighters are due to the modern turbofan engine and its 25/1 thrust to weight ratio. According to Project Forecast II predictions, future military aircraft will need even higher thrust-to-weight engines to reduce size and increase payload.

Currently, jet engine thrust and efficiency are usually limited by the maximum tolerable temperature of the turbine and associated structures immediately downstream of the

combustion chambers. Combustion temperatures are high enough to literally melt the downstream engine components and must be limited through elaborate flow controls and structural cooling mechanisms. Limiting the maximum combustion temperature limits the amount of energy which can be added to the flow in the combustion process and thus limits the efficiency and net thrust of the engine.

In an attempt to remove or reduce such limitations, scientists and engineers are currently developing new, light weight materials that will withstand higher temperatures than the metal superalloys used in current designs. High temperature ceramics and carbon-carbon (C/C) composites represent two such materials. Both offer increased engine efficiency through higher sustainable temperatures, decreased weight and reduced dependency on foreign sources for various metal superalloys (21:1,95). Ceramics however are too limited by their low fracture toughness and sensitivity to surface defects for current structural applications. Use of Carbon-Carbon composites promises greater success due to a lower density and higher fracture toughness than ceramics. C/C composites also offer a high strength-to-weight ratio, variable material response through variable stacking sequences, high corrosion resistance, and low notch sensitivity. Additionally, carbon is abundant worldwide and easier to obtain than most metal superalloys.

However, C/C composites exhibit a number of serious material limitations including: low resistance to high temperature oxidation, low interlaminar strengths (< 1500 psi), and low strain to failure (< 1%). These materials also require weeks or months of processing to manufacture and cost 20-50 times conventional composites like graphite/epoxy.

Research in chemical coatings continues to address the oxidation problem, and if successful, could lead to wide spread use of C/C structures where low shear strength and failure strain are not a concern such as in limited life (i.e. cruise missile) engines or static components such as combustors and nozzle flaps/seals (9:1). In fact, despite its material limitations, C/C composites have already found applications in space shuttle and reentry vehicle nosetips and leading edges, solid fuel rocket nozzles and exit cones, bearings, and especially in aircraft disk brakes (13:294).

While there are many different types of Carbon-Carbon composites, this research effort is centered on one type intended for possible jet engine applications known as "ACC-4." Basic material properties of this material have been studied by several leading research agencies both in and outside the Air Force. Current research is now centered on possible applications of such a material, and the parameters associated with applications design, such as

failure modes and failure initiation.

b. Purpose

The purpose of this thesis is to experimentally and analytically investigate the damage and failure initiation characteristics of woven, Carbon-Carbon (C/C) composite beams. A version of the ASTM-2344 "Apparent Interlaminar Shear Strength" (three point bend) test will be used to induce damage in specimens with constant thickness and width but varying length in order to study the effects of length on failure initiation. The three point bend test is a common test used by manufacturers to evaluate material capability, and may not be the most ideal method of inflicting damage for a damage initiation study. However, since it is such a common industry test, studying the types of failures generated through this test will aid many others in interpreting similar standard test results. Photomicrographing the highly polished sides of the bend test specimens before and after the experiments will show where initial damage propagates to the outer surface and the amount of force required to cause such damage. Comparisons between the photographic evidence will be made among the various specimens and load conditions.

To compliment the experimental studies, an elastic finite element analysis will generate an expected stress

field for the test specimens, which will be analyzed with two common combined-stress failure criterion to predict locations of damage initiation and the associated load. Stress and failure criteria contours will be generated and compared to micrographs of actual test specimens to demonstrate model accuracy and the ability to predict failures.

All tests in this study will be conducted with uncoated C/C at room temperature to provide basic data for any others who may choose to study more complex cases of coated C/C at room and elevated temperatures.

#### c. Material Description

The material evaluated in this study is a modern version of a two-dimensional (2-D), woven C/C composite known as "ACC-4." Carbon-Carbon composites consist of mats of interwoven carbon fibers imbedded in a carbon matrix. In 2-D C/C, the fibers are woven perpendicularly and in-plane, running the length and width of the ply. Plies are then soaked in phenolic carbon resin, stacked in a particular sequence, and cured to form the basic laminate. Three-dimensional (3-D) C/C lay-ups have additional fibers typically running perpendicular to the 2-D weave plane which are usually "stitched" through the 2-D plies to increase interlaminar strength. As a result, 3-D laminates are

generally stronger and more isotropic than 2-D laminates, however, manufacturers generally prefer 2-D laminates because they are easier to produce. Therefore, studying 2-D instead of 3-D composites may have a wider range of interest and applicability.

The particular ACC-4 composite tested here employs high modulus, heat stabilized Union Carbide T-300 graphite fiber yarns and a HITCO SCI-0008 phenolic resin matrix (10). The yarns are woven into mats in a 8-harness satin weave pattern shown in Figure 1. Generally, the finished mats contain 24 warp yarns per inch and 23 fill yarns per inch making a highly orthotropic laminae. Twenty such mats are then saturated with the phenolic resin and stacked with all warp fibers parallel to form the symmetric, highly orthotropic laminate tested in this thesis. Following lay-up, the mats underwent five successive phenolic resin impregnation and pyrolysis cycles to densify and cure the laminate. According to Leong and Zimmer (13:9-13, 26-38), this process of successive reimpregnation and pyrolysis creates voids inside the laminate as the layers expand and contract under the thermal stress. Figure 2 is a Scanning Electron Microscope (SEM) photo at 25X of half of the polished cross-section which shows the large voids within the fill fiber layers. These voids are also evident in Figure 3, a 200X optical micrograph of a typical polished C/C cross-

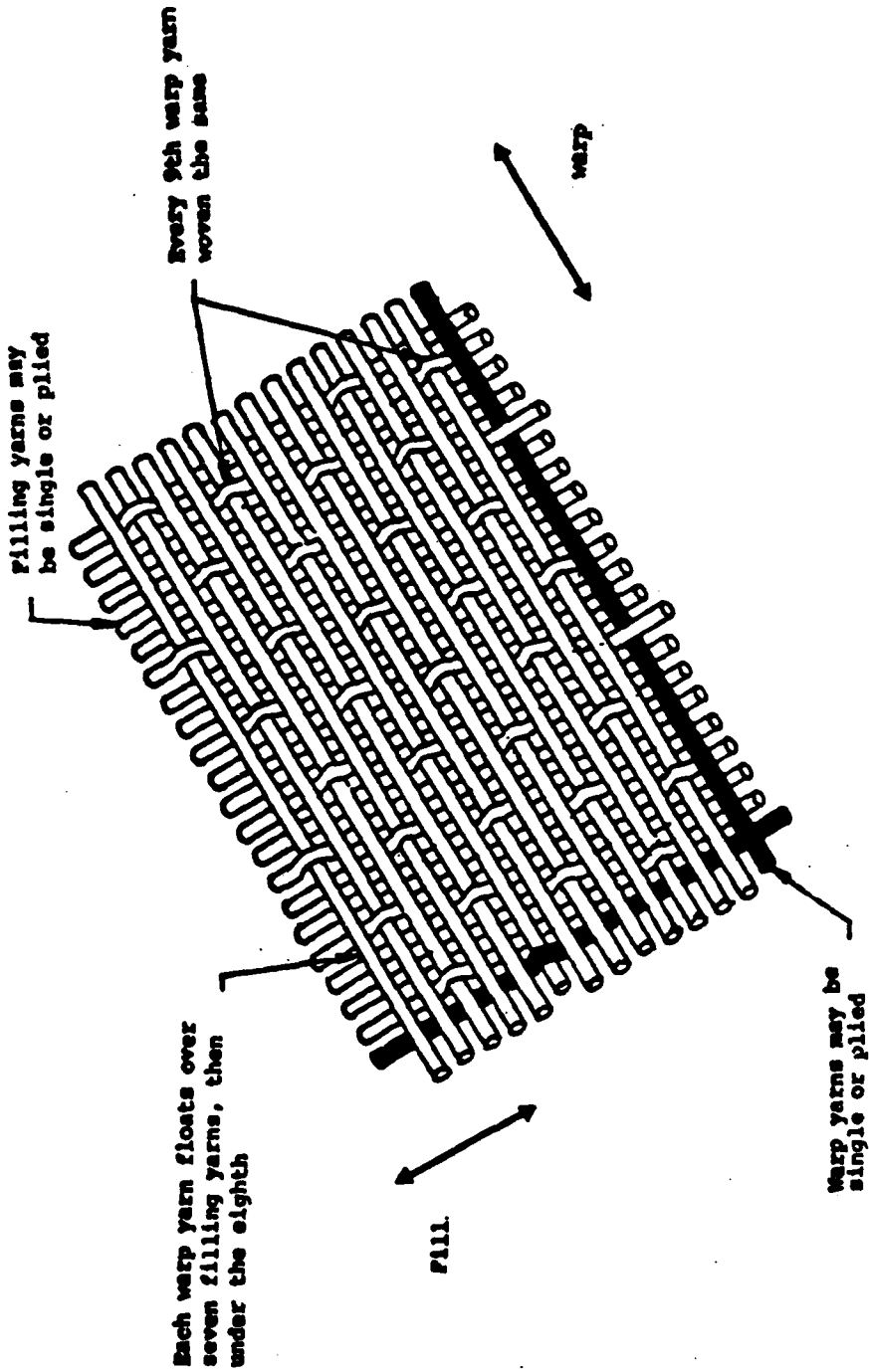


Figure 1. The 8-Harness Satin Weave

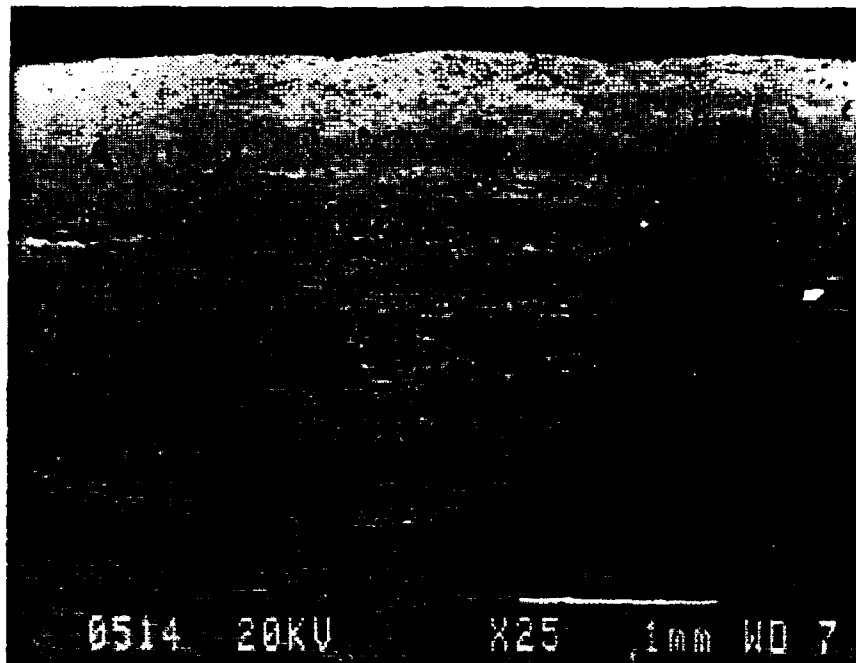


Figure 2. SEM Micrograph of Typical Polished Cross Section,  
L/d = 4, (25x)



matrix —  
warp fibers —

voids —  
fill fibers —

Figure 3. Typical Optical Micrograph of Polished Cross Section (200x)

section. Figure 3 also indicates the features common to all C/C micrographs and serves as a guide for interpreting other photos presented in this study. Figures 4 and 5 are additional SEM photos of the polished face and show the detail of the weave pattern of the laminate. The twenty ply cured laminate is nominally 0.22 inches thick for a final nominal ply thickness of 0.011 inches. The density of the cured laminate is about 1.6 gm/cc and its in-plane Poissons ratio is 0.05 at room temperature. The material properties for this version of ACC-4 are listed in Tables 1 and 2 below, and were supplied courtesy of Mr Scott Theibert and Mr Steve Szaruga of the Non-Metallic Materials branch, Air Force Materials Lab, and Mr Ted Fecke of the Air Force Aero-Propulsion Lab. They represent an average set of consistent properties compiled from contracted and in-house experimental investigations of this material over the past several years (6,10,19,20, & 23). It is understood that these material properties vary because of the complicated processing required to form the C/C laminate, and are often not constant within a particular raw billet of material.

This research assumes these values as material constants. No attempt was made to estimate the consequences of significant variances in these properties, primarily because results obtained using these values were accurate enough for the purpose of characterizing damage initiation.

Table 1. Elastic Properties of Uncoated ACC-4

$E_x$	$E_z$	$G_{xy}$ (msi)	$G_{xz}$	$\nu_{xy}$	$\nu_{xz}$
16	.45	.35	.20	.05	.20

Table 2. Average Yield Strengths of Uncoated ACC-4 (23)

Tensile		Compressive		Shear
$X_T$ (psi)	$Z_T$ (psi)	$X_C$ (psi)	$Z_C$ (psi)	S (psi)
48,000	550	26,000	25,000	1,000

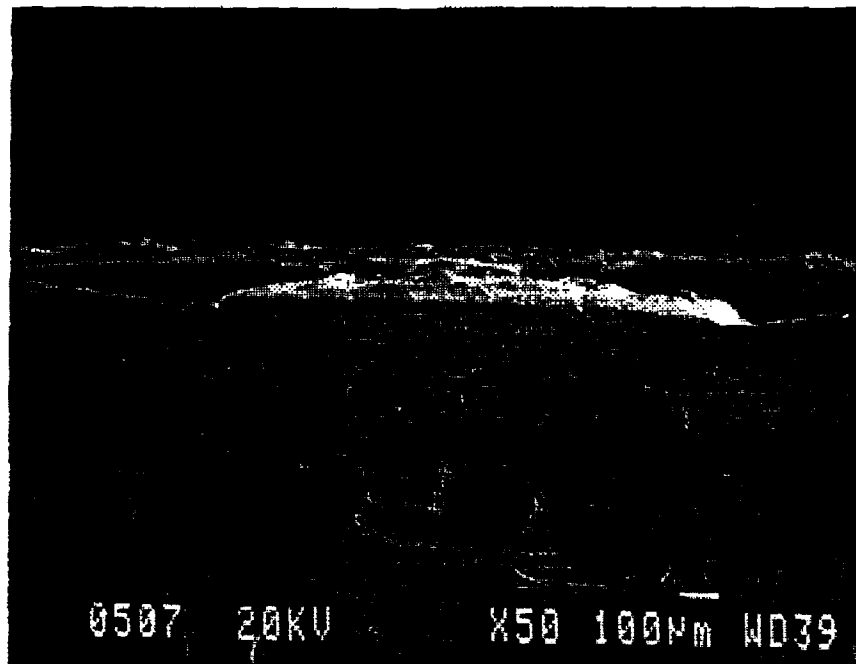


Figure 4. Typical SEM Photo of Polished Edge (50x)

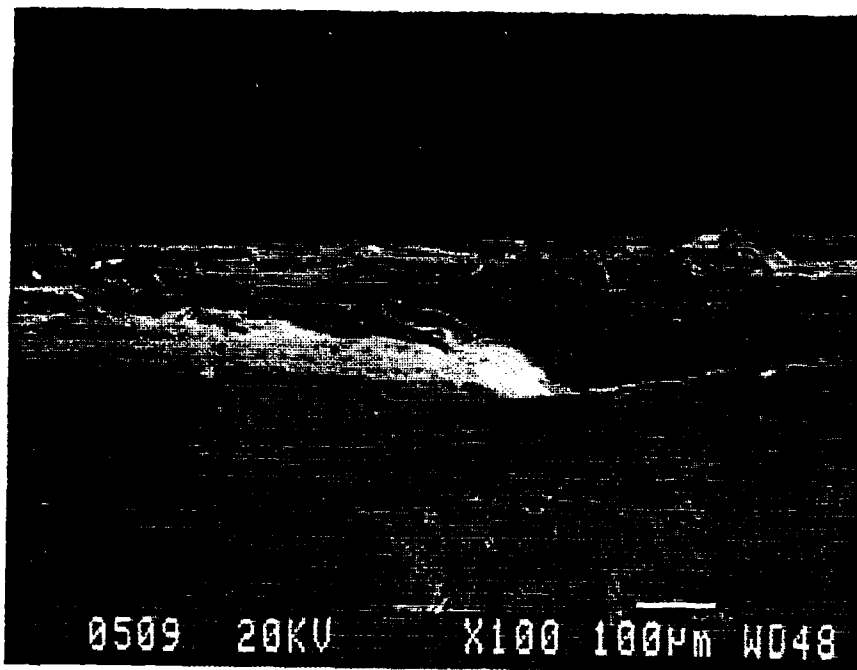


Figure 5. Close-up of Weave Geometry at Edge (100x)

#### d. Background

Many leading researchers in composites have studied exact and approximate solutions for composite materials in cylindrical bending which is analogous to the 3-Pt bend tests results investigated by this thesis. A summary of related historical works, some almost 50 years old, is presented for comparison to experimental and finite element results discussed in later chapters.

Lekhnitskii (8) was one of the first to develop a general elasticity theory for anisotropic material. His work was based on the Kirchoff assumption of no transverse shear deformation and was applicable only for small displacements, but it was the foundation of Classical Laminated Plate theory (CLPT). Ambartsumyan (1:75-82), a student of Lekhnitskii, noted that it's necessary to consider transverse shear deformations in CLPT analysis of orthotropic materials with a high  $E_{11} / G_{12}$  ratio (such as ACC-4). He incorporated these transverse shear effects as an approximate parabolic distribution in a plate theory developed for symmetric laminates where the laminae axes coincide with the plate axes.

Whitney (28:539-542) expanded this development to include symmetric laminates of arbitrary orientation with respect to the plate axes and applied the theory to a simply supported square laminate subject to static, transverse

load, like a laminate in three point bend. For this square plate, Whitney developed some numerical results for span/depth ratios of about 40, and  $E_{11} / E_{22}$  ratios of about 40 showing a 15% difference in predicted displacements between laminated plate "shear deformation theory" and CLPT. His results also show that this same 15% difference occurs at span/depth ratios of less than 10 for  $E_{11} / E_{22}$  equal to three. Note that this last result is similar to the  $L/d = 4$  ACC-4 case considered in this study.

Pagano (14:399) realized the limitations of Classical Laminated Plate Theory and acknowledged Whitney's approximate method of incorporating the influence of shear deformations on deflection. He developed exact linear elasticity solutions for several boundary value problems involving unidirectional and bidirectional layered anisotropic materials in bending. Based on the numerical results obtained with his solutions, Pagano concluded his stress distributions from the elasticity solution applied to both short ( $L/h = 4$ ) and long ( $L/h \geq 10$ ) beam bend specimens. He also noted that CLPT transverse stress approximations converge to the exact solution "more rapidly than its prediction for plate deflection." For comparison, Pagano computed shear stress distributions through the thickness of a symmetric, orthotropic composite beam with  $L/h$  ratios of four, six, and ten. These stress distribution

plots will be compared to stress distributions from a finite element model in later sections.

Pagano (15:331,341) also investigated the influence of shear coupling in bending of anisotropic laminates by comparing elasticity and CLPT solutions for simply supported beams under uniform loading. His results show that CLPT solutions still converge to the elasticity solutions, but that CLPT results are more than 10% from the elasticity solution for span-to-depth ratios of less than 20.

Pagano (16:521-528) studied composite beams in cylindrical bending even further by considering differences between uniform and concentrated loads expressed as a Fourier series expansion. Once again, he compared CLPT and elasticity solutions, but in this case, material properties representative of graphite/epoxy composites were assumed. The results of his study showed the CLPT solution underestimates by 100% the maximum deflection of a symmetric laminate beam with  $L/h$  equal to 10, under a concentrated load. This case is also similar to the material and loading conditions investigated here.

In an interesting experimental approach, Robinson (17:27-30) correlated observed damage to acoustic emissions from three point bend specimens of a cylindrical, 3-D Carbon-Carbon Composite. He stated that, in general, the reduction in load resistance caused by internal damage was

proportional to the level of acoustic emissions from the specimen under load. Robinson concluded that large emissions corresponded with fiber failures while smaller emissions indicated matrix failures, and thus more energy is released in fiber failures than matrix failures. He also noted that indications of damage were not visible on the specimen surface until the later stages of failure.

Rosensaft and Marom (18:12-16) evaluated the applicability of bending test methods to composite materials. They compared three- and four-point bend test results for Carbon, Kevlar, and Glass fiber reinforced composites. Of these three unidirectional materials, they concluded Carbon fiber reinforced composites behavior came closest to expected linear beam theory behavior. Rosensaft and Marom also noted that the predicted beam theory maximum shear stress from the bend tests is higher than the reported shear strength of the material. They also tested specimens with different fiber volume fractions and concluded that predicted shear stress values from bend specimens doesn't depend on this ratio.

Whitney and Dauksys (31:133-137) showed that material fiber alignment within the bend test specimens may be important in high  $E_{11} / E_{22}$  ratio composites since shear coupling causes off-axis specimens to twist and lift off the supports along the sides of the specimen. They reported

"shear coupling always causes the apparent bending modulus to be higher than the actual modulus," and that it could result in a difference between theoretical and measured quantities such as modulus. However, for the woven [  $0^\circ$ ,  $90^\circ$  ] material considered here, shear coupling could only result from improperly aligned fiber tows. Since the misalignment would be localized, and at most a few degrees, one expects the amount to be negligible and not affect experimental results.

Whitney and Browning (30:298-300) have characterized failures in three- and four-point bend test specimens of unidirectional graphite epoxy. In particular, their 50-ply,  $L/h = 4$ , three-point bend specimen is dimensionally similar to the  $L/d = 4$  C/C specimens tested in this thesis research. Based on microscopic examinations of the short test specimens, Whitney and Browning concluded that mixed mode (compression and shear) rather than pure shear failures occur in composite bend test specimens.

Recently, a relevant elasticity solution to the subject of this thesis appears to be Whitney's elasticity analysis of orthotropic beams under concentrated loads (29:177). Whitney analyzed models of thin (.08") and thick (.25") short beam shear specimens of  $L/d$  equal to four. His two dimensional solution uses a Fourier series to model applied and support loads along the beam, and hyperbolic functions

for stress distributions through the thickness. To allow computed stresses to reduce to zero at the end surfaces, he assumed a support pin overhang length of .50" or twice the thickness of the thick beam. Since his stress values are exactly zero at the top and bottom surface, the "large overhang" assumption permits him to satisfy all surface boundary conditions for the flexural and short beam shear tests. In addition, he demonstrates convergence of his Fourier series loading over 100 terms of the series. Whitney then generated some numerical examples using the converged series to illustrate the application of this theory, and plots a visual representation of the changing stress field within the short beam. According to this graph, the shear stress distribution is highly skewed at the load and support pin contact points which accurately reflects the effect of the concentrated load. He also shows compressive stresses at the same points are over twice the values at the neutral axis, and much larger than predicted by classical beam theory, especially for the thick beam. Despite his large overhang assumption, these results should apply to the experimental findings of this thesis, especially between the support pins where boundary condition assumptions about the end faces are least important. Whitney and Browning use this analysis in their experimental study mentioned earlier to explain some of their results

obtained with unidirectional composite beams. Through this analysis, they reasoned that "compression stresses in regions where high shear-stress components exist tend to suppress interlaminar shear failure modes" (30:300)

On the subject of numerically predicting failures, Whitney claims:

Numerical results indicate a very complex state of stress in the vicinity of the applied load where failure has been observed to initiate. Combined shear and compression stresses exist in this region with large gradients present (29:183).

indicating a combined or coupled failure criteria might be more appropriate than an individual or uncoupled criteria when analyzing stress fields to predict failure loads.

Copp (4:78) used a different approach and obtained similar results by developing an exact solution to the complex mixed boundary continuum mechanics equations with integral transforms. He analyzed the indenter contact problem with simply supported composite beams of differing fiber orientations. Specifically, an extensive parametric study of contact length, layer thickness, beam length, laminae orientation and support conditions was conducted. The resulting stress contours show the localized effects of the indenter and the support pins, as well as the far-field or global beam response. Copp applied the Tsai-Hill criteria to the stress field generated by their exact solution to indicate damage patterns in composite materials

over various load conditions. His integral transform technique specified indenter contact length and calculated the corresponding indenter load so direct comparisons to a particular load case for the finite element results considered here may not be possible. However, the stress and Tsai-Hill failure criteria contours developed from his solution should exhibit the same characteristic pattern as any developed from the finite element analysis included in this thesis. Copp's particular case of indenter contact length to specimen depth ratio ( $c/h$ ) of 0.25, and semi-span to depth ratio ( $L/h$ ) of 2.0 should closely compare with the three point bend specimen of length to depth ratio equal to four considered in this study.

## II Theoretical Development

### a. Failure Criteria

In order to predict damage initiation, "damage" must be defined in a mathematical sense. Exceeding the mathematical limits implies the structure would experience physical damage under the same conditions. Applying the failure criteria provides a convenient way to compute net strength in both uniaxial and combined stress states. There are many failure theories applicable to composite materials. Frequently, they are extensions of criteria applied to isotropic materials such as maximum stress, maximum strain, or quadratic theories like von Mises failure criterion (26:280). Even though many of these criteria are more empirically than analytically developed, they are still consistent with basic mechanics and generally work well as design guidelines (24:11.1). Because of increased complexity of failure modes in composites as compared to isotropic materials, we must be careful not to oversimplify the observed physical phenomena just to fit an isotropic material failure pattern. And although we may not be able to describe many of the concurrent and interactive failure modes on a microscopic level, certain criteria such as the ones listed above do provide some insight to the global, "engineering" behavior of the material.

Based on our limited understanding of the microscopic failure behavior of Carbon-Carbon composites, predicting failures using a fracture mechanics or "critical flaw size" model would be premature. Also, since maximum stress and strain criteria treat stress or strain in only one direction and are uncoupled criteria, they are least likely to accurately predict behavior of coupled composite materials. Thus, the criteria used in this research is based upon the combined longitudinal, transverse, and shear strengths of ACC-4 in the form of Tsai-Wu tensorial and Tsai-Hill quadratic criteria.

Tsai and Wu (27:58-80) compared different failure criteria for anisotropic materials. They realized that most criteria agree when referring to principal strengths, i.e., uniaxial and pure shear test data measurement along material symmetry axes. However, they also noted that disagreements among the criteria frequently occurred in the combined stress state, i.e., in predicting failure points not on the principal strength axes. For this reason, a general strength criterion, invariant under coordinate transformation, was proposed by Tsai and Wu to account for stress interactions and to predict off-axis failures. This technique uses two strength tensors in the scalar function

$$f(\sigma_k) = F_i \sigma_i + F_{ij} \sigma_{ij} = 1 \quad (1)$$

to represent a failure surface. In three dimensions, this function contains 27 terms in expanded form with  $i, j, k = 1, 2, \dots, 6$ . The coefficients of the resulting stress polynomials are functions of the material strength characteristics, usually determined from uniaxial experiments (27:64-65). For the orthotropic laminate beam under plane stress conditions, this criteria reduces to

$$F_1\sigma_1 + F_2\sigma_2 + F_6\sigma_6 + F_{11}\sigma_1^2 + F_{22}\sigma_2^2 + F_{66}\sigma_6^2 + 2F_{12}\sigma_1\sigma_2 = 1 \quad (2)$$

where  $F_i$  and  $F_{ij}$  are strength tensors of second and fourth rank respectively, and can be described in terms of engineering strengths as follows:

$$F_1 = \frac{1}{X_T} + \frac{1}{X_C}, \quad F_{11} = -\frac{1}{X_T X_C} \quad (3)$$

$$F_2 = \frac{1}{Z_T} + \frac{1}{Z_C}, \quad F_{22} = -\frac{1}{Z_T Z_C} \quad (4)$$

$$F_6 = 0, \quad F_{66} = \frac{1}{S^2} \quad (5)$$

with

$X_T$  = uniaxial tensile strength

$X_C$  = uniaxial compressive strength

$Z_T$  = interlaminar tensile strength

$Z_C$  = interlaminar compressive strength

for the subject three point bend specimens. The  $F_{12}$  or biaxial strength term was originally described by Wu as a function of the four uniaxial strengths and  $\sigma_b$ , the biaxial tensile strength. Wu (32:474-482) showed that the  $F_{12}$  term is small and gave some guidelines for experimentally determining  $F_{12}$ . He went on to show that experimental methods of measuring this biaxial stress interaction were themselves a function of the applied biaxial stress ratio and thus the error in measuring  $F_{12}$  depended on  $F_{12}$ . To find the true value of  $F_{12}$  experimentally, Wu claimed an iterative experimental process was required and was based on initial assumed values of  $F_{12}$  and the biaxial stress ratio. Rather than pursue this complicated procedure to find  $F_{12}$ , an approximate value of  $F_{12}$  was calculated through a relationship prescribed by Tsai and Hahn (26:284). Tsai and Hahn determined this expression for  $F_{12}$ , derived

from a generalized von Mises criterion:

$$F_{12} = -\frac{1}{2} \sqrt{F_{11}F_{22}} \quad (6)$$

which reduces to

$$F_{12} = \frac{1}{2 \sqrt{X_T X_C Z_T Z_C}} \quad (7)$$

for the orthotropic, plane-stress case considered here. Therefore, the Tsai-Wu criteria referred to in this study is actually the original Tsai-Wu criteria modified by substituting Tsai and Hahn's  $F_{12}$  expression for the biaxial strength term.

The advantages to the Tsai-Wu criteria are that it is invariant, easy to transform, and shows a variety of stress interactions in a complex combined stress field. However, this criteria requires all unidirectional material stress or strain limits be known and estimates the coupling coefficients from these values. Accuracy depends on uncertainties in the input material stress limits. On the

other hand, the Tsai-Hill criteria combines most of the favorable properties of the Tsai-Wu criteria but with less dependence on the individual material stress limits.

The Hill criteria began as a generalized failure criteria for anisotropic material proposed by Hill (5:318-320) in 1950. Hill reasoned that since the von Mises distortion energy criterion approximately described the yielding of isotropic materials, the anisotropic criteria should reduce to von Mises for the isotropic case. Assuming the criteria was quadratic (to provide a closed, finite, failure space), he proposed the following relationship to define yield points

$$F(\sigma_y - \sigma_z)^2 + G(\sigma_z - \sigma_x)^2 + H(\sigma_x - \sigma_y)^2 + 2L\tau_{yz}^2 + 2M\tau_{zx}^2 + 2N\tau_{xy}^2 = 1 \quad (8)$$

where F, G, H, L, M, and N are parameters characteristic of the anisotropic material. Later, Tsai (25:3-11) expressed these parameters in terms of the usual failure strengths X, Y, and S for a laminate as mentioned above. For an applied shear only, he found

$$2 N = \frac{1}{S_{12}^2}$$

$$2 M = \frac{1}{S_{13}^2} \quad (9)$$

$$2 L = \frac{1}{S_{23}^2}$$

where the S terms are the appropriate shear strengths. For an applied pure axial load he found

$$G + H = \frac{1}{X^2}$$

$$F + H = \frac{1}{Y^2} \quad (10)$$

$$F + G = \frac{1}{Z^2}$$

where X, Y, and Z are the tensile or compressive strengths along the respective material axes. Solving the above equations for F, G, and H,

$$2 H = + \frac{1}{X^2} + \frac{1}{Y^2} - \frac{1}{Z^2}$$

$$2 G = + \frac{1}{X^2} - \frac{1}{Y^2} + \frac{1}{Z^2} \quad (11)$$

$$2 F = - \frac{1}{X^2} + \frac{1}{Y^2} + \frac{1}{Z^2}$$

For the case of plane stress in the 1-3 plane and for

$$X = X_T = X_C \quad \text{and,} \quad Z = Z_T = Z_C \quad (12)$$

The Tsai-Hill failure criteria can be expressed

$$\frac{\sigma_1^2}{X^2} - \frac{\sigma_1\sigma_3}{X^2} + \frac{\sigma_3^2}{Z^2} + \frac{\sigma_{13}^2}{S^2} = 1 \quad (13)$$

where  $\sigma_1$ ,  $\sigma_3$  and  $\sigma_{13}$  are the principal stresses. Jones (7:79) indicates this theory agrees with the experimental failure data for E-glass/epoxy composites, particularly under tensile loads. Calculations of the Tsai-Hill criteria in this thesis are based on X and Z equal to the compressive strengths rather than the tensile strengths. Since compressive stress fields predominate in the three point bend test, it was felt that this would produce more realistic failure contours. Knowing the stress components at a given point, one can evaluate Equation (13) to check for possible failure. Thus, the task now becomes one of finding the stresses at various points within the specimen. Since measurement of internal stress is impossible we must model the structure in some fashion and check its performance in predicting an experimentally measurable quantity like external displacements for a given test. If the displacement predictions are reasonable, then one

assumes the stress field generated by the model is reasonable, provided the fundamental principles aren't violated in the computations.

b. Finite Elements and Damage Initiation

Finite Element Analysis (FEA) has become a common engineering tool for modeling structures under specific loads, especially when considering macro mechanical or overall material behavior. It's a numerical procedure for approximating a solution to a continuum mechanics problem with sufficient accuracy for engineering purposes. Finite Element Analysis uses a lumped element approach where a structure is discretized into a finite number of idealized substructures, each with its own material properties, and interconnected at a finite number of grid points. Applied loadings are also discretized into "equivalent nodal loads" at these grid points. Then, for analyses based on the displacement formulation, the overall stiffness matrix  $[K]$ , and the applied load vector  $\{r\}$  are computed and used to solve:

$$[K]\{d\} = \{r\} \quad (14)$$

for the unknown grid point displacements  $\{d\}$ . This solution requires inversion of the global stiffness matrix  $[K]$ , and

thus  $[K]$  must be constrained to a non-singular matrix by removing degrees of freedom appropriate for the physical supports and providing resistance to motion in the supported directions. Discretizing the model will tend to induce error in the computed nodal displacements when compared to an exact continuum solution, however, for an increasing number of elements in the structural model, the net error should converge to zero (3:94). The inherent flexibility in FEA of assigning specific material properties to specific elements make FEA a particularly useful tool for analysis of composite materials.

Many individual and commercial computer codes for FEA already exist. They range from codes such as NISA™ which can analyze global behavior of small, simple models on a personal computer, to powerful and sophisticated codes for mainframe computers such as STAGS™, SNAP™, ADINA™, and SAPIV™ which incorporate non-linear material response and element failure schemes for both macro and micro mechanical response. However, the most common Finite Element Analysis code used by government and industry is the NASTRAN™ code developed by NASA (11). NASTRAN™ is written for "standard" linear static and dynamic analyses and includes provisions for "tailoring" by the user through "DMAP" alter sequences or combinations of rigid formats. The COSMIC, 1987 version of the NASTRAN™ code is installed, maintained, and readily

available on several mainframe computers here at Wright-Patterson AFB and was used for the Finite Element analysis conducted in this thesis. Since the focus of this study is on predicting damage initiation in three point bend specimens, and not post-failure response, a linear material response model was deemed adequate for the purpose at hand in favor of speculating at a complex non-linear material model. In addition, the finite element models used were only two dimensional as width or edge effects were deemed insignificant for the purely orthotropic material tested.

Efforts to model the three point bend specimen began with a coarse 5 x 20 element mesh of the entire  $L/d = 4$  specimen. All elements in the mesh were rectangular isoparametric membrane elements with a 1.25 length/width aspect ratio. Indenter and support pin loads were approximated as point loads on the appropriate grid points with one support node constrained as rigid, and the other free to displace only in the longitudinal (x) direction. The grid point coordinates were computed through a FORTRAN program and were numbered along each row from the lower left corner to the upper right corner of the model. The program also defined the four grid points of each sub-element rectangle as a specific isoparametric membrane element, and wrote the actual NASTRAN™ "GRID" and "CQDMEM1" (12) node and element input deck lines for the input file. Since the node

and elements numbers were generated sequentially by a computer program, they weren't the optimum arrangement for minimum band-width. However, NASTRAN™ internally optimized and automatically renumbered the mesh elements using the "BANDIT" algorithm before solving the matrix equation for the nodal displacements and element stresses.

Having constructed a working Finite Element model of the short test specimen, it was necessary to validate its performance with common Aluminum material properties before applying Carbon-Carbon material properties. The element stresses output by the model were input to a FORTRAN program which computed the centroidal coordinates of each element and assigned the element stresses to a point at that centroid. These values were then input to SURFER™ (22), a personal computer, 3-D plotting program in order to generate contour plots of the stress distributions within one half of the finite element model. Two of these contour plots are shown in Figures 6 and 7. One can see the same characteristic shape of the normal and shear stress distributions as predicted by Copp's (4:124,127) exact elasticity solutions, shown in Figures 8 and 9, which indicates generally acceptable model performance.

Having demonstrated this, a refined mesh model was built in order to reduce the stress differences between each element and to enhance the agreement between the finite

element and exact solutions. The refined model consisted of a 10 x 50 element mesh of the same  $L/d = 4$  specimen. As before, all elements were rectangular isoparametric membrane elements, but with an aspect ratio reduced to one. Again, contour plots of the predicted shear and normal stress distributions were generated for the Aluminum beam test case and are shown in Figures 10 and 11. Comparing these with the same plots for the coarse mesh model shows how the refined mesh produces smoother contours for the same load condition, particularly in the vicinity of the applied loads. Comparing Figures 10 and 11 with Figures 8 and 9 also indicates the refined mesh is in much closer agreement with the elasticity solution stress fields than the coarse mesh. A diagram of this refined mesh model is shown in Figure 12 for reference.

The model for the long ( $L/d = 15$ ) specimens was essentially three of the short beam models connected at the ends. The only difference is that both support nodes were moved to the extreme ends of the model and elements modeling the support pin overhang section of the specimen were eliminated to reduce model size for convenience in plotting the resultant stress contours.

Substituting ACC-4 material properties for the Aluminum properties, yielded working models of the ACC-4 test specimens and these models were used to generate the results

discussed in Chapter IV. The NASTRAN™ input deck is listed in condensed form in Appendix A. All of the Executive and Case Control cards for the sample case are listed. However, the Bulk data GRID and CQDMEM1 card listing alone contains over 1000 line entries so the appendix listing shows only a few sample cards for this segment of the data deck. Enough information is given such that the input deck could easily be reconstructed from the listing in Appendix A.

To predict failure, the output of the Finite Element Models were input to a FORTRAN program written by the author which calculated the magnitude of the failure criterion for each element. The important parts of this FORTRAN "post-processor" are the segments which read in the Finite Element Analysis output stresses and compute the magnitudes of the two failure criteria. Since most of the post-processor program involves simple manipulations of data, only these two important segments of the code are listed in Appendix B.

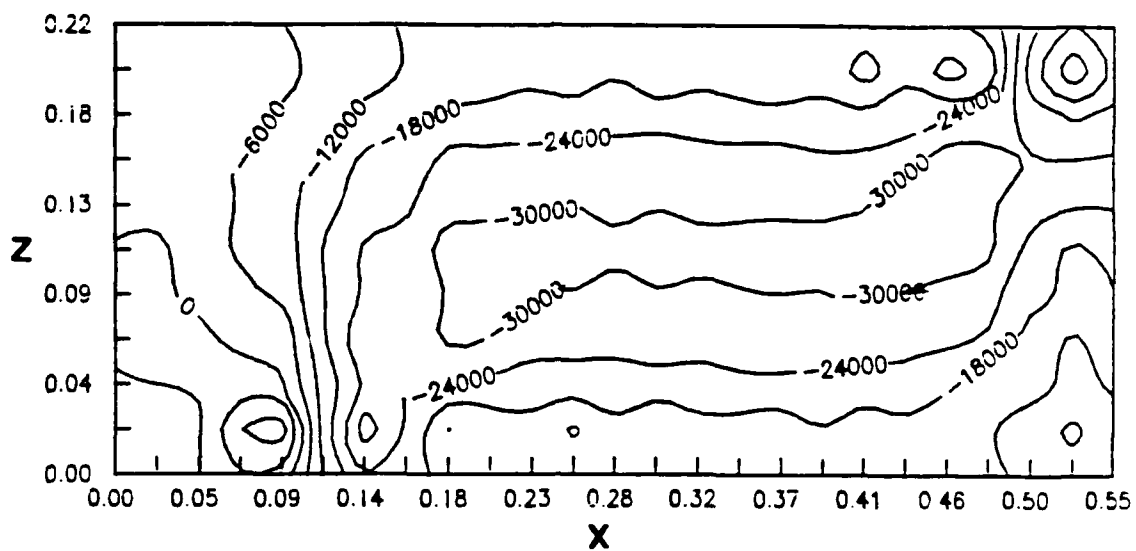


Figure 6. Shear Stress  $\sigma_{xz}$  (psi),  $N=100$ ,  $P=100$  lbs,  $L/d=4$

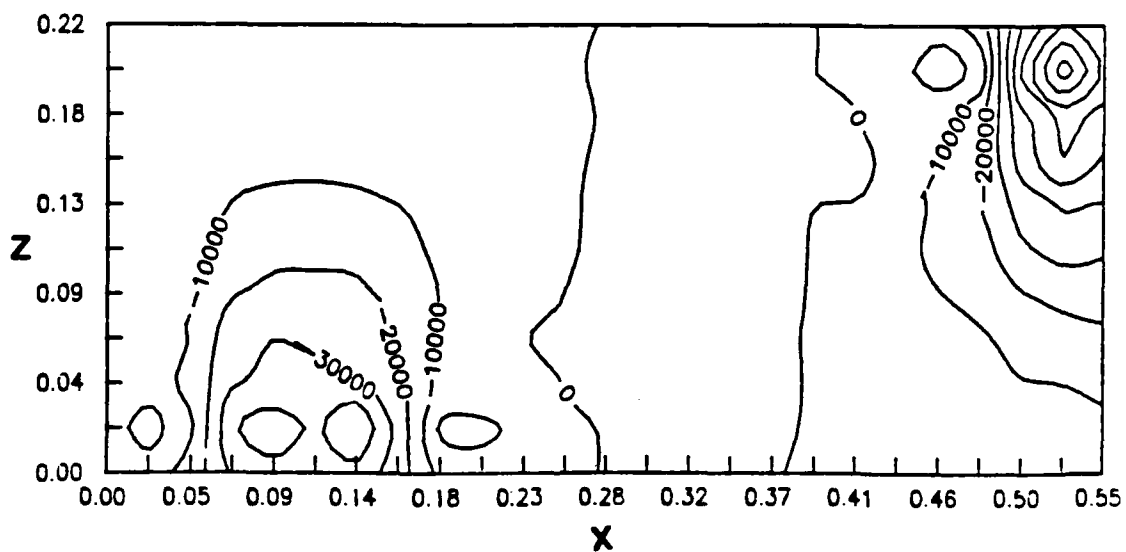


Figure 7. Normal Stress  $\sigma_z$  (psi),  $N=100$ ,  $P=100$  lbs,  $L/d=4$

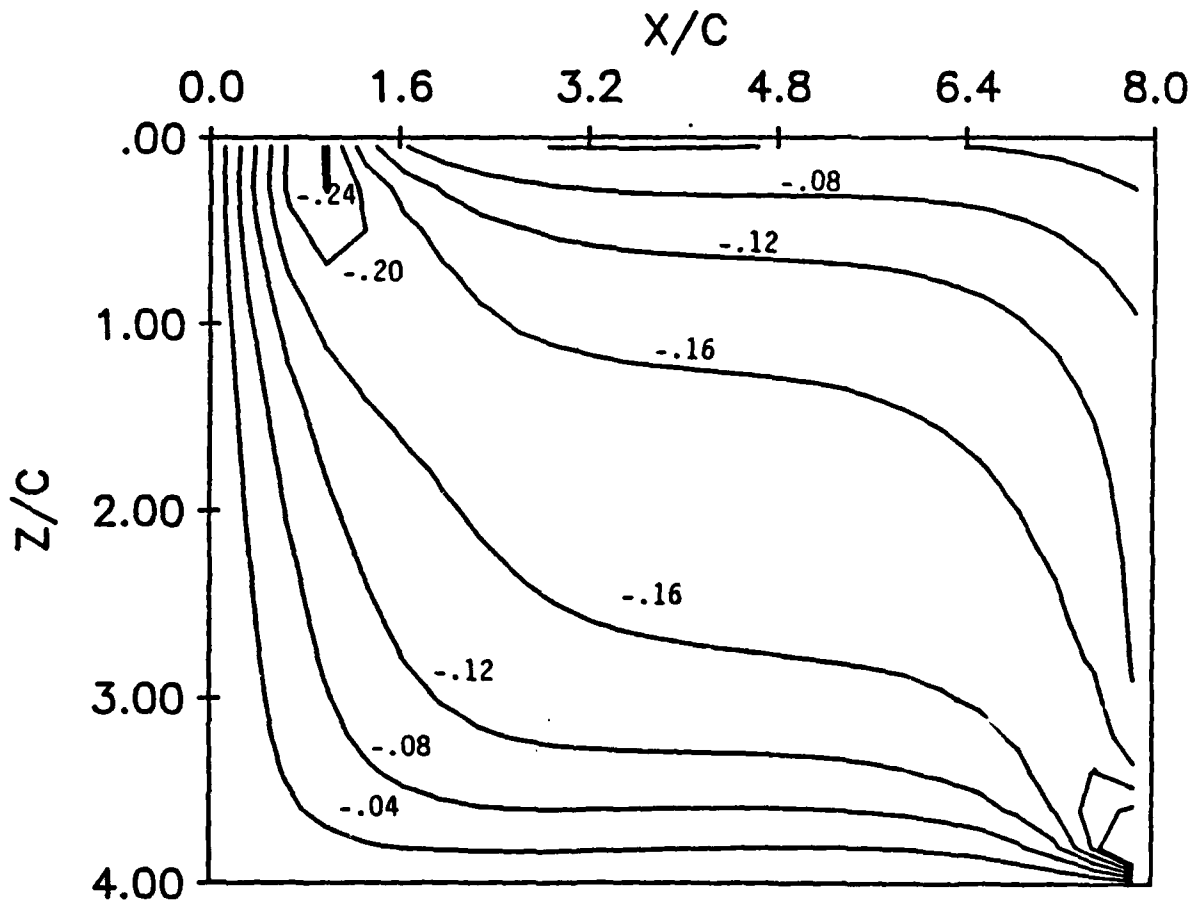


Figure 8. Copp's Exact Shear Stress Distribution (4),  
 $c/h = 0.25$ ,  $L/h = 2.0$

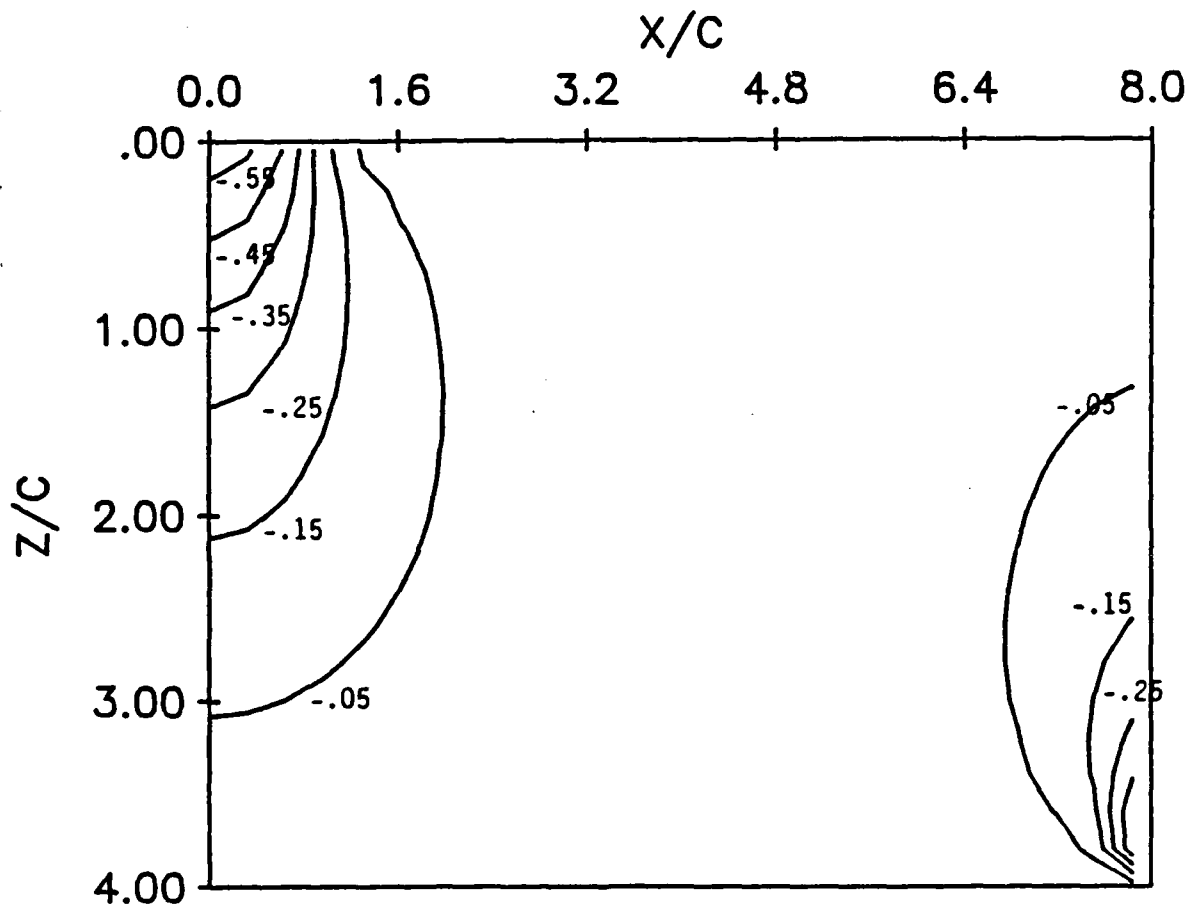


Figure 9. Copp's Exact Normal Stress Distribution (4),  
 $c/h = 0.25$ ,  $L/h = 2.0$

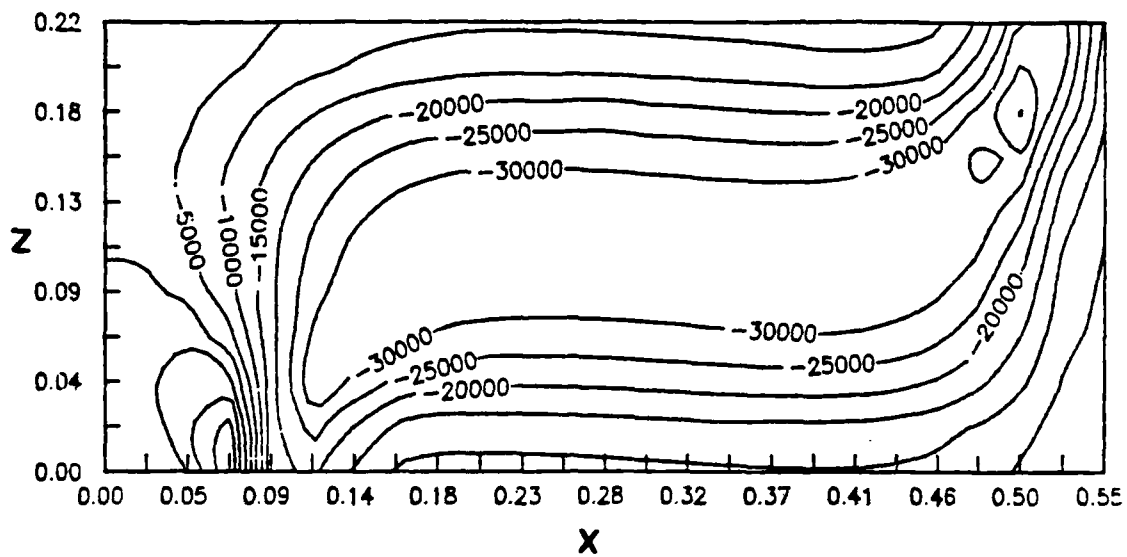


Figure 10. Shear Stress  $\sigma_{xz}$  (psi),  $N=500$ ,  $P=100$  lbs,  $L/d=4$

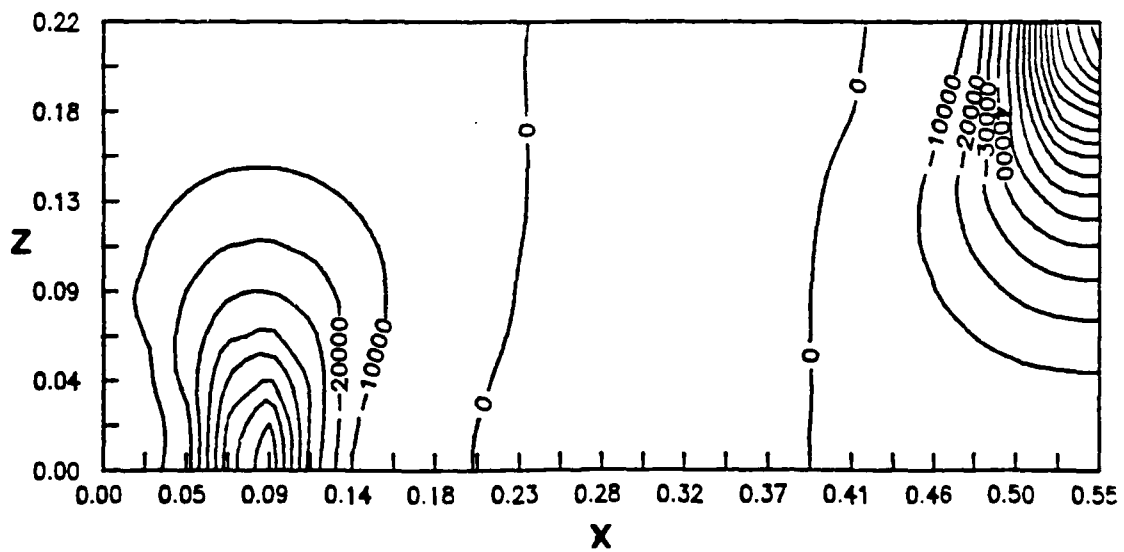


Figure 11. Normal Stress  $\sigma_z$  (psi),  $N=500$ ,  $P=100$  lbs,  $L/d=4$

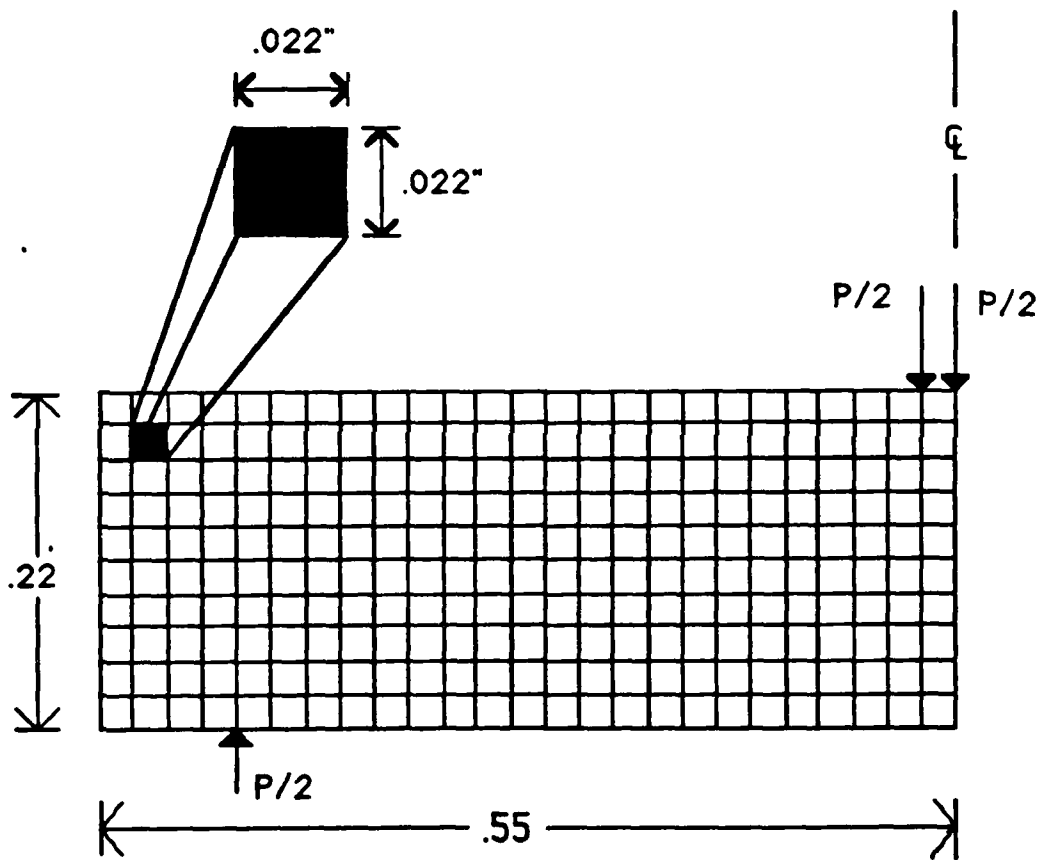


Figure 12. Left Half of the Finite Element Model,  $L/d = 4$

### III. EXPERIMENTATION

#### a. Objective

To determine the damage progression and mode of failure of these ACC-4 beams, specimens of varying length-to-depth (L/d) ratios were tested in a three-point bend fixture under the guidelines of ASTM-2344 (2). Since the shear modulus is about 1/40 of the tensile modulus, and since the test specimens were relatively short, shear failures were expected in the x-y plane rather than tensile failures due to the bending. For these experiments, "failure load" is defined as the maximum load obtained on the load-displacement curve generated by the experiment. This represents an ultimate load since the specimen exhibited large deformations and ply separations beyond this load. Following the tests, the specimens were examined through a microscope and high-magnification photographs (micrographs) were taken to record the internal damage in the specimen. The following sections provide the specifics of specimen preparation, test apparatus, and the actual test procedure.

#### b. Specimen Preparation

The ACC-4 material tested was supplied by Mr T. Fecke of the Air Force Aeropropulsion Laboratory in three (3) strips, each 8.4" long, 1.0" wide, and 0.22" thick. These strips were intended for use as test specimens in a contractual

research effort and had passed a series of pre-test inspections, but were not needed. The strips were also X-rayed by the Materials Laboratory prior to sectioning and no internal delaminations or defects were detected. Afterward, the strips were cut into the various test specimens as indicated in Figure 13. Specimens were designated "x/y-z" where

x = 2 for the 0.22" thickness (d)

y = L/d ratio for the specimen

z = specimen number of the given x/y type

In all, 16 total specimens were cut, six at L/d = 4, six at L/d = 5, and four at L/d = 15. The specimens were cut with a rectangular cross-section (width-to-depth ratio, w/d = 2) rather than the ASTM-recommended square cross-section for comparison to known four-point bend tests of similar rectangular specimens. Note that the specimens were cut to the required length for the desired L/d test ratio, plus only 0.25" for support pin overhang. This minimal amount of material overhang allowed the maximum use of the available material and should not affect test results. Next, the specimens' sides were polished with a series of coarse (120) to ultra fine grit (1 micron) sand paper to enhance the surface for viewing crack development, and to provide a smooth surface for acceptable micrographs. The top center

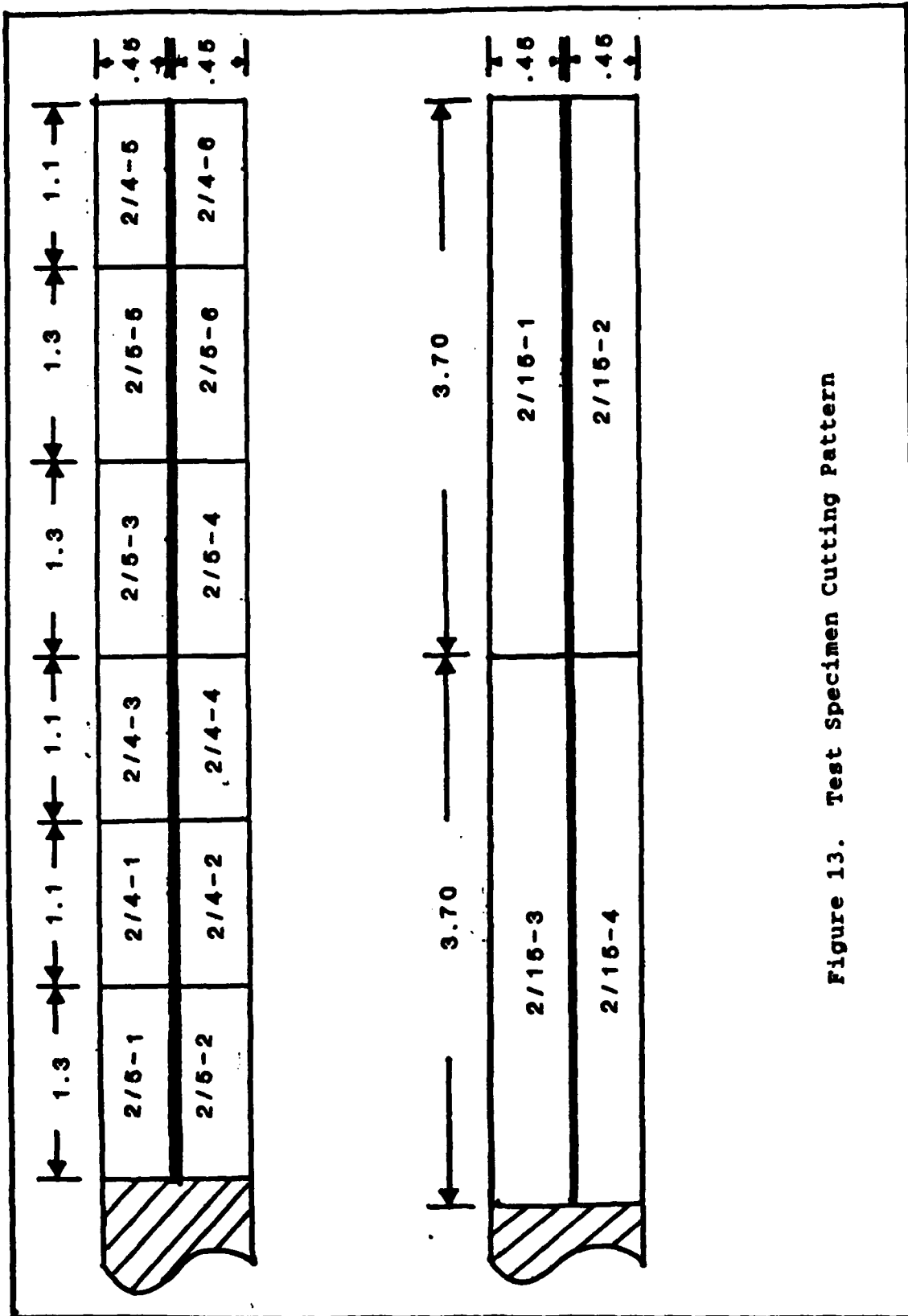


Figure 13. Test Specimen Cutting Pattern

of each specimen was then measured and marked with a felt tip pen as a guide for indenter placement during the test. Using this mark as the approximate location of the indenter contact line, micrographs were made of the top section of the polished face in the vicinity of this line as pre-test record of the material condition. Each specimen was then placed in separate bags to prevent incidental contact and scratching of the polished surfaces. Measurements of the final polished specimen dimensions were taken only after the tests for the same reason.

#### c. Test Equipment

The specimens were loaded in three-point bend through the motion of the cross-head of the Instron tester. Table 3 lists all equipment used in the testing and schematic diagrams of the test set-up are shown in Figures 14 and 15. An Interface SM-1000 Load Cell and Endevco amplifier supplied the load voltage signal to the Digital Voltmeter (DVM) and the X-Y plotter. Prior to testing, the load cell was calibrated by Precision Measurement Laboratory technicians to a traceable standard load cell. By placing both load cells in series and applying uniform load increments, output from the standard load cell was used to calibrate the SM-1000 Load Cell. The results of this calibration demonstrated that our load cell calibration curve was linear and constant throughout the load cell

range. All test loadings were converted from volts to pounds of load using this line which is shown in Appendix C.

Table 3: Equipment List

Load Measurement	
<ul style="list-style-type: none"> <li>a. Instron TTD tension/compression tester</li> <li>b. Interface SM-1000 Load Cell</li> <li>c. Endeveco 4225 Power Supply &amp; 4423 Signal Cond.</li> </ul>	
Range: 0 - 1000 lbs	Accuracy: $\pm 0.3$ lbs
Displacement Measurement	
<ul style="list-style-type: none"> <li>a. Robinson-Halpern 225A-300 LVDT</li> <li>b. Power-Ten 3130A-2000 Power Supply</li> <li>c. Local Adjustable Amplifier/Rectifier</li> <li>d. Hewlett-Packard 3312A Function Generator</li> </ul>	
Range: $\pm 0.30$ in	Accuracy: $\pm 0.0002$ in
Output	
<ul style="list-style-type: none"> <li>a. Hewlett-Packard 3466A Digital Multimeter</li> <li>b. Hewlett-Packard 7045B X-Y Plotter</li> </ul>	

To measure specimen deflection, we used a Robinson-Halpern Linear Variable Differential Transducer

(LVDT) and a locally manufactured adjustable Amplifier/Rectifier to produce a linear signal which could also be set to zero at the start of the test. The LVDT was mounted inside the support stand and aligned so that the transducer for weight rested on a spring at the bottom of the stand, while the top protruded through the support plate and touched the center of the lower surface of the specimen. As the specimen deformed under the load, the transducer rod was forced down which induced a voltage in the LVDT. This voltage was amplified and rectified then input to the X-Y plotter. Prior to testing, the LVDT was calibrated with a dial micrometer. The head of the micrometer was brought to rest against the tip of the transducer rod and adjusted until the tip of the rod was at the approximate level of the bottom of the test specimen. Then the LVDT output voltage was set to zero and incremental micrometer displacements were made. The LVDT output for each displacement was plotted and showed that the LVDT output was linear over the 0.0 to 0.030 inch expected range of test specimen displacements. This calibration curve is also included in Appendix C. Repeated calibrations showed the slope of the calibration curve remained constant, thus it was not necessary to recalibrate the LVDT for each test.

During the tests, load was continuously monitored in the form of the load cell output voltage on the digital voltmeter. Maximum load was determined by recording the

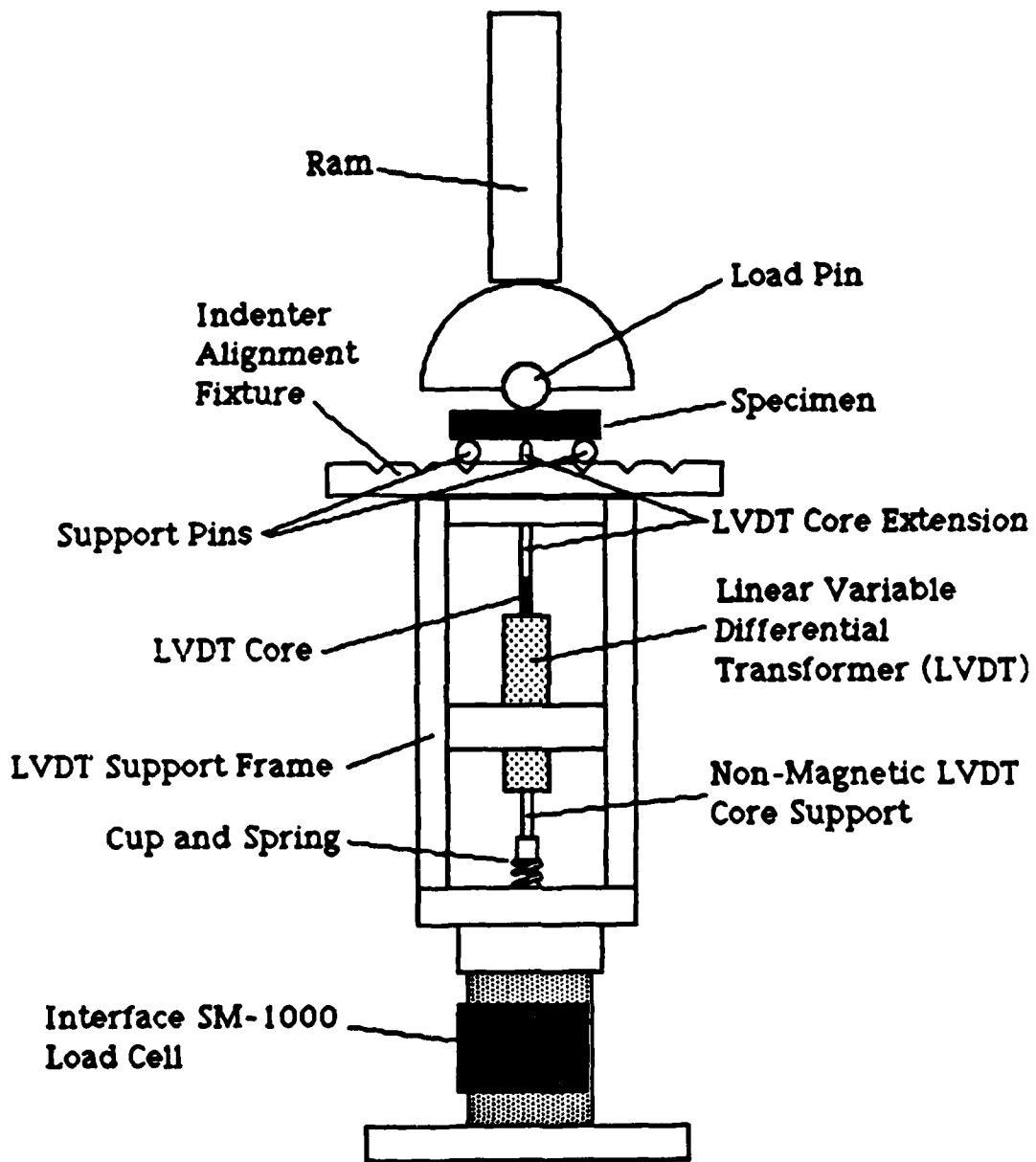


Figure 14. Experimental Fixture Diagram

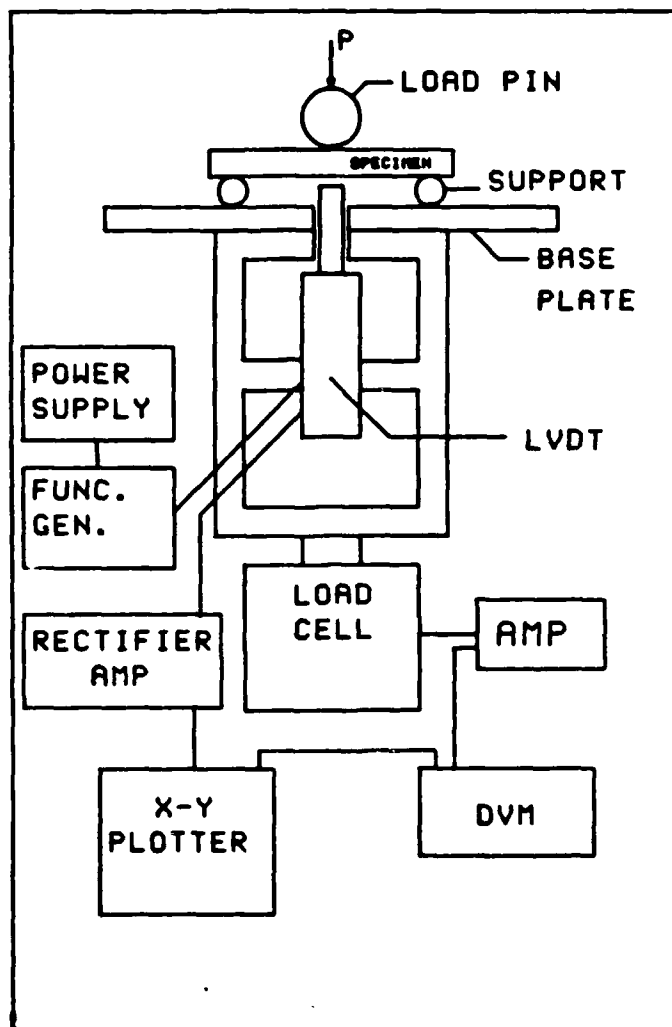


Figure 15. Equipment Schematic

maximum voltage displayed on the DVM during the test. This value was compared to the magnitude of the X-Y plotter trace to insure accuracy of the trace.

The plotter provided a permanent record of test results in the form of load-deflection curve generated by the plotter. The load cell voltage was plotted along the y-axis while the deflection voltage was plotted along the x-axis. The plotter axis scales were set prior to the test to allow maximum use of the plotter paper. Reduced copies of all such experimental traces are included in Appendix C. As mentioned previously, load cell and LVDT calibration curves are also included in Appendix C so that the raw data contained in the experimental Load vs Displacement curves may be correctly interpreted.

#### d. Test Sequence

As mentioned previously, a modified version of the ASTM-2344 Short Beam Shear test was used to damage and eventually fail the specimens. Here's a brief description of the test procedures used to generate the load versus mid-span deflection curves shown in Appendix C.

After a 1-2 hour equipment warm-up, and prior to any testing, the load ram was brought to bear on the empty support plate. Then, the fixture was loaded to approximately 500 lbs and unloaded, three times, to "exercise" the load cell and LVDT. This ensured all

equipment functioned properly before inserting test specimens into the load path.

Next, the support pins were set in the appropriate grooves for the test specimen L/d ratio and the specimen was set on the LVDT rod and support pins and weighed down with the load pin centering fixture. The load cell output voltage was adjusted to zero at this point since this represented the "zero load" condition. Afterward, approximately 0.003 to 0.008 Volts (2 to 5 lbs) of light preload was applied with the load ram to loosely hold the specimen in place. Careful minor adjustments were made to center the specimen over the support pins and LVDT, and to align the load pin. Having set the specimen in the proper position, LVDT output voltage was set within +0.001 and -0.001 Volts ( $\pm 0.0001$  inches), the best "zero" achievable with the sensitive LVDT balance. Next, the X-Y plotter pen was adjusted to the test plot origin and the axis scales set appropriately for the test. Then, selecting the "0.002 in/min" (the minimum in low range) crosshead speed on the Instron tester, testing commenced by starting crosshead motion down.

For the  $P_{max}$  tests, specimens were loaded until the Digital Voltmeter (DVM) readout reached a maximum value and started to decline. At this point, crosshead motion was reversed and the specimen was slowly and completely unloaded. For load levels less than  $P_{max}$ , a turn-around

load and corresponding voltage were calculated prior to the test and the crosshead motion was manually reversed as soon as load cell output reached this value. Loading at 0.002 in/min was slow enough that overshooting the target load wasn't a problem. Load and displacement output was continuously plotted until the specimen returned to zero load. A test loading with a steel sample beam similar to the dimensions of the C/C test specimens was run to test the operation of the equipment. The load-displacement curve generated in this test is shown in Figure 16 and indicates that the LVDT and load cell traces will return approximately to zero when the specimen isn't permanently deformed.

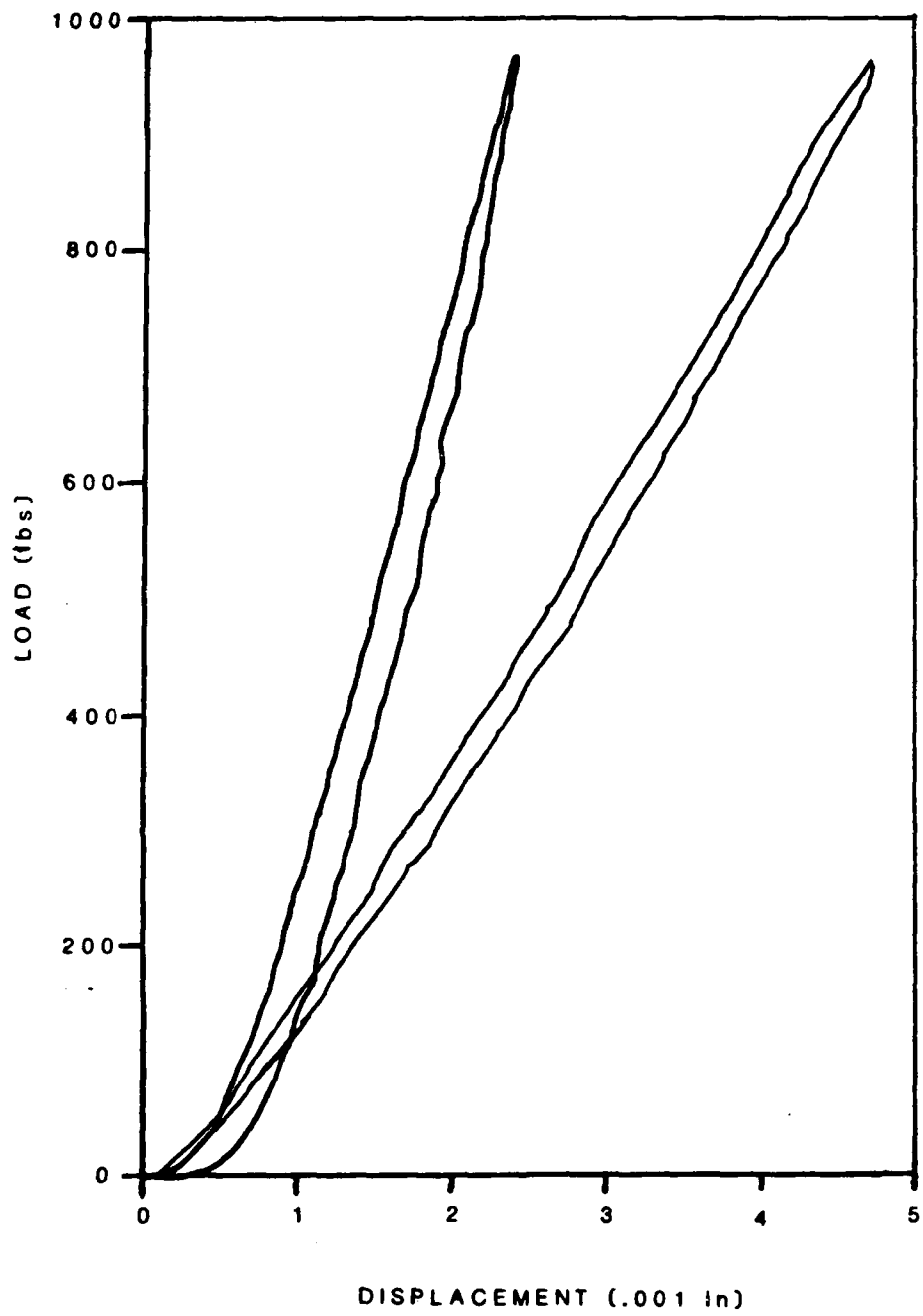


Figure 16. Steel Beam Load-Displacement Curve, Test Case

#### IV. Results and Discussion

##### a. Maximum Load Test Results

The first series of experiments involved over half of the available test material and determined the range of maximum sustainable loads. A total of 12 specimens, four at each L/d ratio, were loaded to failure using the procedure described in Chapter III. Afterward, the damaged specimens were microscopically examined to detect similarities and differences between damage in the three different L/d ratio specimen types. Figure 17 shows the results of these tests and compares them to four-point bend data obtained recently by Szaruga (23) with similar ACC-4 material. Note that the difference in  $P_{max}$  is greatest for the L/d = 4 specimens and decreases as the L/d ratio increases as shown in Table 4.

Table 4.  $P_{max}$  Test Results Summary

L/d	Average P (lbs)	$\Delta P_{max}$ (lbs)	$\Delta P_{max}$ (%)
4	300	36	12
5	275	15	6
15	165	6	4

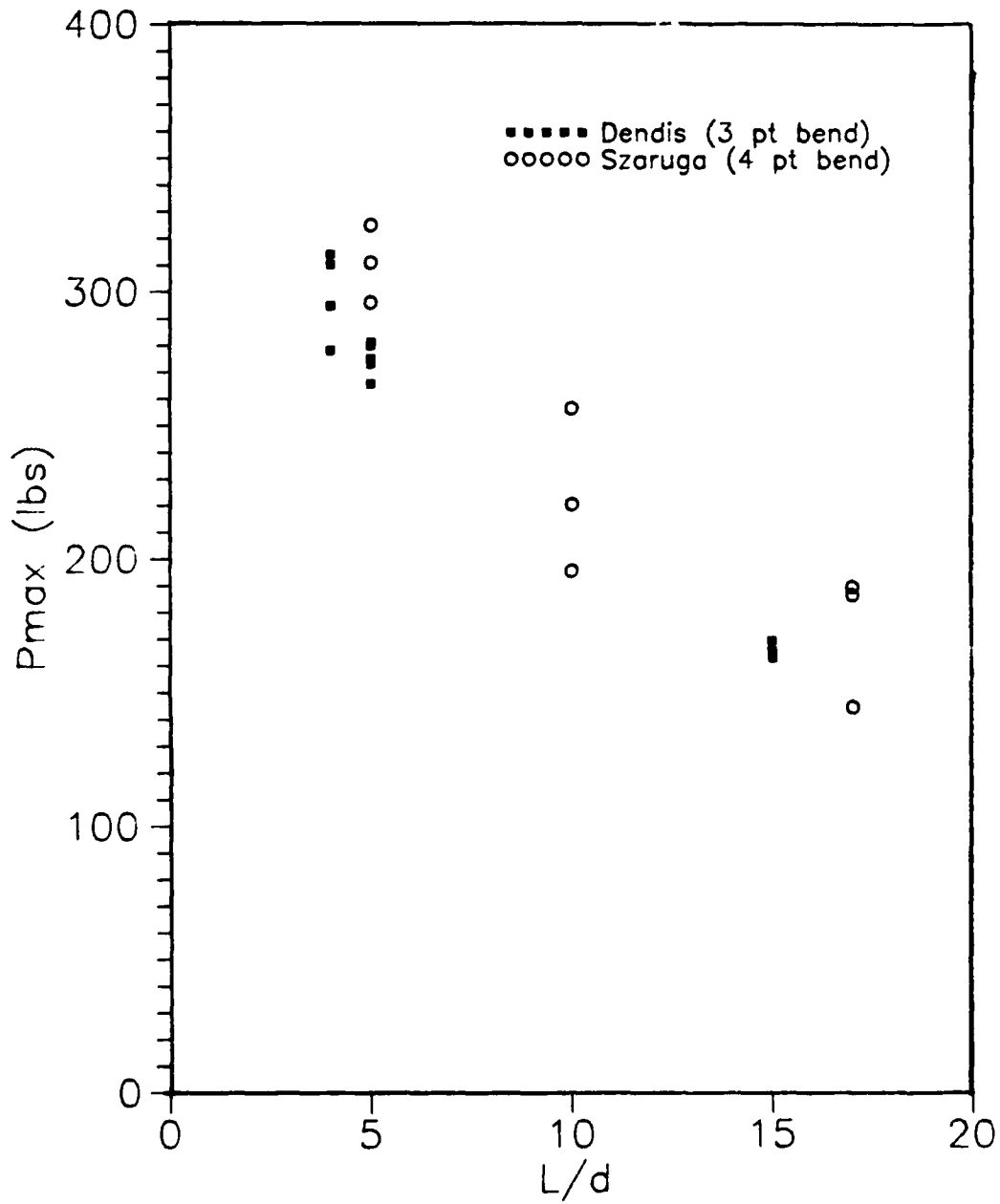


Figure 17. Test Results, Maximum Load Vs L/d Ratio

Fortunately, two cases at  $L/d = 4$  and two cases at  $L/d = 15$  achieved the same maximum load demonstrating repeatability of the experiment. In these instances, the maximum displacements recorded by the LVDT differed by less than 1%, and were easily within the accuracy of the LVDT system. This indicates that the experiment was accurate as well as repeatable.

Examining photomicrographs of the damaged specimens reveals that all specimens have a fractured outer ply at either the indenter or support pin contact area as shown in Figures 18, and 19. Pre- and post-test micrographs such as are shown in Figure 20 prove the cracking occurred during the test and was not caused by cutting and polishing the specimens. Examination of the back surfaces of the  $L/d = 15$  specimens revealed that the outer ply fracture doesn't always travel outward to both edges of the beam. For the specimen shown in Figure 21, the top ply fracture wasn't visible on the front face, but on the back face instead. It is interesting to note that in Figure 21(a) of the front face, the indenter appears to have pressed on a fill yarn rather than the warp yarn as on the the back face shown in Figure 21(b). Since the warp yarns contribute the most to the bending stiffness because they are perpendicular to the load line, it is reasonable to expect ply fractures at the back face rather than the front face for this particular specimen. This asymmetrical contact resistance appears to



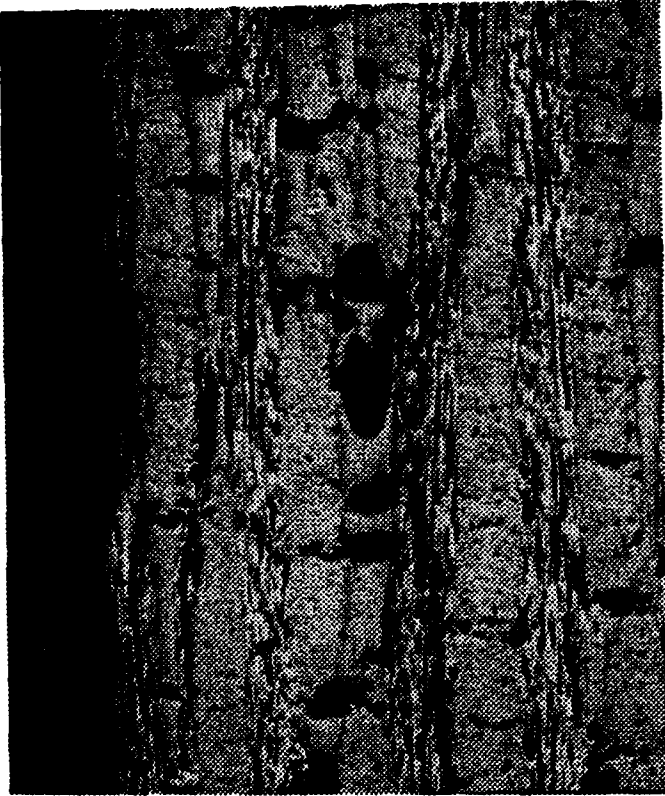
Figure 18. Top Ply Fracture,  $L/d = 15$ ,  $R = 100\%$ , (100x)



Figure 19. Top Ply Fracture Under Indenter,  $L/d = 5$ , #4,  
R = 100%, (100x)



(a) Pre-Failure



(b) Post-Failure

Figure 20. Top Ply Fracture, Indenter Contact Zone,  $L/d=15$ , # 3,  $R=100\%$ , (50X)

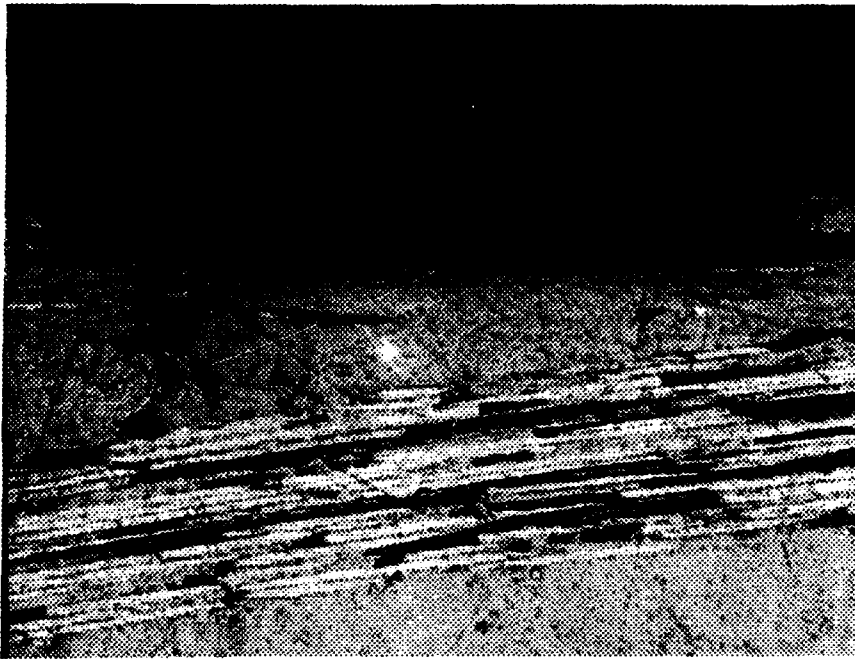


Figure 21(a). Indenter Contact Zone, Front Face,  $L/d = 15$ ,  
#2, R = 100%, (200x)

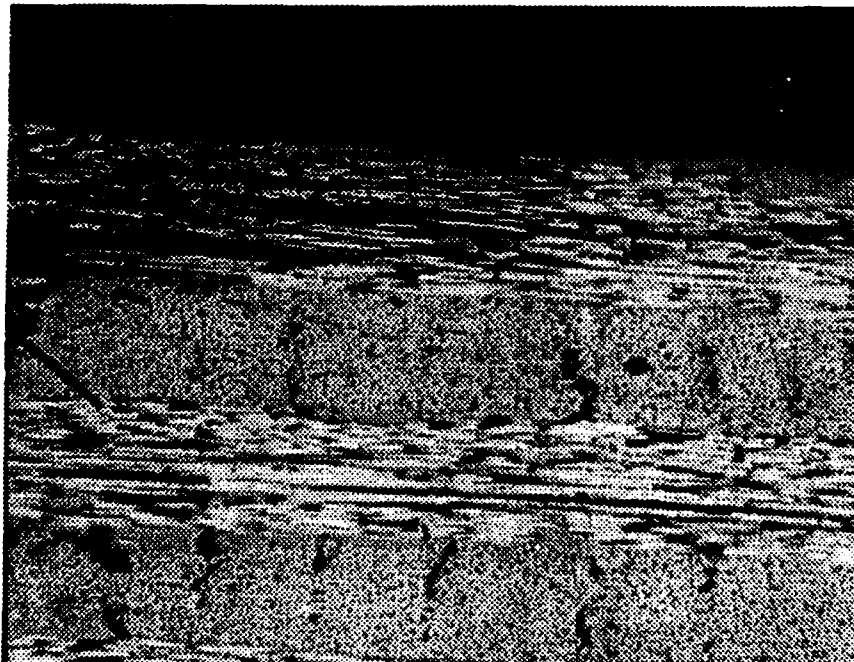


Figure 21(b). Indenter Contact Zone, Back Face,  $L/d = 15$ ,  
#2, R = 100%, (100x)

contribute to asymmetrical crack propagation throughout the specimen as well. Figure 22 indicates the cracks also fail to equally propagate to the outer faces at the neutral axis. Again, in Figure 22(a) one sees the polished front face at mid height and about 0.2" right of the load contact line and notices no cracking. Whereas in Figure 22(b), one can see the distinct cracks photographed on the back face of the specimen just opposite the location of Figure 22(a).

Unlike the outer ply damage, the internal ply damage varied in size and location among the different specimens. In the short ( $L/d = 4, 5$ ) specimens, multiple cracks were present in most every internal layer of fill fibers. Figure 23 shows several cracks in the fill layers just below the top surface. These cracks run generally at a 45 degree angle although their direction of travel is highly influenced by the presence of internal voids and proximity to the warp yarns. Microscopic examination reveals that these cracks appear only in the fill layers and only in the section of the beam between the supports. This is expected since the shear force in the beam should be zero outside the supports.

The same type of microcracks were found in the long ( $L/d = 15$ ) specimens but they were mostly contained between the two warp plies that bracket the center of the laminate. These cracks in the long specimens were generally longer and wider than their counterparts in the short specimens and

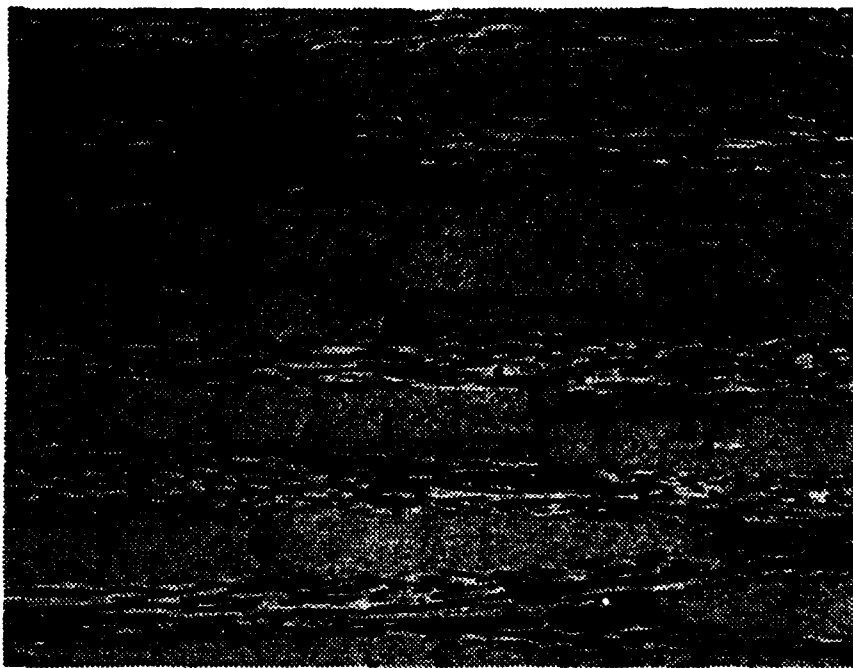


Figure 22(a). 3/16" Right of Center at N.A., Front Face,  
L/d = 15, R = 100%, (50x) (no cracks)

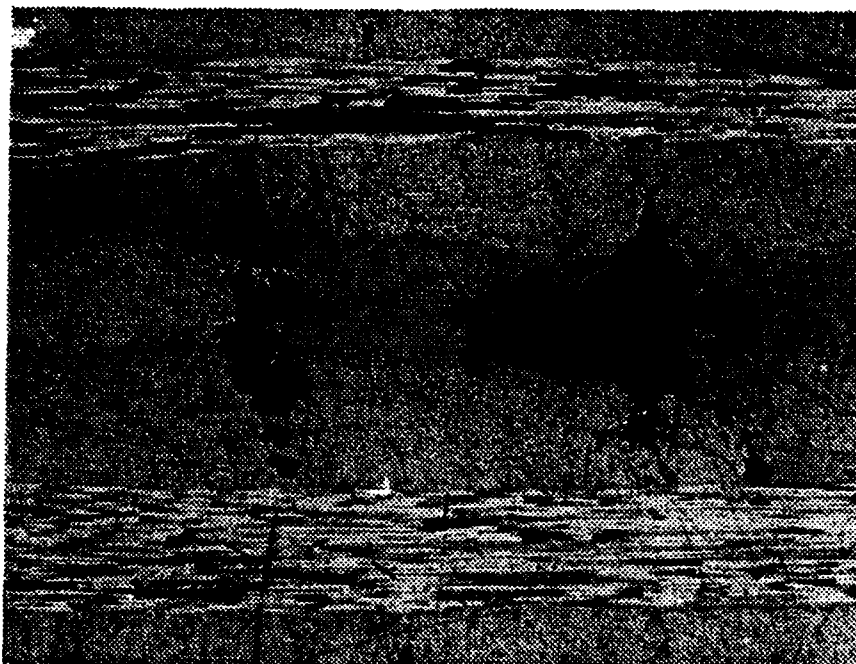


Figure 22(b). 3/16" Left of Center at N.A., Back Face,  
L/d = 15, R = 100%, (100x) (cracked)



Figure 23(a). Cracks Beneath Top Ply, 3/16" Left of Center.  
L/d = 5, #4, R = 100%, (100x)



Figure 23(b). Close-up on Center of Figure 23(a) Above,  
(400x)

were interconnected more than the cracks in the short beams.

During the loading and unloading of the short specimens, no sudden failures were ever observed, just gradual delamination of the plies. In one particular case, an  $L/d = 4$  specimen was loaded far beyond failure to a maximum displacement of about one half of the specimen thickness. Even under this extreme deflection, the short beam specimen did not exhibit any sudden or catastrophic failure.

The long specimens however behaved differently. During testing of the first  $L/d = 15$  specimen, the cross-head motion was reversed just after the applied load reached it's maximum value. A few seconds later, as the cross-head was receding, a loud "snap" was heard from the specimen and a visible "crack" appeared at the surface, running along the mid-plane of the beam. At the same time, there was a sudden decrease in the resisted load indicated by a large discontinuity in the load displacement curve. Additional tests of the long specimens demonstrated that this visible fracture and sudden decrease in resisted load occurred prior to cross-head motion reversal if the reversal was delayed past the point of maximum load. This loud "snap" and visible surface fracture may lead one to incorrectly assume the test induced a single, large shear crack in the laminate as expected for isotropic materials. However, microscopic examination of this visible "crack" reveals it is a

collection of many smaller 45 degree cracks in the fill fiber layer as described above. In the long specimens, some localized shear cracking occurred in the fill fiber layers adjacent to the outer ply fracture mentioned earlier. Between the plies adjacent to the contact points and the neutral axis plies however, the long specimens were generally undamaged.

b. Finite Element Predictions

Using the results of the  $P_{max}$  experiments, an average  $P_{max}$  for each L/d ratio was determined. The next step was to apply this load to the finite element model described in Chapter III. The stress field generated by the model was then analyzed with the combined-stress failure criteria to see if model estimates of damage were consistent with the physical evidence. For P equal to  $P_{max}$  (R = 100%), the L/d = 4 finite element model predicts the stress field shown in Figures 24 and 25. Comparing these fields with Copp's (4) elasticity solutions shown in Figures 8 and 9 indicates the model stress field is well behaved and appears reasonable. Notice that the magnitude of the shear stress contours indicate most of the central elements exceed the 1000 psi material shear strength limit. As described in Chapter III, the stress components were input to both a Tsai-Wu and Tsai-Hill failure criteria to test for exceedance of a "yield" state of stress. Normally, the

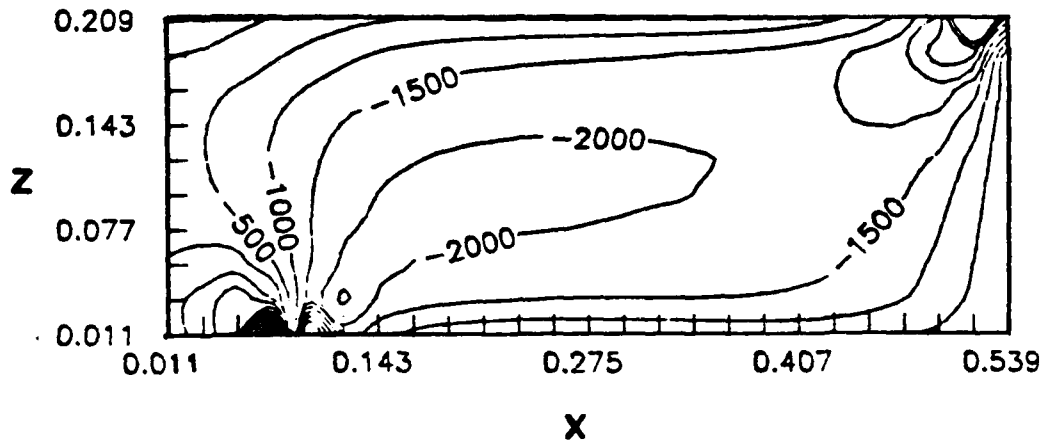


Figure 24. Shear Stress  $\sigma_{xz}$  (psi), Carbon-Carbon,  $N = 500$ ,  
 $R = 100\%$ ,  $L/d = 4$

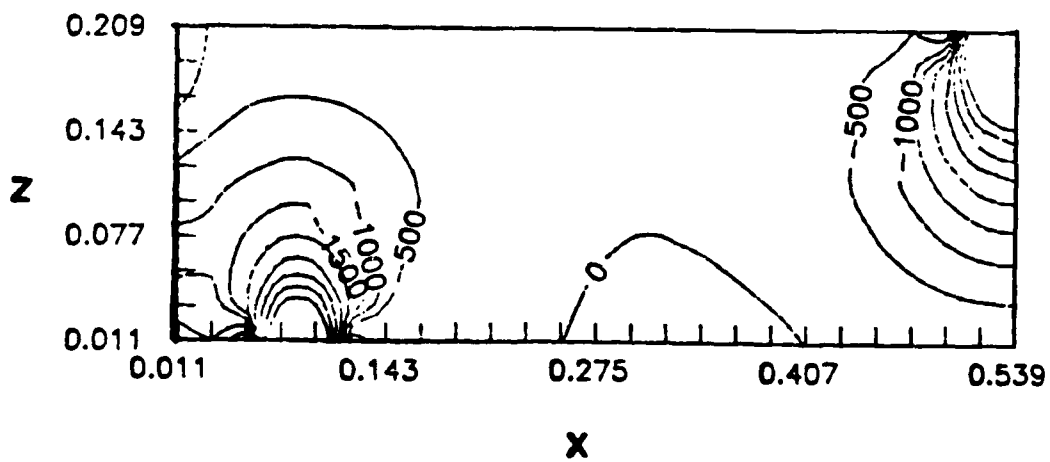


Figure 25. Normal Stress  $\sigma_z$  (psi), Carbon-Carbon,  $N = 500$ ,  
 $R = 100\%$ ,  $L/d = 4$

yield point is reached when the calculated criteria equals one. However, for graphical purposes, the criteria used here subtracted one from the computed value thus zero becomes the yield limit. In this manner, negative values indicate stress below yield and positive values indicate stress above the yield limit. Any contour labeled with a positive value indicates failure of the elements in that region. Figures 26 and 27 show the resulting failure criteria contours for one half of the  $L/d = 4$ ,  $R = 100\%$  model. Comparing Figure 27 to Copp's predicted Tsai-Hill yield contours shown in Figure 28 demonstrates that the finite element based failure contours agree with the elasticity based contours. The corresponding failure contours from the  $L/d = 15$ ,  $R = 100\%$  case are shown in Figures 29 and 30. Keep in mind that two tic marks spaces on the contour plots equals the length of one element and that output from 250 elements are used to derive the contours. According to Figures 26 and 27, the finite element model predicts yielding or failure of about  $3/4$  of the elements when  $P$  equals  $P_{max}$ . This would seem to invalidate the linear elastic continuum assumptions of the model and hence the associated stress results, but the model displacement predictions show otherwise. For example, compare predicted maximum specimen bending displacement and the measured LVDT displacements from the  $P_{max}$  tests listed in Table 5. In these instances,  $P_{max}$  of the model and  $P_{max}$  of

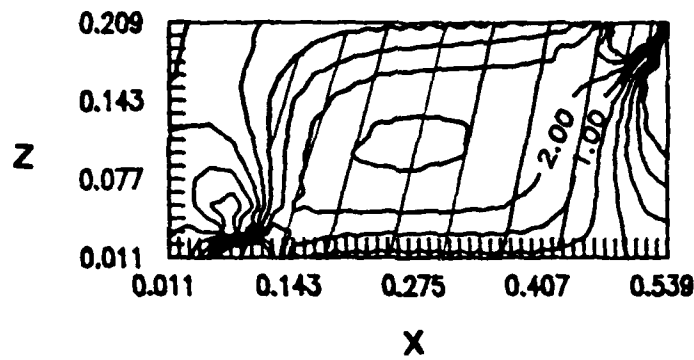


Figure 26. Tsai-Wu Failure Criteria,  $L/d = 4$ ,  $R = 100\%$

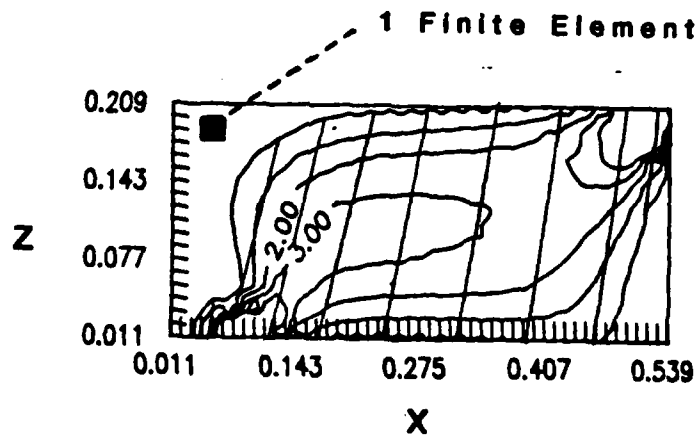


Figure 27. Tsai-Hill Failure Criteria,  $L/d = 4$ ,  $R = 100\%$

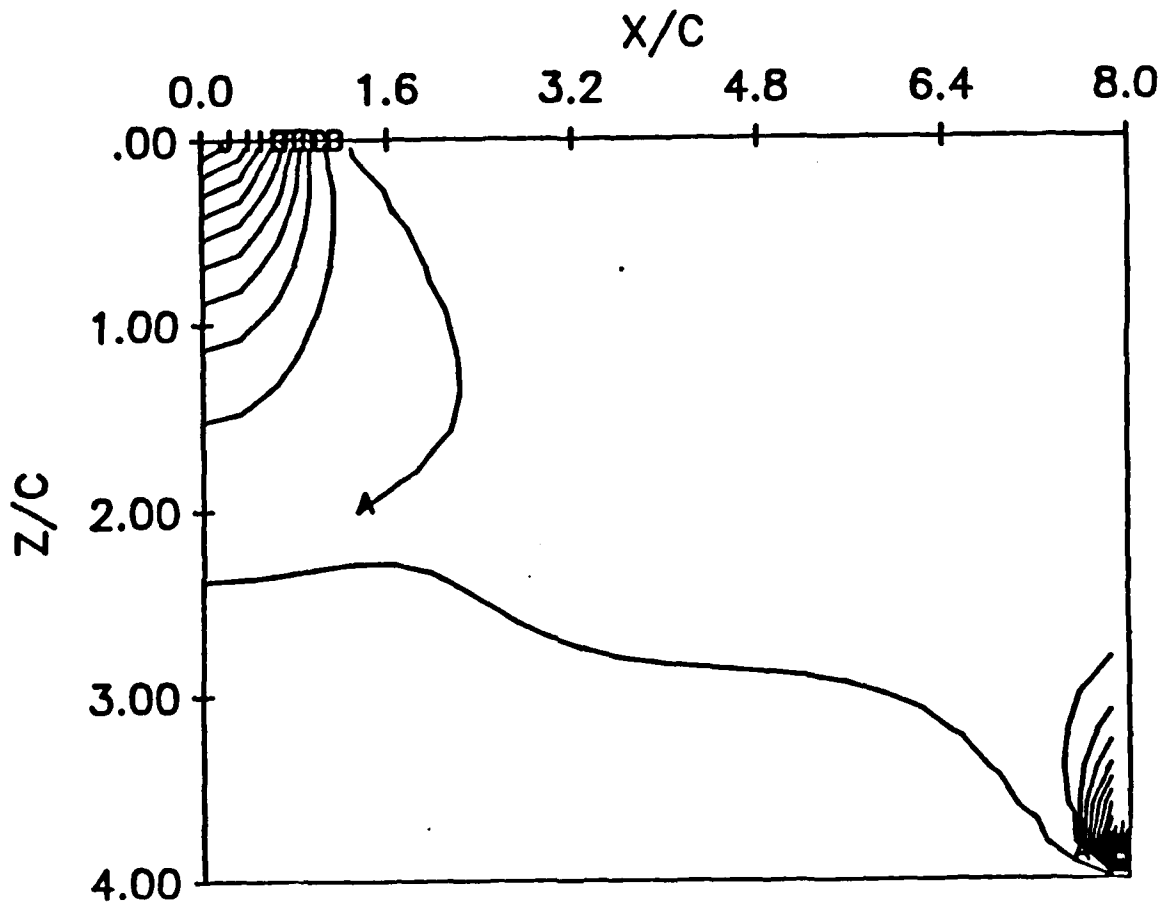


Figure 28. Copp's Exact Elasticity Solution Tsai-Hill Failure Contour (4)

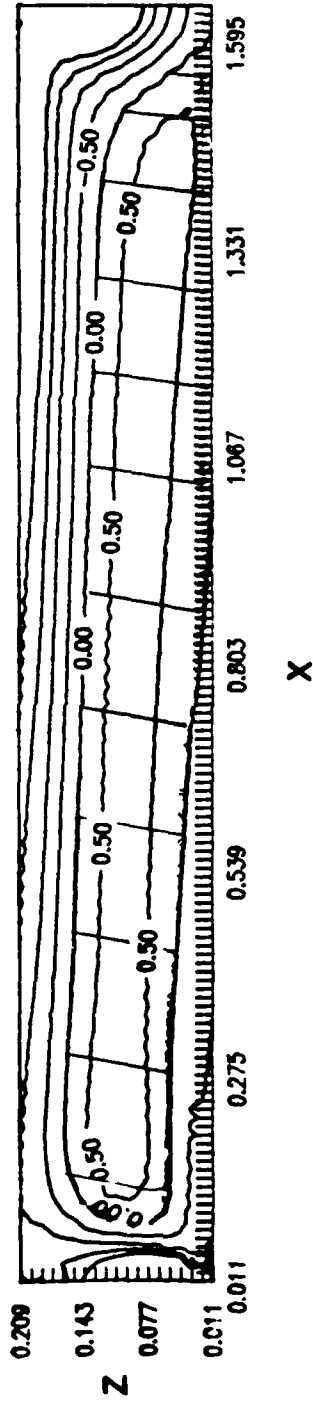


Figure 29. Tsai-Wu Failure Criteria,  $L/d = 15$ ,  $R = 100\%$

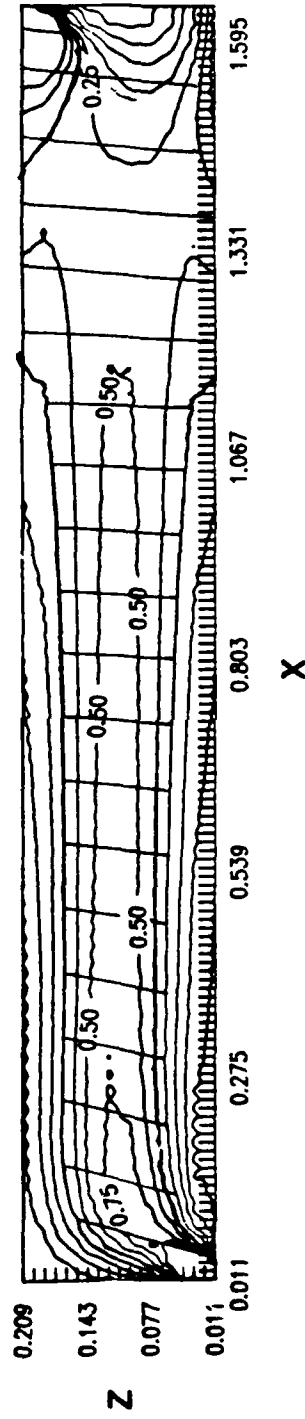


Figure 30. Tsai-Hill Failure Criteria,  $L/d = 15$ ,  $R = 100\%$

Table 5. Experimental and Finite Element Displacements

L/d ratio	LVDT $\delta_{\max}$ (in)	model $\delta_{\max}$ (in)
4	.0056	.0054
15	.0274	.0285

the test specimen differed by less than four pounds. For both the short and long beam models, the predicted max displacement is within only 5% of the measured specimen displacement when the specimen and model failure loads are nearly equal.

Running the finite element model at reduced loads produces the straight line in Figure 31 characteristic of the finite element assumptions. This line matches the accompanying experimental output trace for the  $L/d = 4$  specimen whose maximum load equaled the  $P_{\max}$  value used in the finite element model. Since the finite element stresses are computed from the displacement solution, the close agreement between model and experimental displacements indicates the model is accurate despite the failure contour indications.

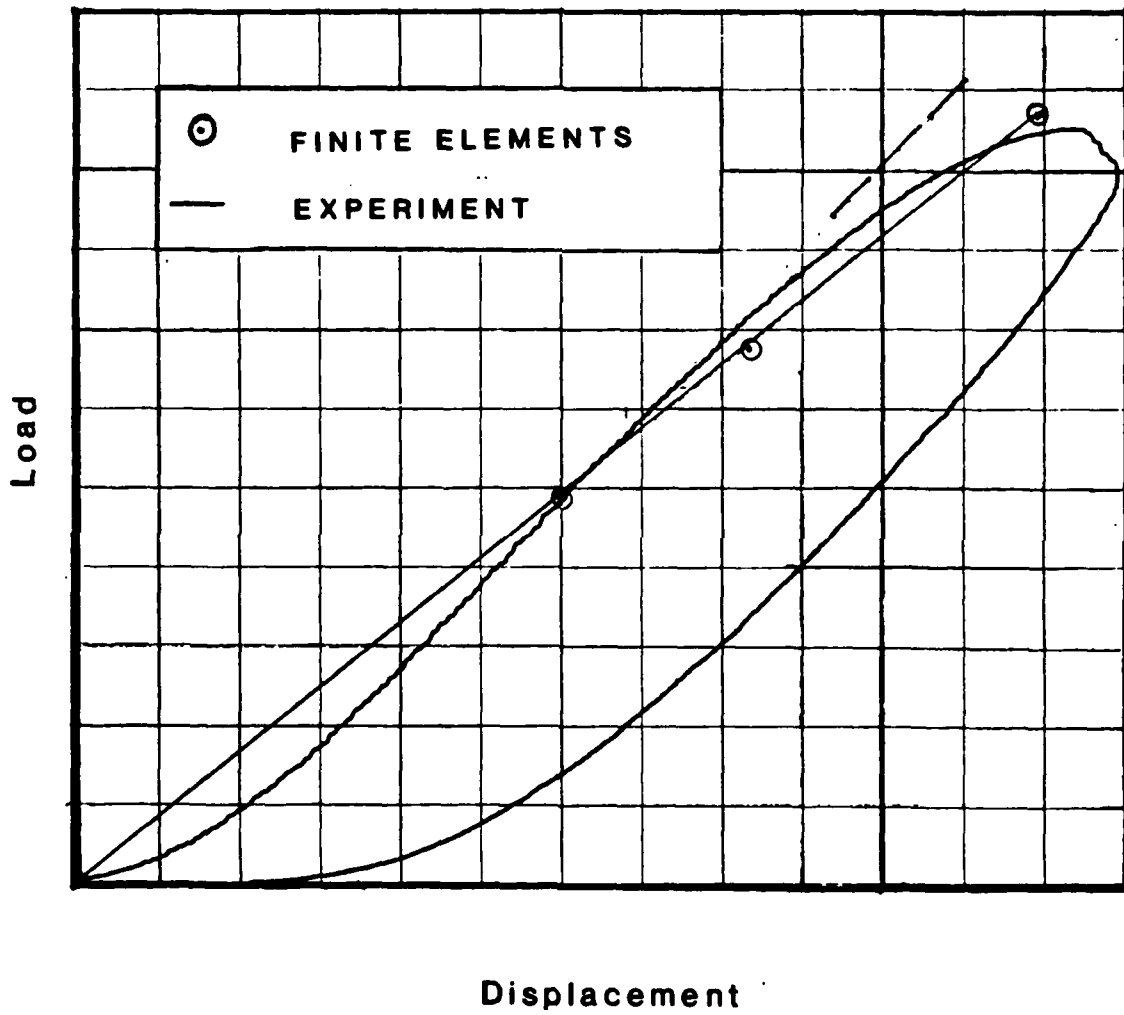


Figure 31. Experimental and Finite Element Load Vs Displacement Curves,  $L/d = 4$

Therefore, according to the models, failure initiation should occur at R of about 50% for a  $L/d = 4$  specimen and at R of about 85% for  $L/d = 15$  specimen. A series of incremental load experiments were conducted to verify this hypothesis.

To test the model further, a series of NASTRAN™ runs were made to generate stress fields and failure contours for  $R = 50\%$  and  $70\%$  to see if it could predict damage initiation. Both failure criteria contours were plotted for the reduced R cases and are shown in Figures 32 through 35. For the short specimen,  $R = 50\%$  produces failure criteria contours where only a small portion of the elements exceed the yield limit. Note that positive (i.e. failed elements) contours are present in the neutral axis regions and indenter/support pin contact regions. Similar results are obtained for the long specimen model with  $R = 85\%$ , where the failed element contours appear only around the neutral axis and indenter contact regions as shown in Figure 36 and 37.

#### c. Incremental Load Experiments

This series of tests were run to initiate damage in the specimens and remove the load before damage progression occurred. After each load/unload cycle, the specimens were examined under the microscope to see if cracks were visible. Due to limited time and material, no long ( $L/d = 15$ ) specimens were available for this test sequence. Only one

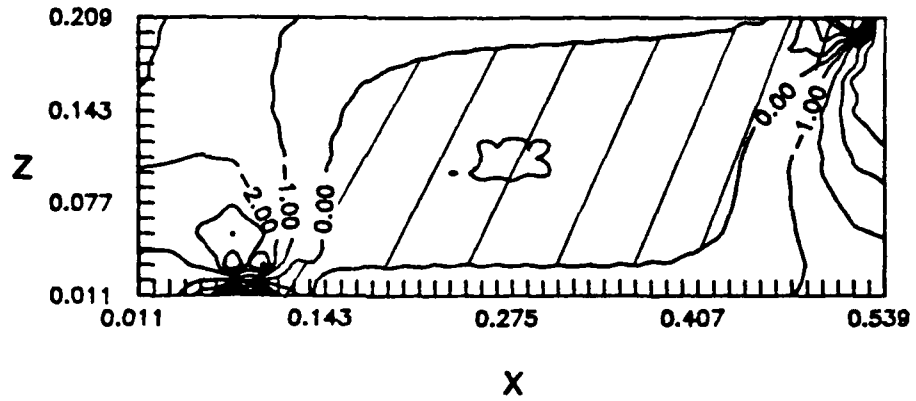


Figure 32. Tsai-Wu Failure Criteria,  $L/d = 4$ ,  $R = 70\%$

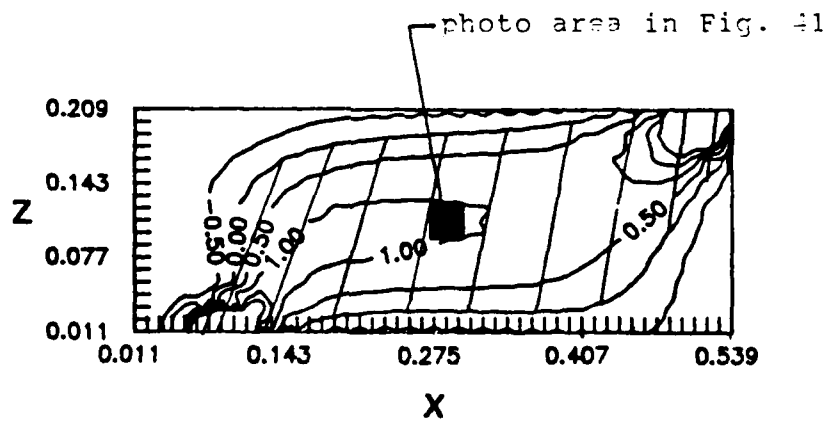


Figure 33. Tsai-Hill Failure Criteria,  $L/d = 4$ ,  $R = 70\%$

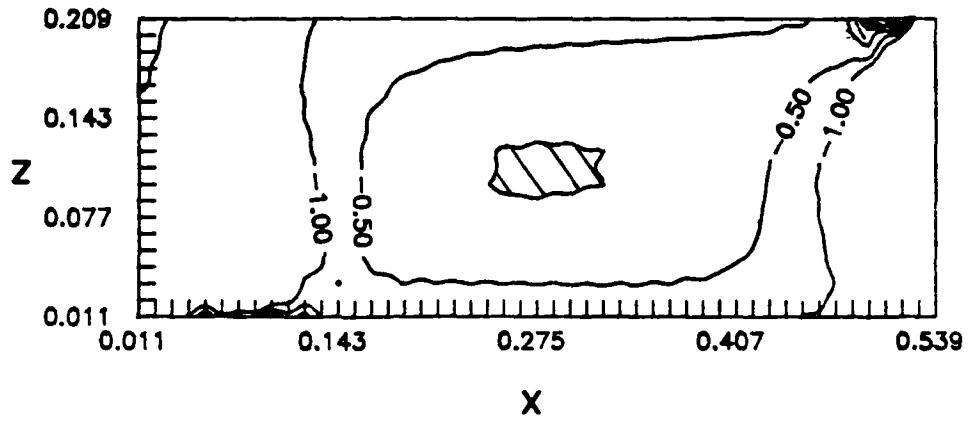


Figure 34. Tsai-Wu Failure Criteria,  $L/d = 4$ ,  $R = 50\%$

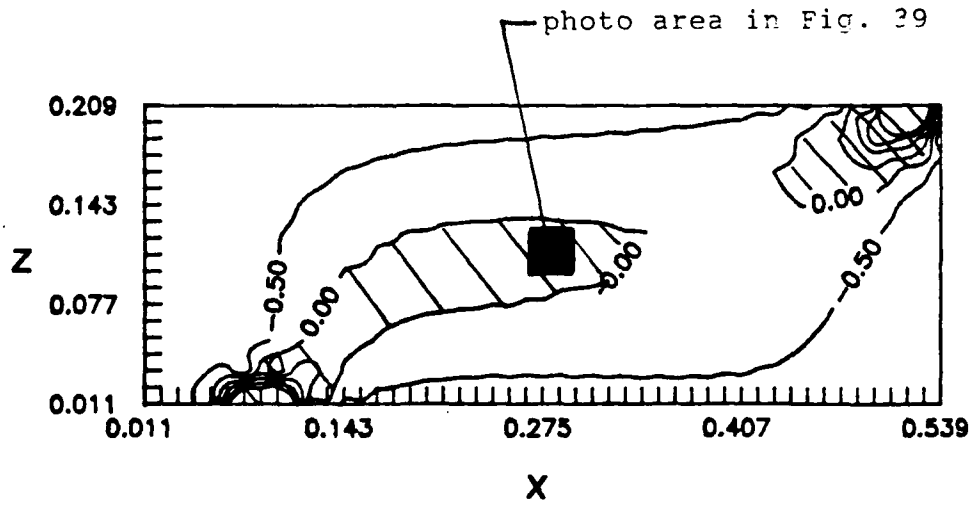


Figure 35. Tsai-Hill Failure Criteria,  $L/d = 4$ ,  $R = 50\%$

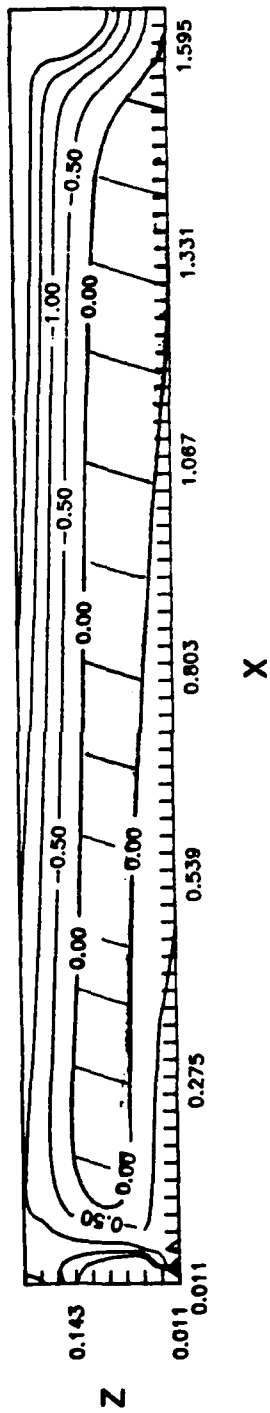


Figure 36. Tsai-Wu Failure Criteria,  $L/d = 15$ ,  $R = 85\%$

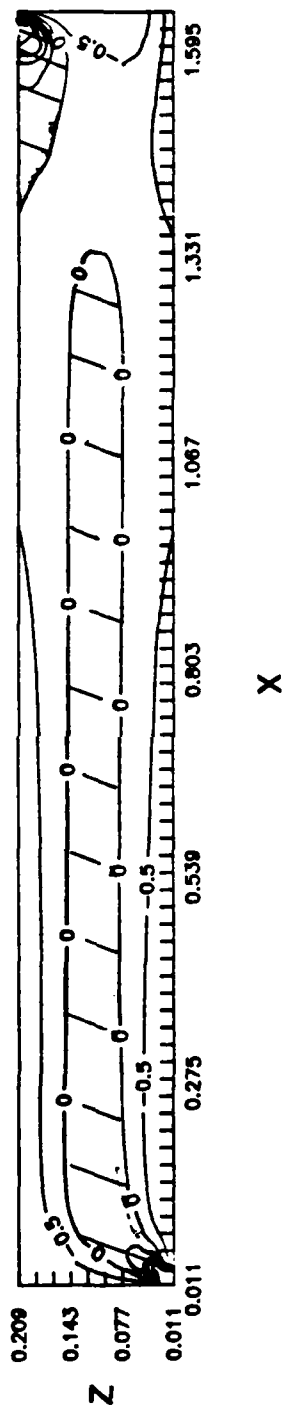


Figure 37. Tsai-Hill Failure Criteria,  $L/d = 15$ ,  $R = 85\%$

specimen at  $L/d = 4$  and one at  $L/d = 5$  were tested. Using the average  $P_{max}$  as the expected failure load, test loads corresponding to the selected R values were computed and used as turn-around points during these tests. For reference, the values are listed in Tables 6 & 7.

After the estimated  $R = 80\%$  tests, both specimens had enough initial damage that additional incremental loading wasn't necessary. Instead, they were loaded to their actual maximum load to see if this value was consistent with earlier  $P_{max}$  test results. Once the actual failure load was known, the estimated R values were corrected to their actual values as shown above. Subsequent reference to R in this section will refer to the actual R value computed once the maximum load was measured. From these tables, one can see the maximum loads attained after the repeated loading and unloading of the specimen are still consistent with the maximum load attained in the direct  $R = 100\%$  tests discussed in section a. of this chapter. This important observation indicates the shifting orientation of a specimen repeatedly inserted and removed from the fixture doesn't affect the overall strength of the specimen.

The repeated removal, reinsertion, and loading of the specimen did not seem to affect the damage pattern in the material either. The only significant difference between the incremental load test damage and the maximum load test damage is that the characteristic outer ply fracture

Table 6. Incremental Load Test Reversal Points, L/d = 4

L/d = 4	Average $P_{max}$ = 300 lbs	
Max Applied Load (lbs)	Estimated R (%)	Actual R (%)
139	50	45
167	60	54
222	80	72
300	100	90
310	111	100

Table 7. Incremental Load Test Reversal Points, L/d = 5

L/d = 5	Average $P_{max}$ = 275 lbs	
Max Applied Load (lbs)	Estimated R (%)	Actual R (%)
133	50	48
160	60	57
186	70	66
212	80	76
270	100	95
280	105	100

occurred at the right support pin rather than at the indenter for both specimens. Figure 38, showing the bottom ply split half way through the thickness, was taken after the  $L/d = 4$  specimen was loaded to only 45% of  $P_{max}$ . Despite this fracture, no indications of damage appeared on the load-displacement curve. High magnification views of the neutral axis plies failed to uncover any "shear" cracks. But cracks less than 5 fiber diameters ( $\approx 40 \mu m$ ) long and  $1/2$  a fiber diameter ( $\approx 4 \mu m$ ) wide were probably undetectable, even with the 1000X lens.

Reinserting and loading the specimen to 54%  $P_{max}$  also produced no indications of damage on the experimental output trace. However, micrographs of the specimen detect fine cracks in the neutral axis layers about 0.25" right of the midspan as seen in Figure 39. For comparison, the photo region in Figure 39 ( $R = 54\%$ ) is depicted on the  $R = 50\%$  predicted failure criteria contour in Figure 35. Note that this micrograph crack is inside the failure limit shown by the zero contour in Figure 35.

Loading the specimen to 72%  $P_{max}$  produced even more visible damage. Micrographs taken after this test show the outer ply warp fibers completely fractured through the thickness (Figure 40). In addition, Figure 41 shows longer "shear" cracks near the neutral axis at 0.25" right of midspan (same area as Figure 39). Correlating the location of this photo with the failure contours for  $R = 70\%$  shown in

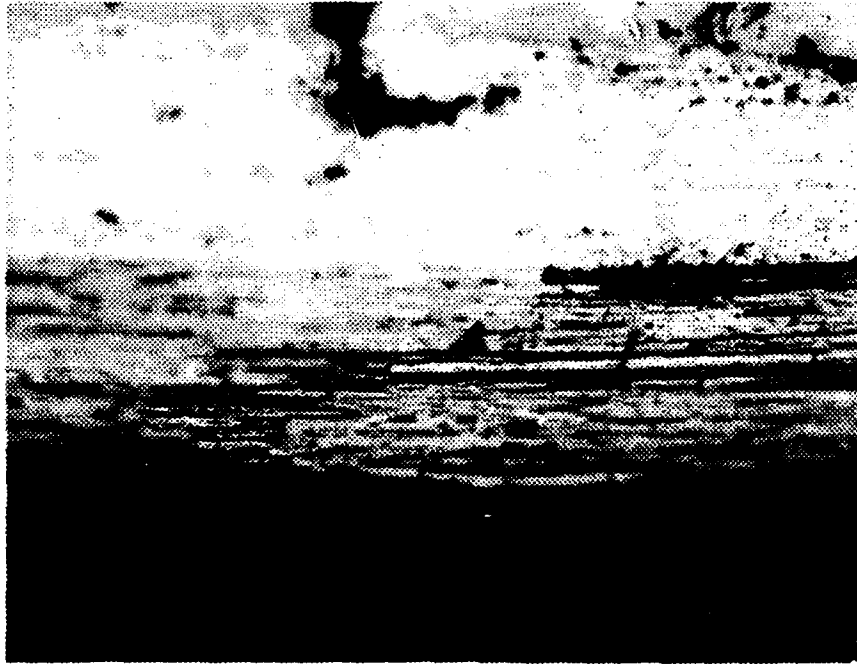


Figure 38. Outer Ply Fracture at Right Support Pin,  
 $L/d = 4$ ,  $R = 45\%$ , (200x)



Figure 39. Initial Cracks at N.A., 1/4" Right of Center.  
L/d = 4, R = 54%, (400x)



Figure 40. Outer Ply Fracture at Right Support Pin,  
L/d = 4, R = 72%, (1000x)



Figure 41. Crack in N.A. Layer, 1/4" Right of Center,  
L/d = 4, R = 72%, (400x)

Figure 33, and  $R = 50\%$  shown in Figure 35 indicates the photo area is within the  $+ 1.0$  and  $0.0$  contours respectively which demonstrates that the model can accurately predict failure in actual specimens.

## V. Conclusions and Recommendations

Two-dimensional, uncoated, ACC-4 advanced Carbon-Carbon composite specimens were experimentally loaded in an ASTM-2344 three-point bend test in order to find where failure initiates for this material in this common test. Failure load and damage indications were recorded on load versus maximum specimen displacement curves. In all, fourteen specimens, divided by length into three categories, were evaluated in the experiments. Over 200 total Optical or SEM photomicrographs of the polished sides of the specimens were taken before and after the experiments to document the type of damage encountered in the specimens. To compliment the experimental study, NASTRAN™ linear elastic finite element models of the specimens were built and successfully used to model experimental displacements. Stress fields were then computed with the models and Tsai-Hill and Tsai-Wu failure criteria were used to evaluate the stress field in order to predict yield or failure initiation.

The experimental portion of this study has shown that three point bend failures of C/C composites are complex and asymmetrical with respect to the cross-section and width of the specimen. Cracks may propagate to the surface on one face of the specimen but not the opposite face, even when extensive damage is present in the structure. In all

specimens tested, the outer plies fractured in the vicinity of the indenter and support pins used in the bend test. The amount of load required to induce this fracture is a function of the bend specimen test length, and for short specimens is as little as 50% of the maximum sustained load. Micrographs also show that gross laminate failures in long test specimens is really a series of smaller, localized matrix cracks along the neutral axis which start as separate cracks and interconnect as the load is increased. This indicates that the "non-linear" appearance of C/C load versus displacement curves is really a manifestation of the internal damage and not indicative of the material behavior. In fact, despite the significant amount of internal damage created when loading above 50% of the maximum load, C/C material response remains generally linear.

Linear elastic finite element models of the test specimens support this since they predict beam displacements within 5% of the actual measured displacements despite the formation of numerous matrix cracks in the test specimens. In addition, failure criteria contour plots derived from the model stress field can be successfully used to predict matrix crack initiation. Failure contours for the short beam show only a few elements in the model exceed the criteria when the applied load is 50% of  $P_{max}$  which is consistent with experimental results.

To further study damage initiation in Carbon-Carbon

composites, similar experiments should be conducted with laminates other than the purely orthotropic laminate considered here. Specimens should be polished on both the front and back face so that each may be examined under the microscope since cracks don't always propagate equally to the outer surfaces. Scanning Electron Microscope (SEM) photos of the specimens are valuable and should also be used in such a study. Caution must be used when interpreting SEM photos though since the C/C specimens tend to "charge" around voids, warp/fill fiber interfaces, and cracks which creates white spots on the photo.

Additional experiments should also be conducted using larger indenter and support pin diameters to evaluate the indenter size and load effects. Indenter and support pins should be sized to force the highest stress concentration at the indenter to limit the number of specimen regions where damage could start. Using an indenter pin twice the diameter of the support pins as listed in the ASTM-2344 three point bend test creates equal stresses at the contact areas which complicates the post-test microscopic analysis of the specimens.

Parametric studies of the finite element model response to drastic changes in material properties would also be useful since there appears to be significant variance in the reported material property values. The effects of varying shear strength would be particularly interesting since the

shear strength is so weak for this material and seems to have the greatest influence on damage initiation.

Finally, additional step load testing of bend specimens is recommended. Data from such tests, combined with the data generated in this thesis, may provide enough information to determine if the net displacement offset shown in the load-displacement curves after unloading is a measurable indication of internal damage.

## Bibliography

1. Ambartsumyan, S. A. Theory of Anisotropic Plates. Stamford, CN: Technomic Publishing Company, 1970.
2. American Society for Testing and Materials 1985 Annual Book of ASTM Standards, Section 15, Volume 15.03. Philadelphia, PA (55-58)
3. Cook, Robert D. Concepts and Applications of Finite Element Analysis (Second Edition). New York: John Wiley & Sons, 1981.
4. Copp, Paul D. Smooth Contact of a Rigid Indenter and a Beam of Two Orthotropic Layers. PhD dissertation, Northwestern University, Evanston, Il. December, 1986.
5. Hill, R. The Mathematical Theory of Plasticity. London: Oxford University Press, 1950.
6. Iannuzzi, Francesco A., Stuart H. Starret, and Mark A. Sherman, Evaluation of Carbon-Carbon Composites for Advanced Turbine Engine Application: Final Report, June 1983 - January 1987. US Air Force Contract F33615-82-C -5105 with Southern Research Corporation. Materials Laboratory, Air Force Wright Aeronautical Laboratories, Air Force Systems Command, Wright-Patterson AFB, OH February 1988
7. Jones, Robert M. Mechanics of Composite Materials. New York: Hemisphere Publishing Corporation, 1985.
8. Lekhnitskii, S. G. Theory of Elasticity of an Anisotropic Elastic Body. (translated by P. Fern) San Francisco: Holden-Day Inc., 1963.
9. Leong, K. and J. Zimmer, Fiber Property Changes During Processing of Carbon-Carbon Composites, (Acurex Corporation) AFWAL-TR-86-4016, Materials Laboratory, Air Force Wright Aeronautical Laboratories, AFSC, Wright-Patterson AFB, OH June 1986. (AD-B013-414)
10. Miller, R. J., C. H. Huang, and K. F. Tosi, "Composite Attachments and Interfaces," (Oral Presentation) US Air Force Contract F33615-83-C2328, 7 October 1987

11. NASA, The NASTRAN™ Theoretical Manual, NASA SP-221(6), Wasington, DC January 1981.
12. NASA, The NASTRAN™ User's Manual, NASA SP-221(7), Wasington, DC June 1985.
13. "Other Engineering Materials; Manufactured Carbon," Machne Design 17: 292-297 (14 April, 1988, Materials Reference Issue)
14. Pagano, N. J. "Exact Solutions for Composite Laminates in Cylindrical Bending," Journal of Composite Materials, 3: 398-411 (July 1969)
15. Pagano, N. J. "Influence of Shear Coupling in Cylindrical Bending of Anisotropic Laminates," Journal of Composite Materials, 4: 330-343 (July 1970)
16. Pagano, N. J. and A. S. D. Wang "Further Study of Composite Laminates Under Cylindrical Bending," Journal of Composite Materials, 5: 521-528 (October 1971)
17. Robinson, C. T. Damage Mechanisms and Failure of 3-D Carbon-Carbon Composites, Final Report US Navy Contracts N00014-77-C-0510 and N00014-81-C-0023, San Antonio, TX: Southwest Research Institute, May 1981 (AD-B058-634L)
18. Rosensaft, M. and G. Marom "Evaluation of Bending Test Methods for Composite Materials," Journal of Composite Technology and Research, 7/1: 12-16 (Spring 1985)
19. Southern Research Institute, Mechanical and Thermal Properties of Carbon-Carbon Materials. Data Report SRI-EAS-87-799-5802-3, US Army Contract DASG60-84-C-0081, Southern Research Institute, Birmingham, AL: September 1987
20. Starret, H. Stuart An Evaluation of the Tensile Properties of an Uncoated and Coated 2-D Carbon-Carbon Composite (Vought ACC-4) (Southern Research Institute) AFWAL-TR-84-4145 Materials Laboratory, Air Force Wright Aeronautical Laboratories, Air Force Systems Command, Wright-Patterson AFB, OH December 1984.

21. Stuchly, S. L., D. C. Larsen, and S. A. Bortz  
Evaluation of Carbon/Carbon Materials for Turbine Engine Applications AFWAL-TR-86-4057 Materials Laboratory, Air Force Wright Aeronautical Laboratories, AFSC, Wright-Patterson AFB, OH September 1986.
22. SURFER™ Users Manual, Golden Software, Golden CO.
23. Szaruga, Stephen L. "Four Point Flexure (Shear) Testing of Structural Carbon-Carbon Composites." An open address to local Scientists and Engineers, Air Force Wright Aeronautical Laboratories, Wright-Patterson AFB, OH 12 September 1988.
24. Tsai, Stephen W. Composites Design. (Third Edition) Dayton, OH: Think Composites Publishing Company, 1987
25. Tsai, Stephen, W.; "Strength Theories of Filamentary Structures," in R. T. Schwartz and H. S. Schwartz (eds) Fundamental Aspects of Fiber Reinforced Plastic Composites New York: Wiley Interscience, 1968.
26. Tsai, Stephen W. and H. Thomas Hahn Introduction to Composite Materials. Westport: Technomic Publishing Company, 1980.
27. Tsai, Stephen, W. and Edward M. Wu "A General Theory of Strength for Anisotropic Materials," Journal of Composite Materials, 5: 58-80 (January 1971)
28. Whitney, J. M. "The Effect of Transverse Shear Deformation on the Bending of Laminated Plates," Journal of Composite Materials, 3: 534-547 (July 1969)
29. Whitney, J. M. "Elasticity Analysis of Orthotropic Beams Under Concentrated Loads," Composites Science and Technology, 22: 167-184 (1985)
30. Whitney, J. M. and C. E. Browning, "On Short Beam Shear Tests for Composite Materials," Experimental Mechanics, 25: 294-300 (1985)
31. Whitney, J. M. and R. J. Dauksys "Flexure Experiments on Off-Axis Composites," Journal of Composite Materials, 4: 135-137 (January 1970)
32. Wu, Edward M. "Optimal Experimental Measurements of Anisotropic Failure Tensors," Journal of Composite Materials, 6: 472-489 (October 1972)

Appendix A: NASTRAN™ Input File for L/d=4 Model

```
NASTRAN BANDIT=0, TITLEOPT=-1
ID DENDIS, THESIS PROJ
APP DISP
TIME 25
SOL 1
CEND
$
TITLE= 2-D 3-Pt Bend Model, Full Span, (2) 150 lb loads, L/D=4
SUBTITLE= 500 CQDMEM1 ELEMENTS, (11 x 51 grid)
LABEL= ACC-4 (.022 X .022 X .440 elements)
ECHO=SORT
$ set 4 = neutral axis elements
$ set 5 = support nodes
$ set 10 = half-beam displacements (nodes)
$ set 11 = half-beam stress (elements)
SET 4=200,THRU,300
SET 5=5.47
SET 10= 1 thru 26,101 thru 126,201 thru 226,301 thru 326,
        401 thru 426,501 thru 526,601 thru 626,
        701 thru 726,801 thru 826,901 thru 926,
        1001 thru 1026
SET 11= 1 thru 25,51 thru 75,101 thru 125,151 thru 175,
        201 thru 225,251 thru 275,301 thru 325,
        351 thru 375,401 thru 425,451 thru 475
SPC=701
SPCFORCES=5
OLOAD=ALL
DISPLACEMENT(PRINT)=10
STRESS(PRINT.PUNCH)=11
LOAD=610
$
BEGIN BULK      $ (DATA CARDS)
$
SPC1,701,123456,47
SPC1,701,23456,5
SPC1,701,2456.1.2.3.4
SPC1,701,2456.6,THRU,46
SPC1,701,2456.48,49,50,51
SPC1,701,2456,101,THRU,151
SPC1,701,2456,201,THRU,251
SPC1,701,2456,301,THRU,351
SPC1,701,2456,401,THRU,451
SPC1,701,2456,501,THRU,551
SPC1,701,2456,601,THRU,651
SPC1,701,2456,701,THRU,751
SPC1,701,2456,801,THRU,851
```

```

SPC1,701,2456,901,THRU,951
SPC1,701,2456,1001,THRU,1051
$
FORCE,610,1025,0,150.,0.,0.,-1.0
FORCE,610,1026,0,150.,0.,0.,-1.0
$
PQDMEM1,801,901.,440.,
$      ACC-4 2-D orthotropic [Q] stiffness coeff's
MAT2,901,16.667+6.,09375+6,..46875+6,..20+6.,095,+M2A
+M2A.....25.+3,15.+3.,75+3
$      GRID and CQDMEM1 cards start here
$      don't forget "ENDDATA" card at end of deck
GRID,  1.,  0.  ,  0.  ,  0.  ,
GRID,  2., 0.022,  0.  ,  0.  ,
GRID,  3., 0.044,  0.  ,  0.  ,

.

GRID, 50., 1.078,  0.  ,  0.  ,
GRID, 51., 1.100,  0.  ,  0.  ,
GRID,101.,  0.  ,  0.  ,  0.022,
GRID,102., 0.022,  0.  ,  0.022,
GRID,103., 0.044,  0.  ,  0.022,

.

GRID,1050., 1.078,  0.  ,  0.220,
GRID,1051., 1.100,  0.  ,  0.220,
CQDMEM1,  1, 801,  1,  2, 102, 101
CQDMEM1,  2, 801,  2,  3, 103, 102
CQDMEM1,  3, 801,  3,  4, 104, 103

.

CQDMEM1, 50, 801, 50, 51, 151, 150
CQDMEM1, 51, 801, 101, 102, 202, 201

.

CQDMEM1, 499, 801, 949, 950,1050,1049
CQDMEM1, 500, 801, 950, 951,1051,1050
ENDDATA

```

---

Appendix B: Failure Criteria Section of the L/d = 4 Model  
Post Processor FORTRAN code

```

C          read inputs from NASTRTAN "punch" file output
C
C          Note: only half of the elements used due to symmetry
C          Do loop increments should add to 1/2 total elements
C          NELINCR=Number of Element Increment
C          SIG1MAX, etc. used in computing values for '*.fc2'

READ(7,7001)
NELINCR=0
SIG1MAX=0.
SIG3MAX=0.
SIG13MAX=0.
DO 40 L=1,10,1
  DO 30 M=1,25,1
    N=M+NELINCR

C          read in element stress values from NASTRAN output
      READ(7,7002) NELM(N),SIGX(N),SIGZ(N),SIGXZ(N),
&          SIG1(N),SIG3(N),SIG13(N)

      IF (ABS(SIG13(N)).GT.SIG13MAX) SIG13MAX=SIG13(N)
      IF (ABS(SIG1(N)).GT.SIG1MAX) SIG1MAX=SIG1(N)
      IF (ABS(SIG3(N)).GT.SIG3MAX) SIG3MAX=SIG3(N)

30      CONTINUE
      NELINCR=NELINCR+50
40      CONTINUE

C          read in Material Stress limits from '*.mat'
      READ(4,*) XT,XC,ZT,ZC,S

C          compute values for Tsai-Wu criteria
      F1=1./XT+1./XC
      F2=1./ZT+1./ZC
      F6=0.
      F11=-1./(XT*XC)
      F22=-1./(ZT*ZC)
      F66=+1./(S*S)

C          use Tsai-Hahn approximation for F12
      F12=-1./(2*SQRT(XT*XC*ZT*ZC))

C          Tsai-Wu Failure Criteria -> TWU(N)      ---
C          or
C          Tsai-Hill Failure Criteria -> THILL(N)   | + = FAILED
C          (compression based, X=XC)              | < 0 = @ LIMIT
C                                                  | - = SAFE
C                                                  ---

```

```

C
C           write inputs to data base for SURFER -- 5 Col's max!
C           Note: only half of the elements used due to symmetry

WRITE(8,8001)
WRITE(9,9001)
WRITE(10,10001)
WRITE(11,11001)

C           Do loop increments should add to 1/2 total elements
C           NINCR=Number of Element Increment
NINCR=0
DO 140 L=1,10,1
  DO 130 M=1,25,1
    N=M+NINCR

C           Compute Tsai-Wu and Tsai-Hill criteria
TWU(N)=F1*SIGX(N)+F2*SIGZ(N)+F6*SIGXZ(N)+F11*(SIGX(N))**2
&      +F22*(SIGZ(N))**2+F66*(SIGXZ(N))**2+2*F12*SIGX(N)*SIGZ(N)-1.0

THILL(N)=(SIGX(N)**2)/(XC*XC)-(SIGX(N)*SIGZ(N))/(XC*XC)
&      +(SIGZ(N)**2)/(ZC*ZC)+(SIGXZ(N)**2)/(S*S) -1.0

C           write output to various data base files
WRITE(8,8003) XBAR(N),ZBAR(N),SIGX(N),SIGZ(N),SIGXZ(N),NELM(N)
WRITE(9,9003) XBAR(N),ZBAR(N),SIG1(N),SIG3(N),SIG13(N),NELM(N)
WRITE(10,10003) XBAR(N),ZBAR(N),TWU(N),THILL(N),NELM(N)
WRITE(11,11003) XBAR(N),ZBAR(N),SIG1(N)/SIG1MAX,SIG3(N)/SIG3MAX,
&      SIG13(N)/SIG13MAX,NELM(N)

130      CONTINUE
        NINCR=NINCR+50
140      CONTINUE
.
.
.

```

---

Appendix C: Experimental Raw Output Data

This Appendix contains reduced copies of the original 11" x 17" X-Y plotter traces of all load cell and LVDT output voltages for the three-point bend experiments. The plotter axes are scaled in Volts per inch as indicated on each different plot. In each case, load cell voltages are along the y-axis and LVDT voltages are along the x-axis. Load cell and LVDT calibration curves are included as Figures 42 and 43 respectively to permit conversion of voltage readings from the raw output traces to actual load in pounds or displacement in inches. Based on these calibration curves, the actual equations used to compute load and displacement magnitudes were:

$$\text{Load (lbs)} = \frac{\{\text{Output Voltage (mv)} + .37 \text{ (mv)}\}}{1.6138 \text{ (mv)/(lb)}} \quad (15)$$

$$\text{Displacement (in)} = \text{Output Voltage (mv)} \frac{0.0001 \text{ (in)}}{11 \text{ (mv)}} \quad (16)$$

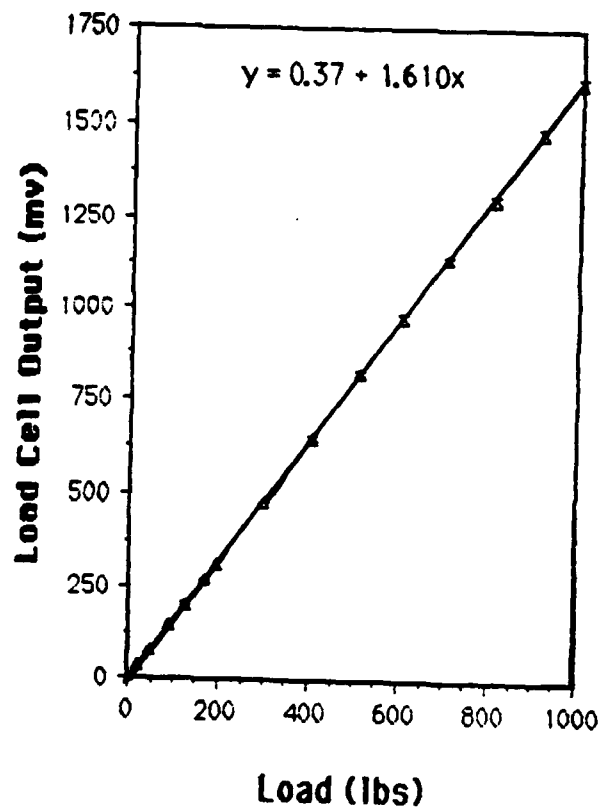


Figure 42. SM-1000 Load Cell Calibration Curve

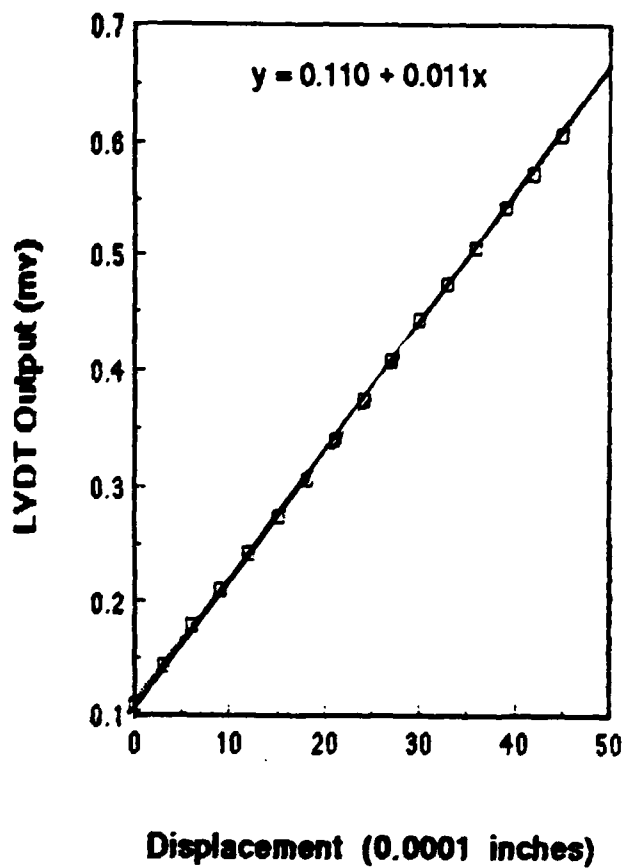


Figure 43. RH 225A-300 LVDT Calibration Curve

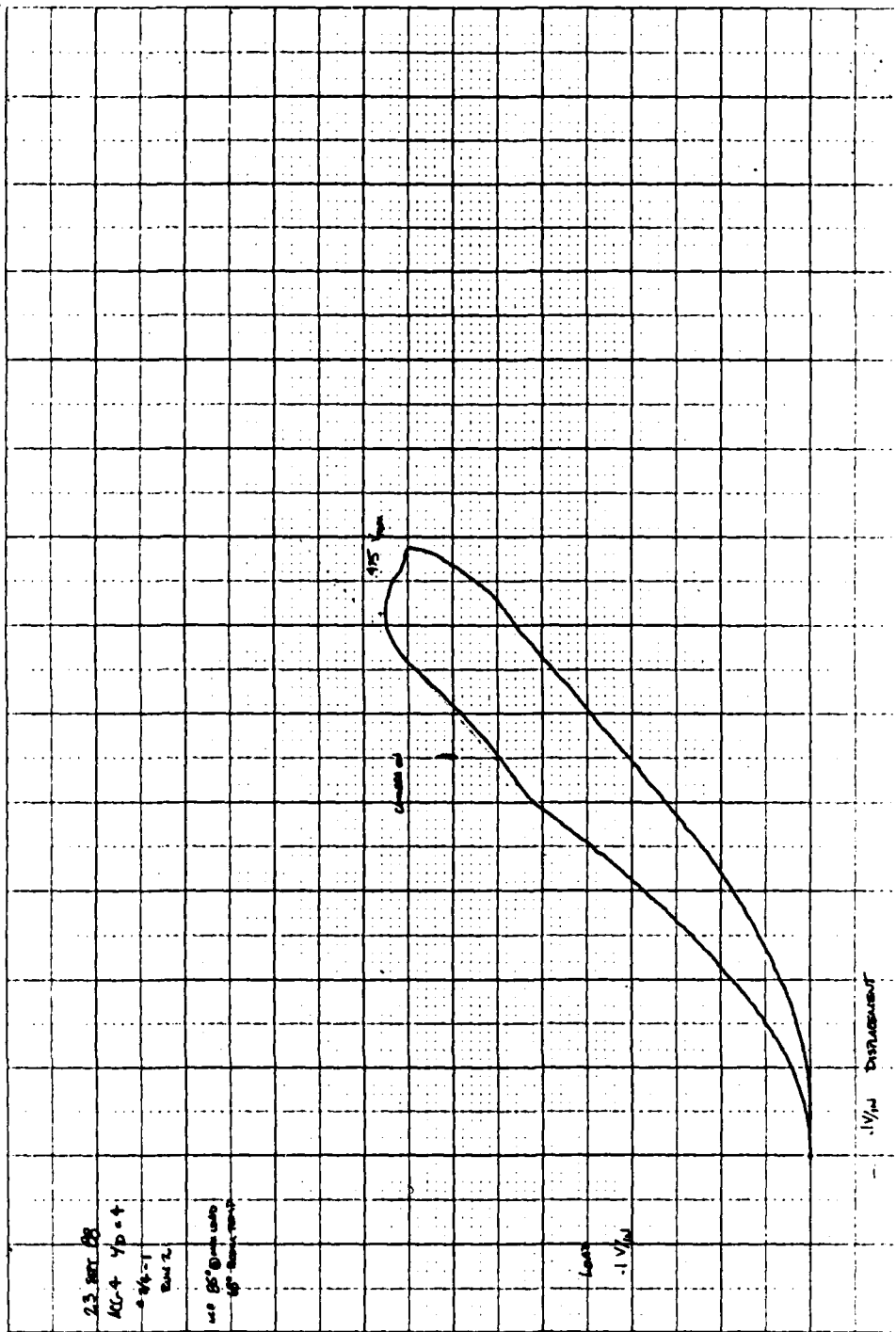


Figure 44. Load-Displacement Curve, Specimen 2/4-1, R=100%

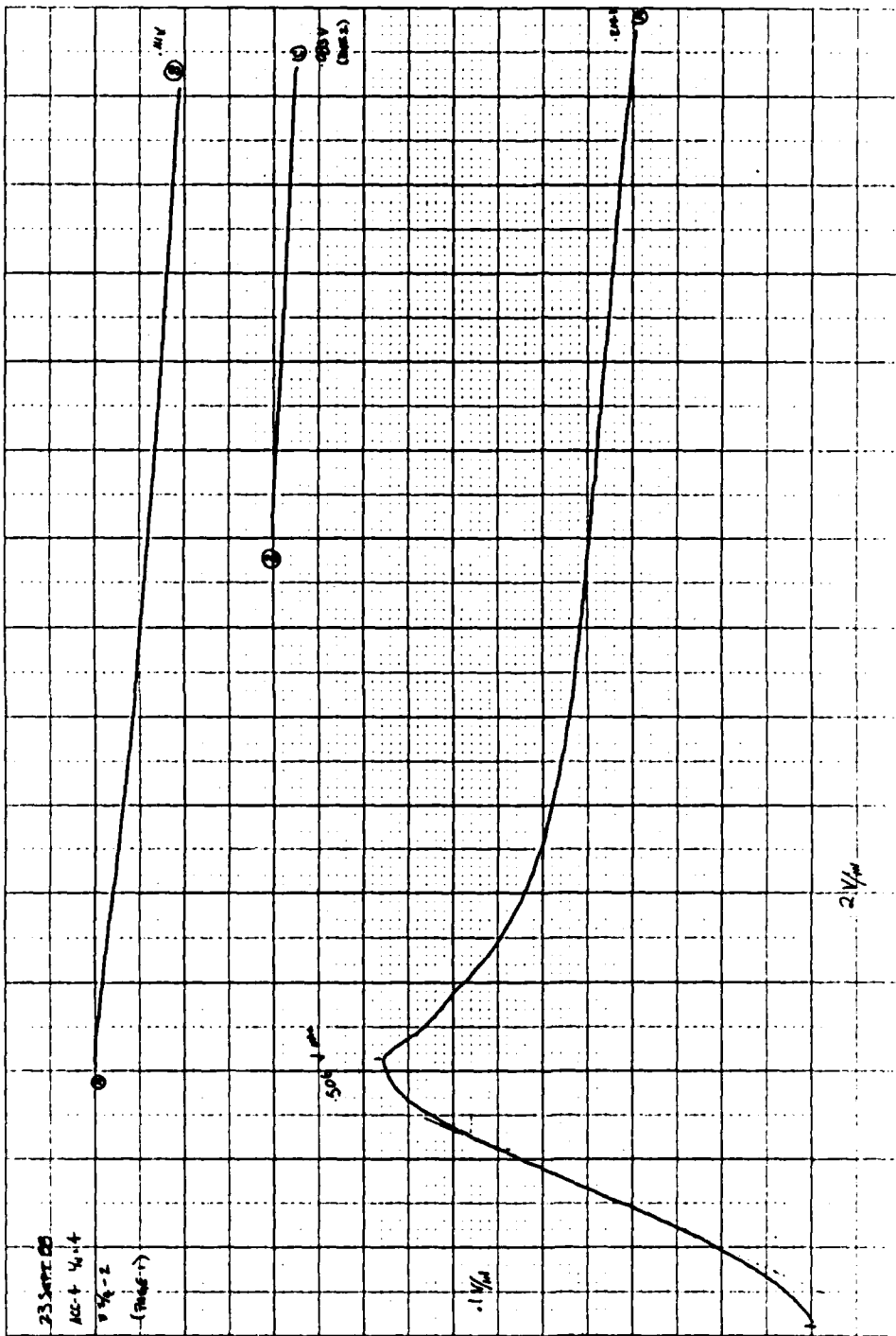


Figure 45. Load-Displacement Curve, Specimen 2/4-2, R=100%

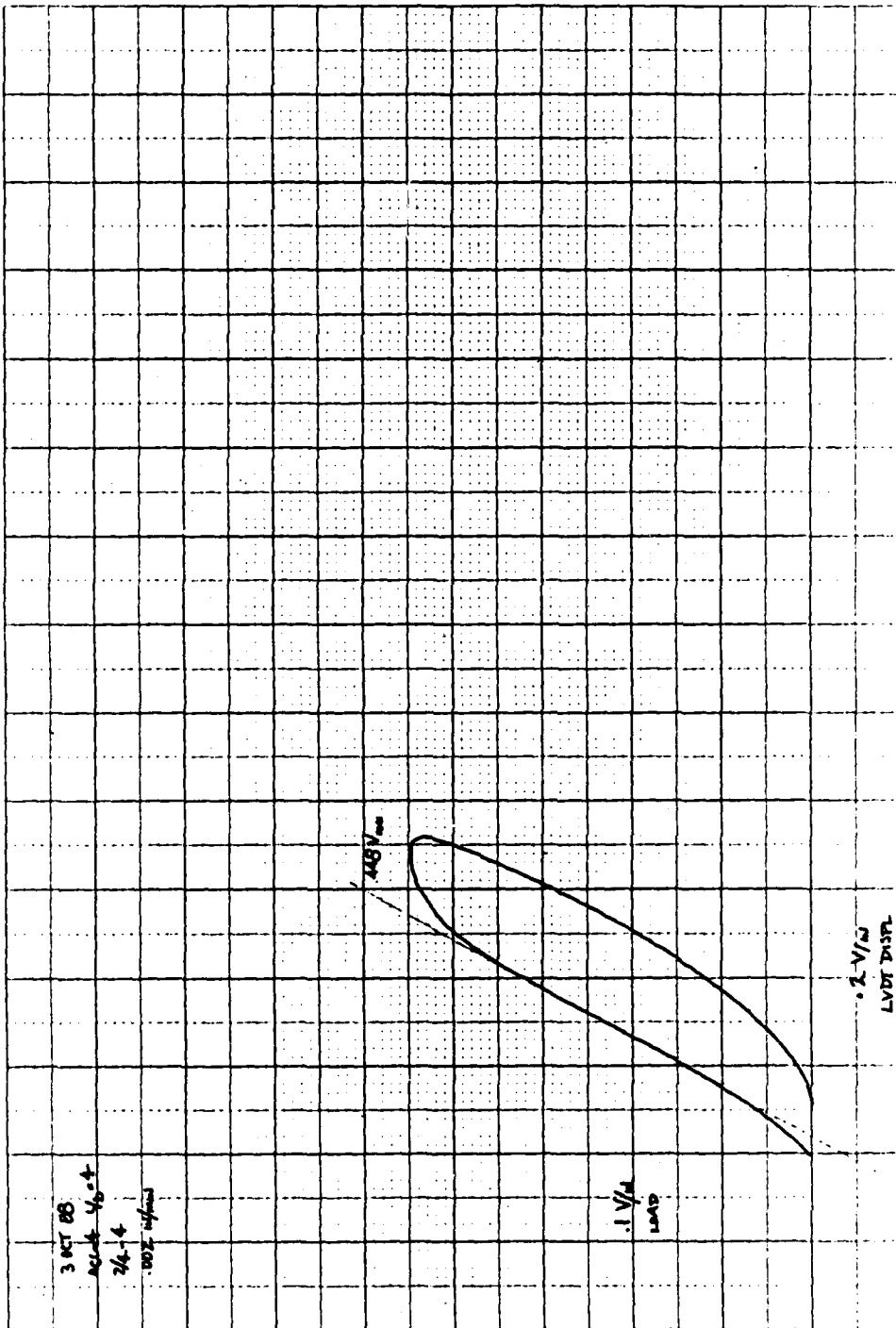


Figure 46. Load-Displacement Curve, Specimen 2/4-4, R=100%

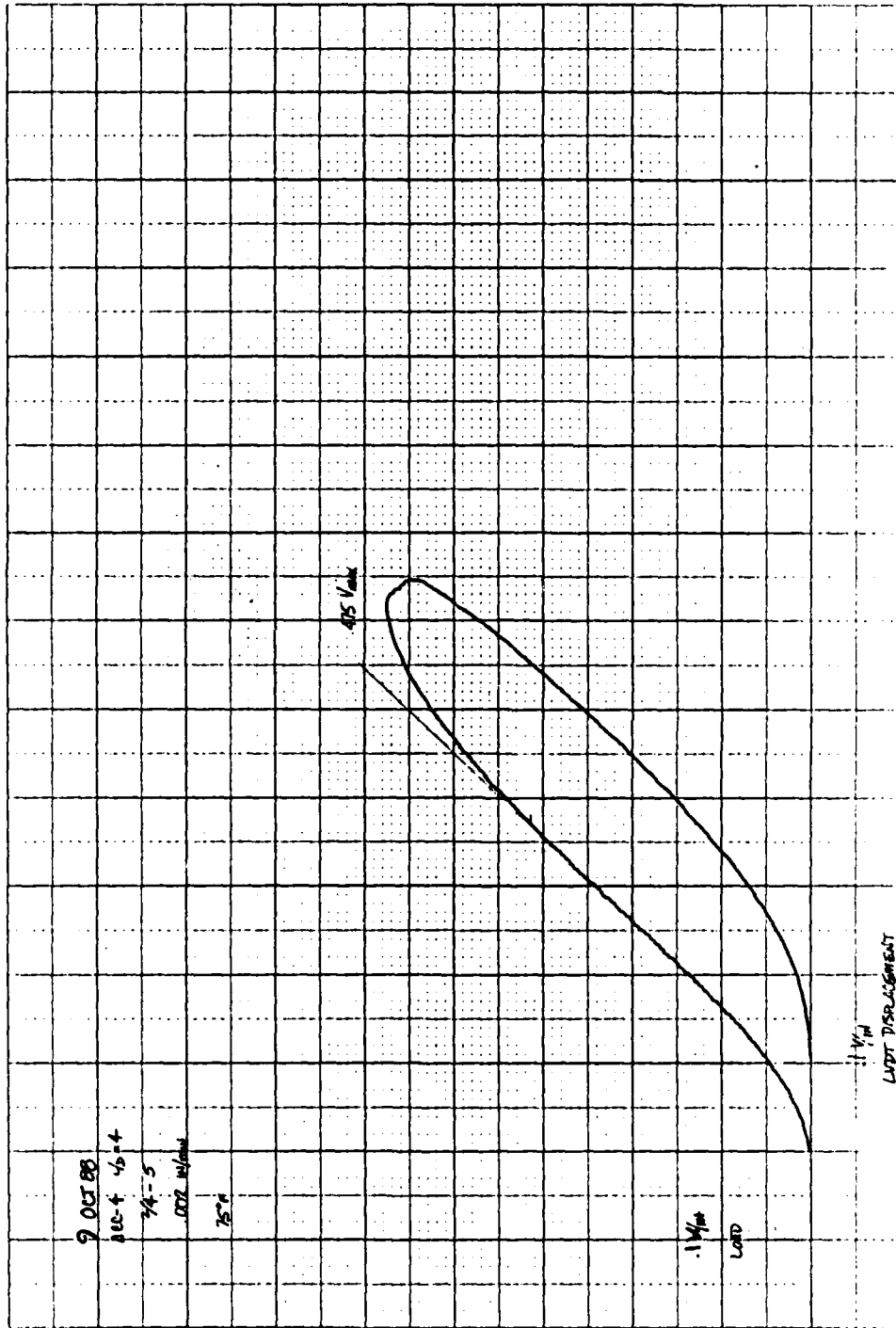


Figure 47. Load-Displacement Curve, Specimen 2/4-5, R=100%

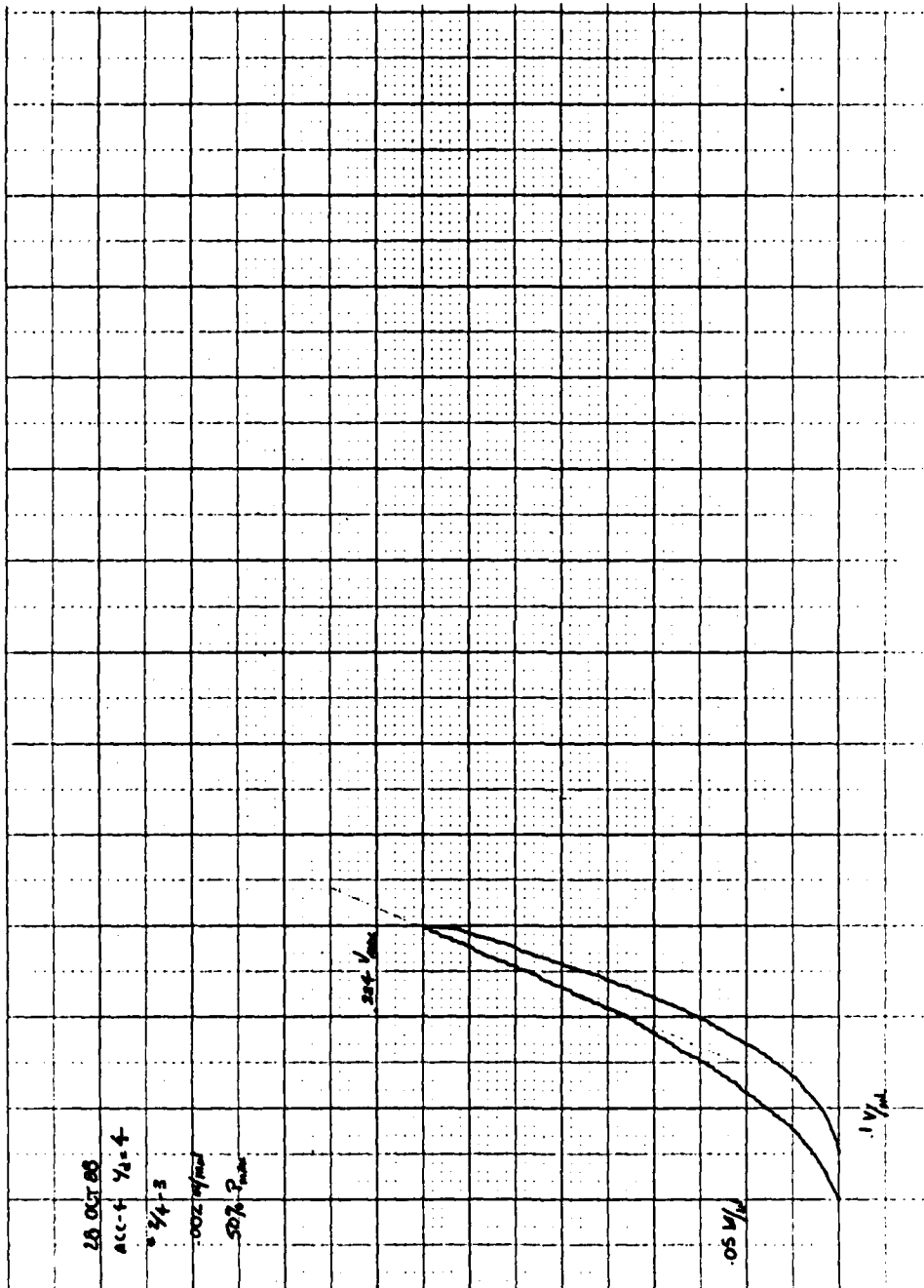


Figure 48. Load-Displacement Curve, Specimen 2/4-3, R=50%

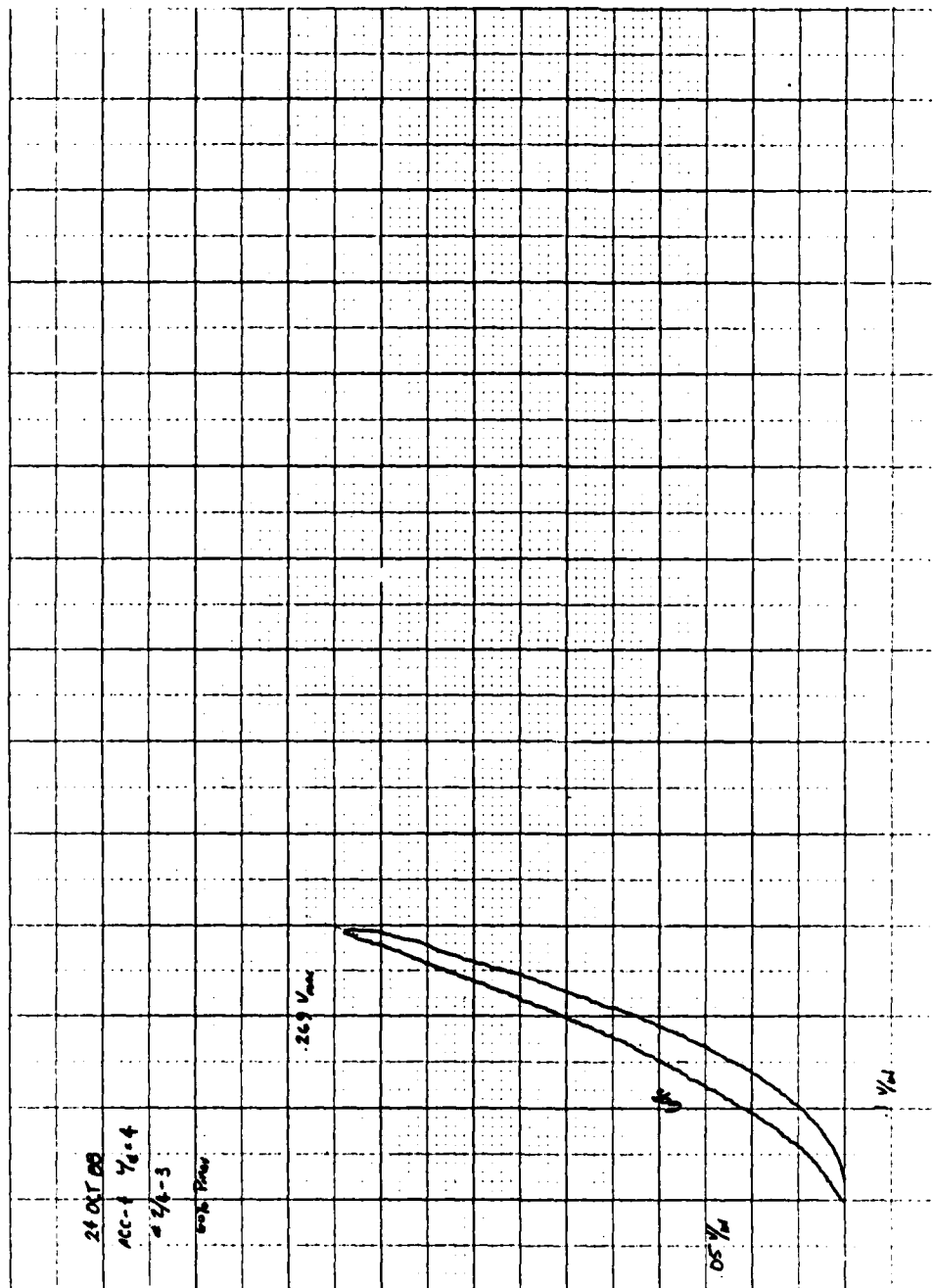


Figure 49. Load-Displacement Curve, Specimen 2/4-3, R=60%

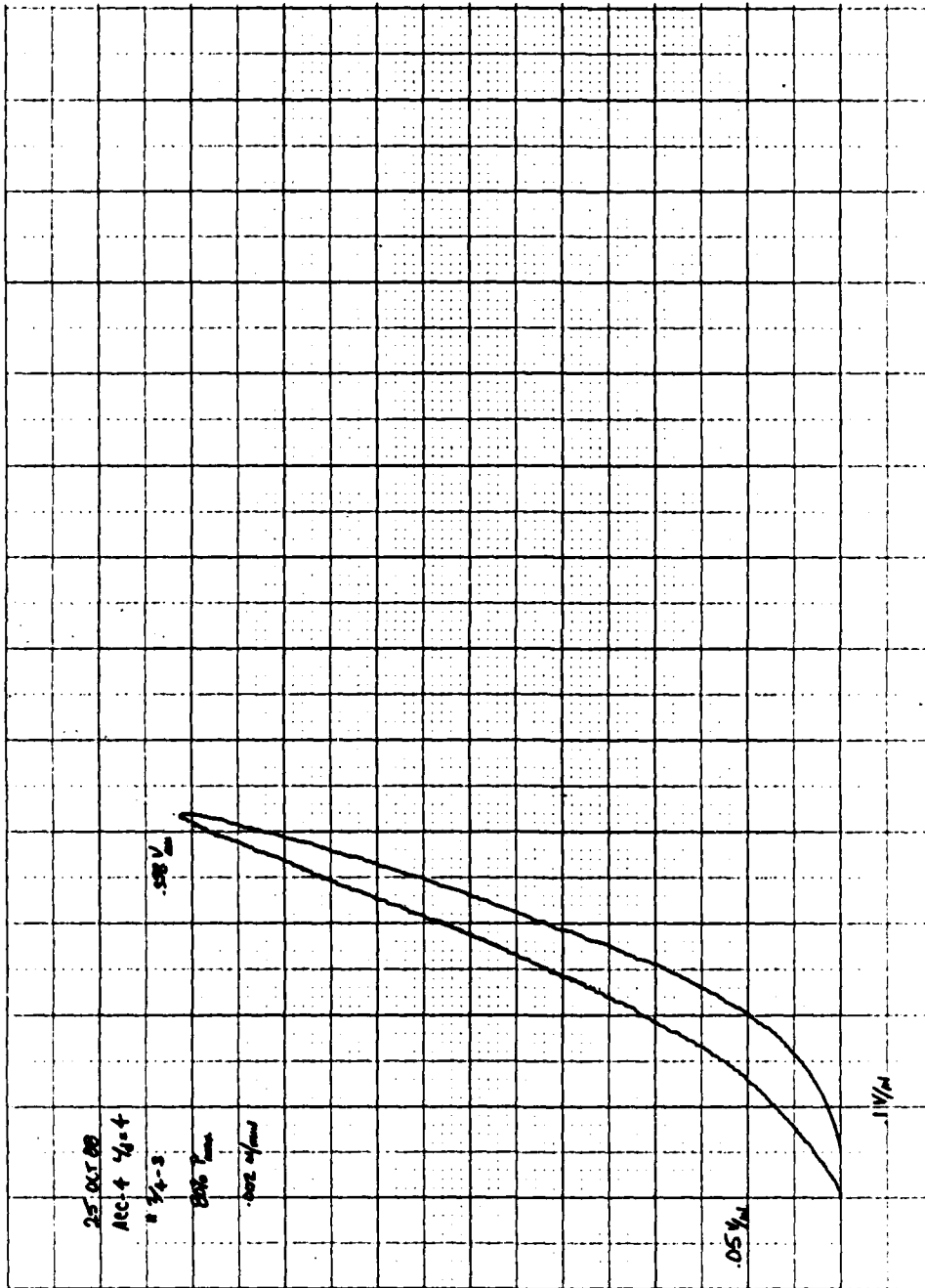


Figure 50. Load-Displacement Curve, Specimen 2/4-3, R=80%

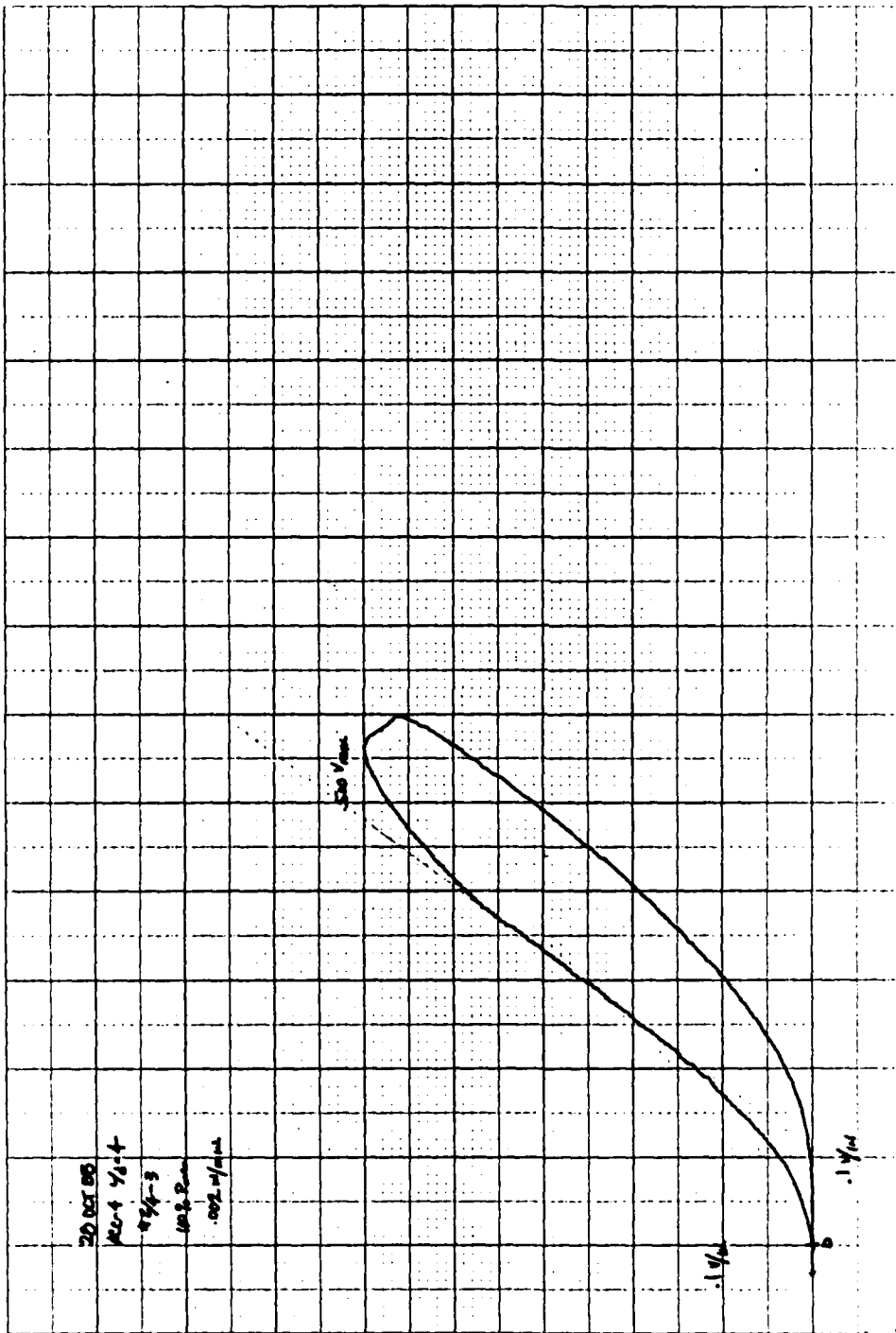


Figure 51. Load-Displacement Curve, Specimen 2/4-3, R=100%

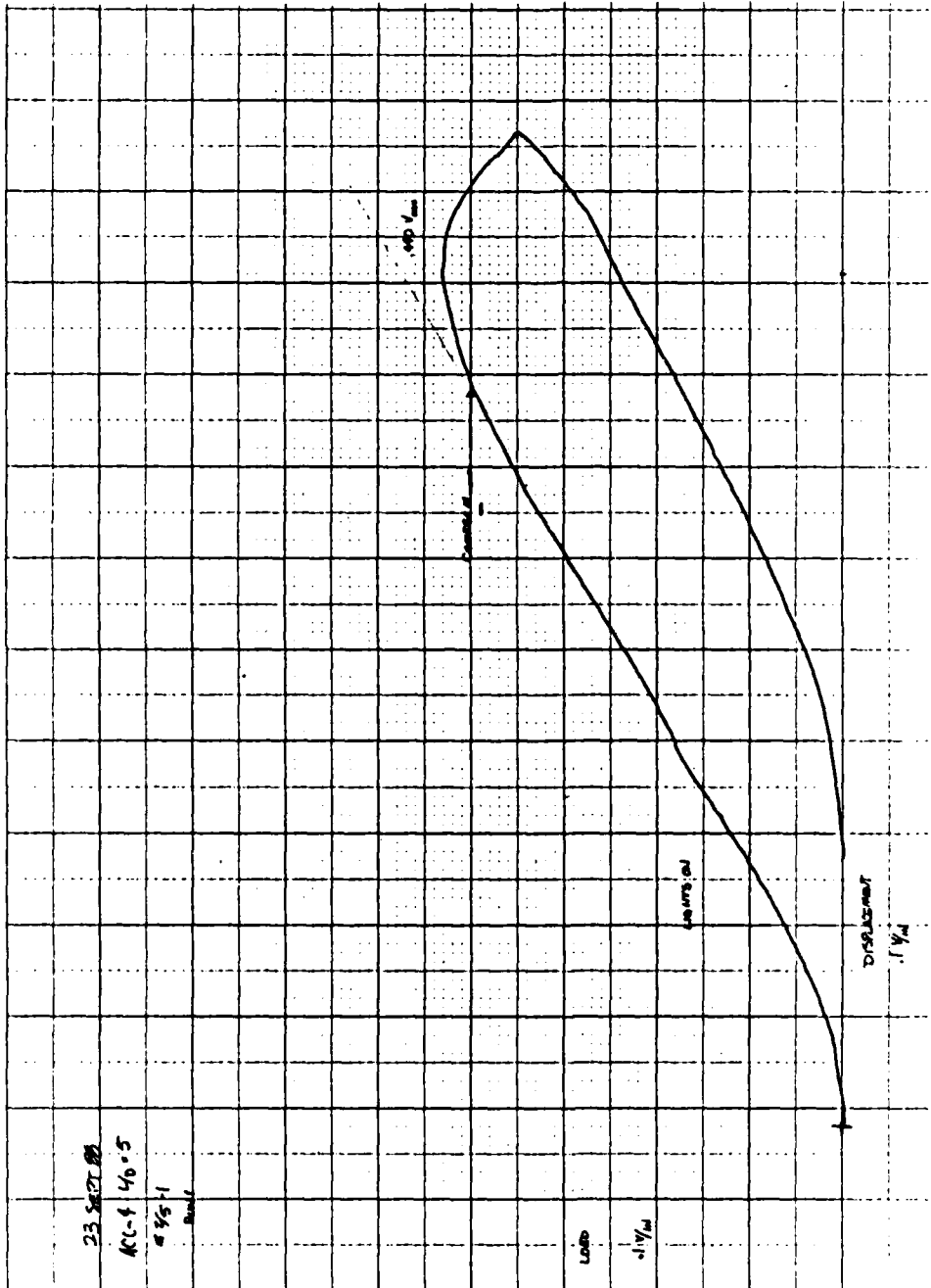


Figure 52. Load-Displacement Curve, Specimen 2/5-1, R=100%

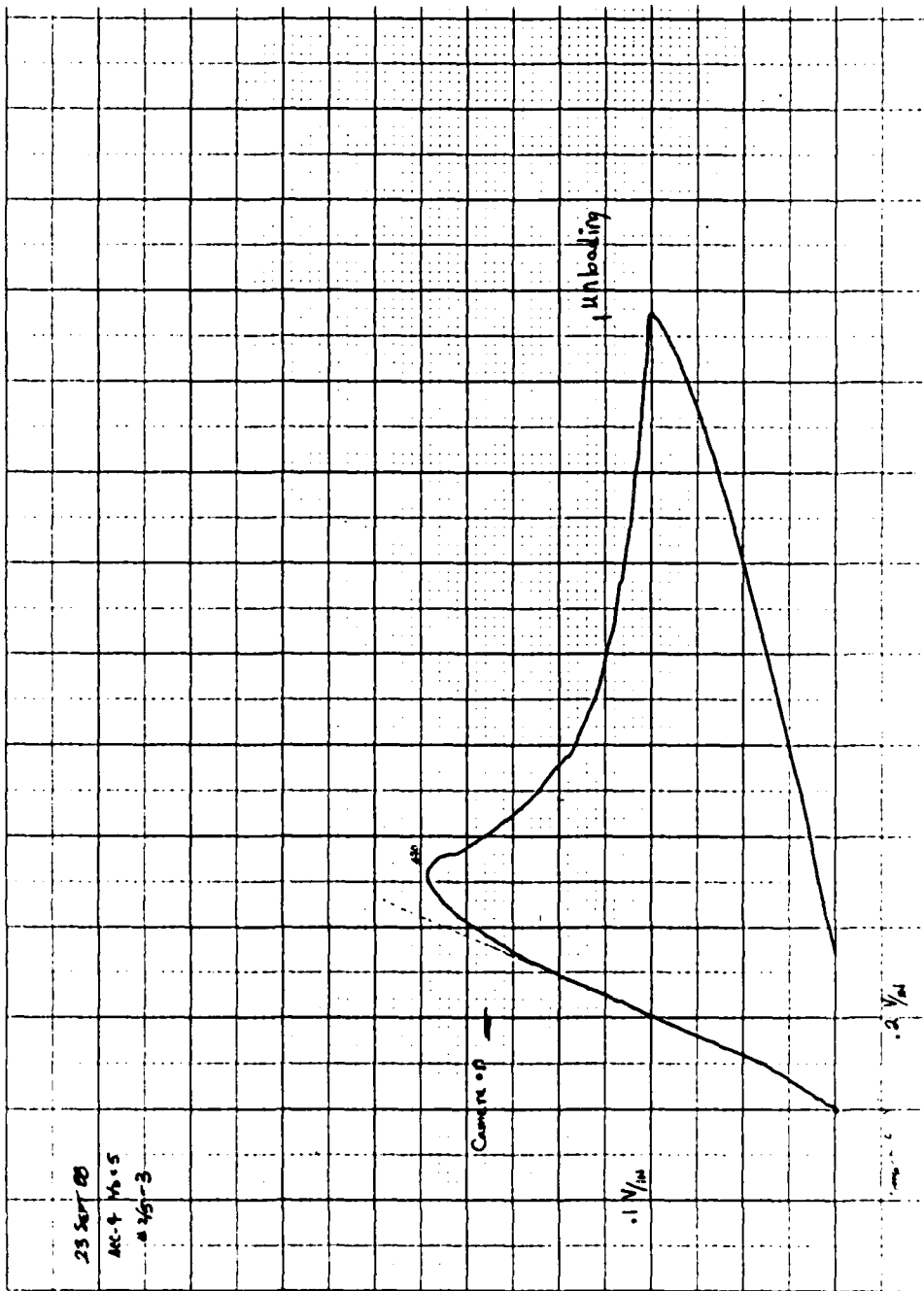


Figure 53. Load-Displacement Curve, Specimen 2/5-3, R=100%

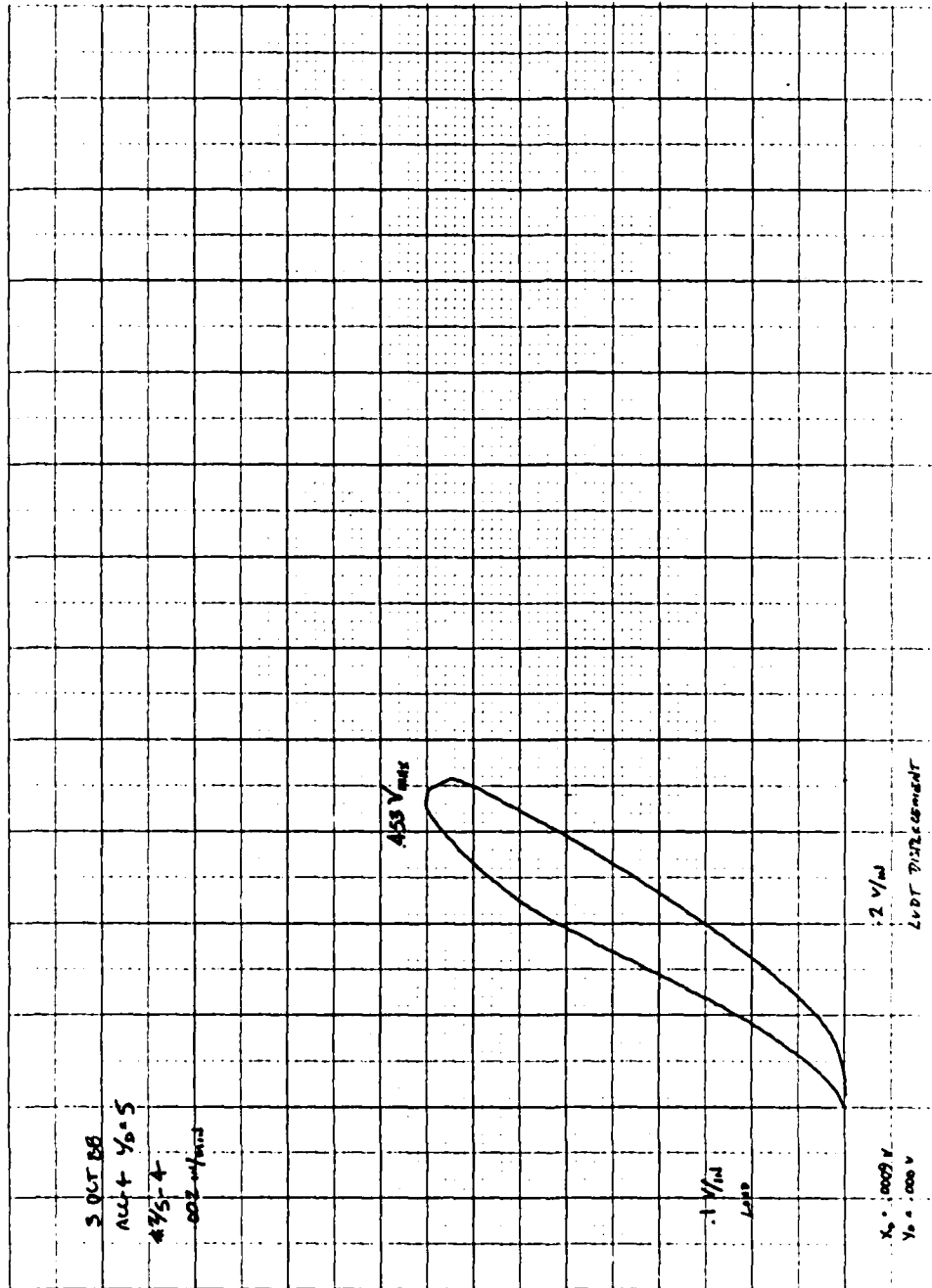


Figure 54. Load-Displacement Curve, Specimen 2/5-4, R=100%

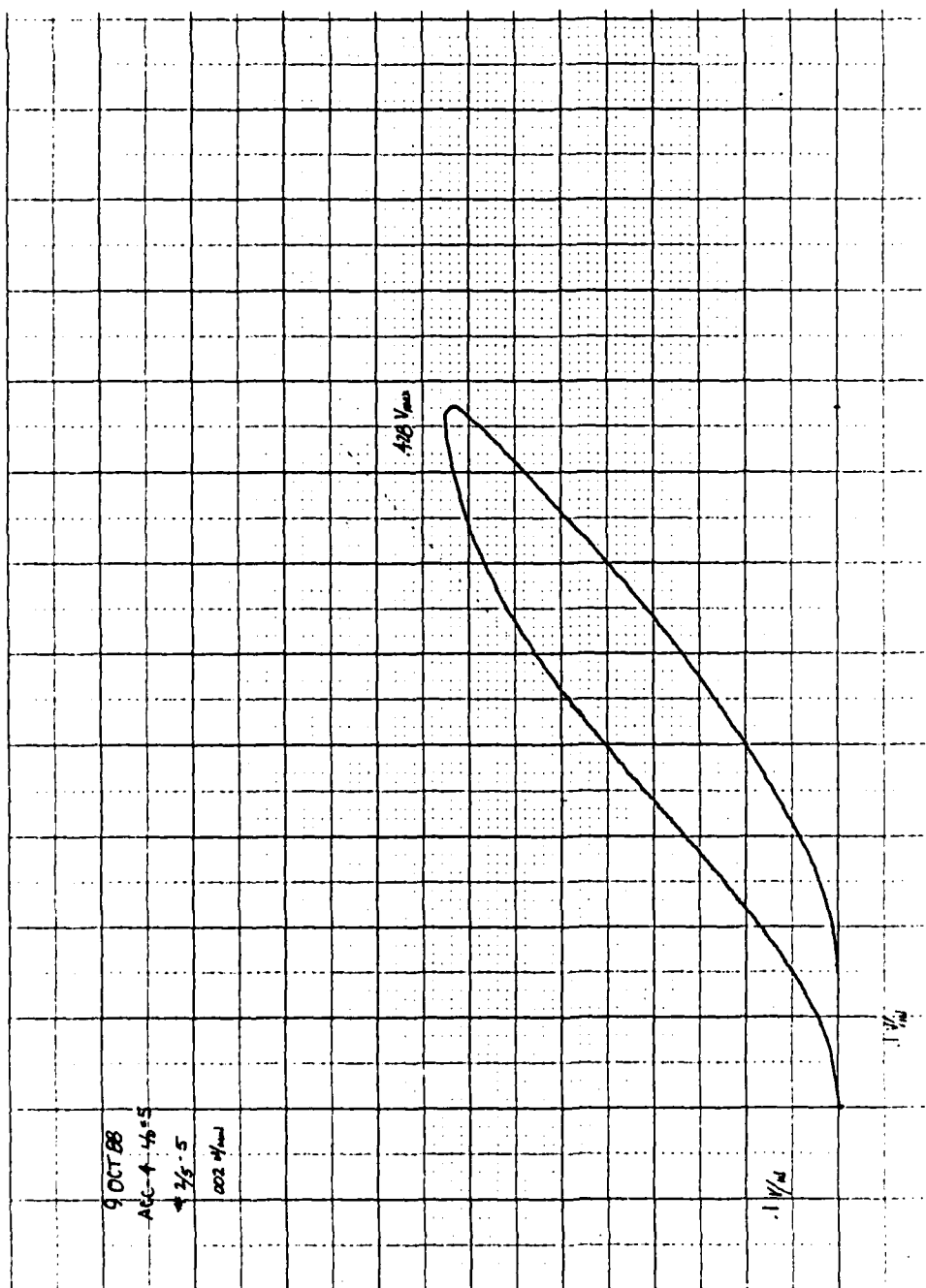


Figure 55. Load-Displacement Curve, Specimen 2/5-5, R=100%

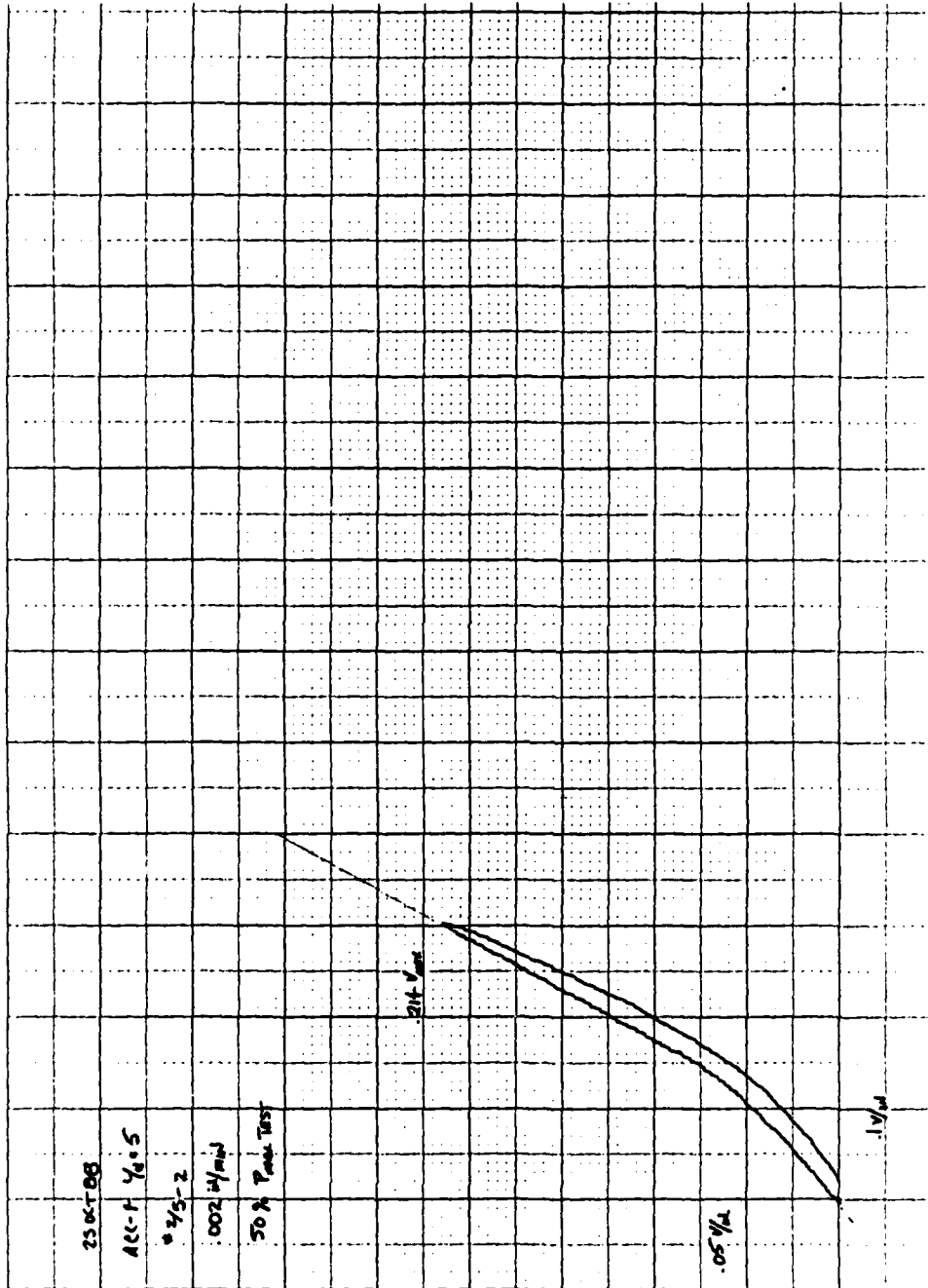


Figure 56. Load-Displacement Curve, Specimen 2/5-2, R=50%

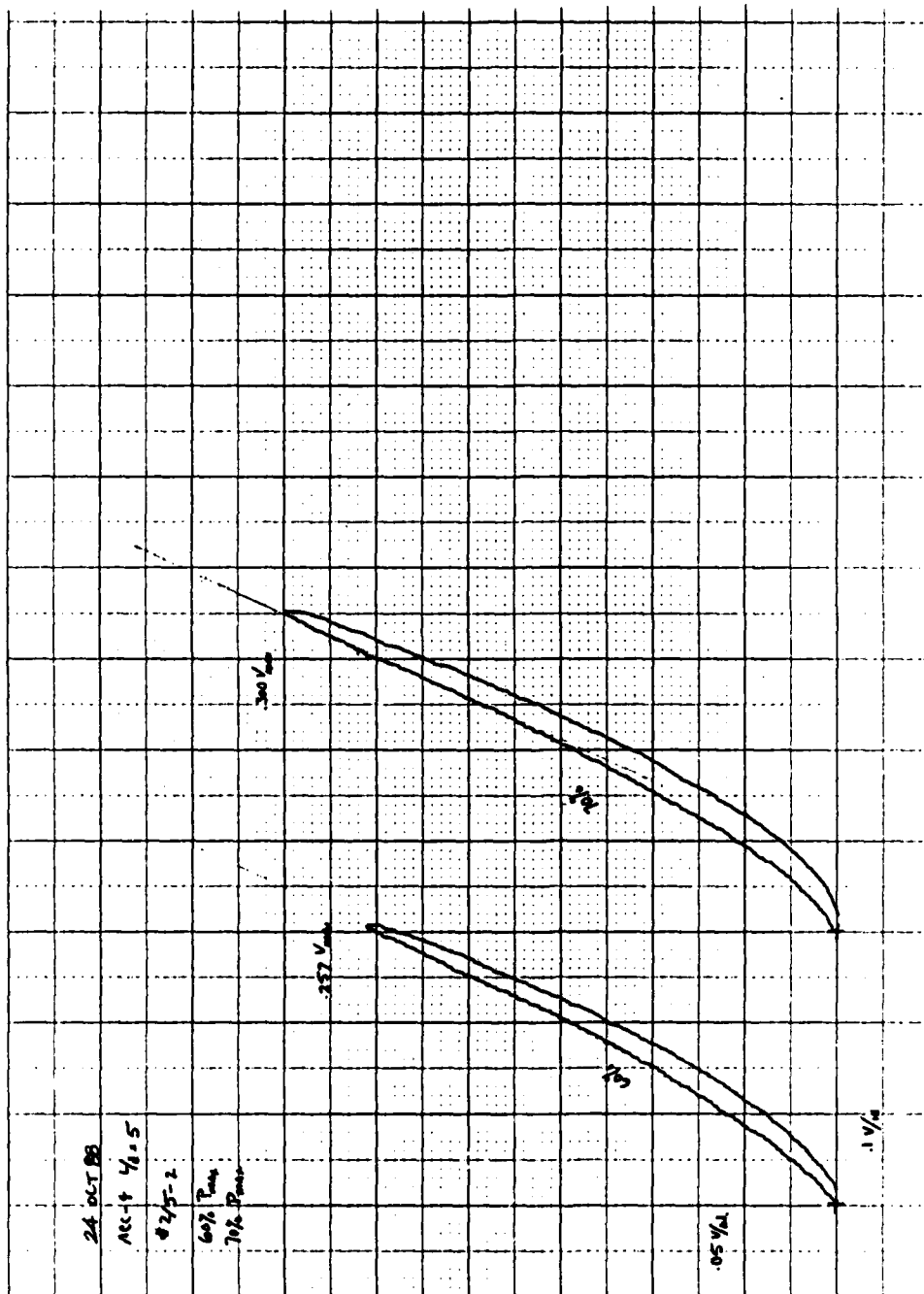


Figure 57. Load-Displacement Curve, Specimen 2/5-2, R=60%, 70%

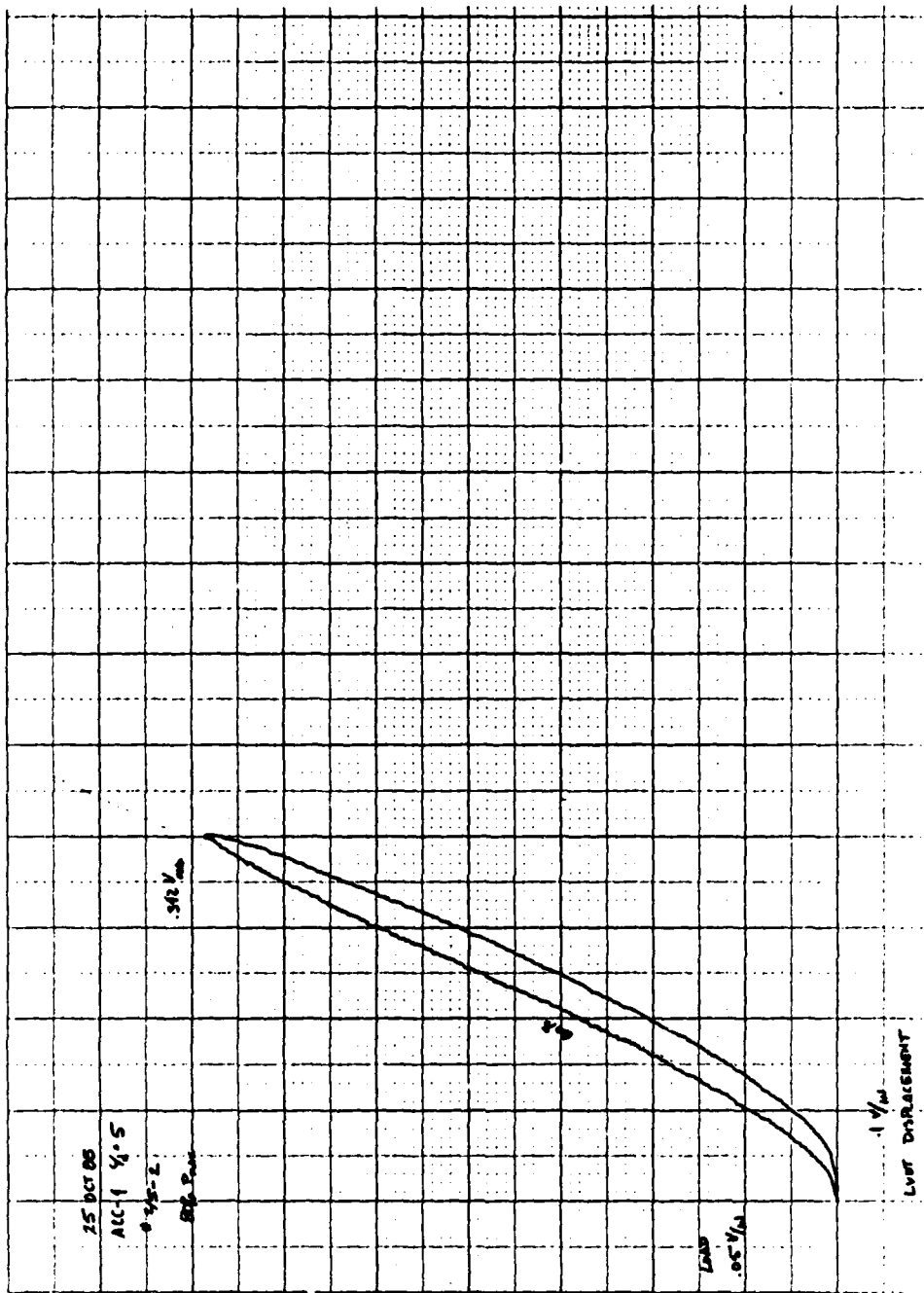


Figure 58. Load-Displacement Curve, Specimen 2/5-2, R=80%

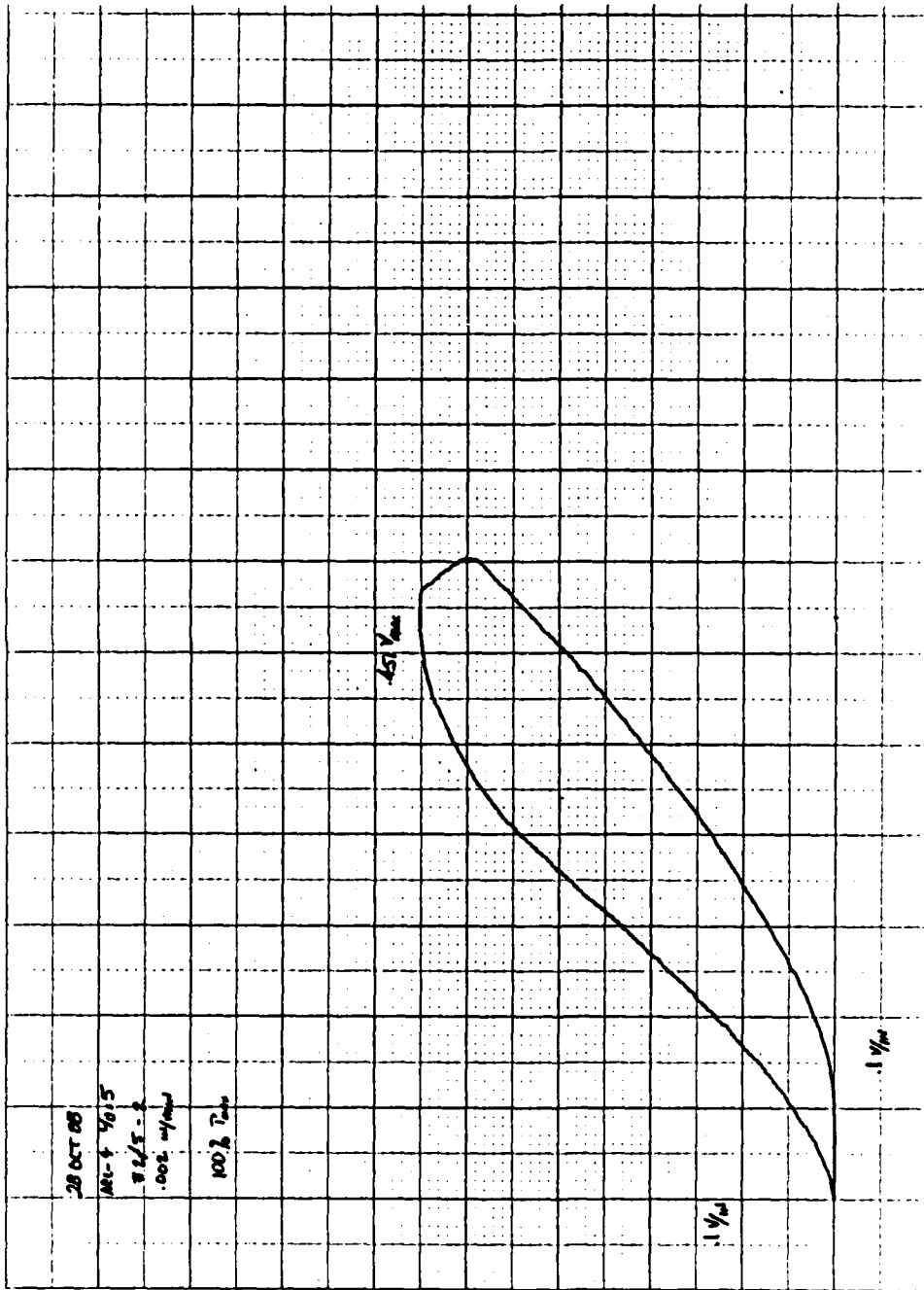


Figure 59. Load-Displacement Curve, Specimen 2/5-2, R=100%

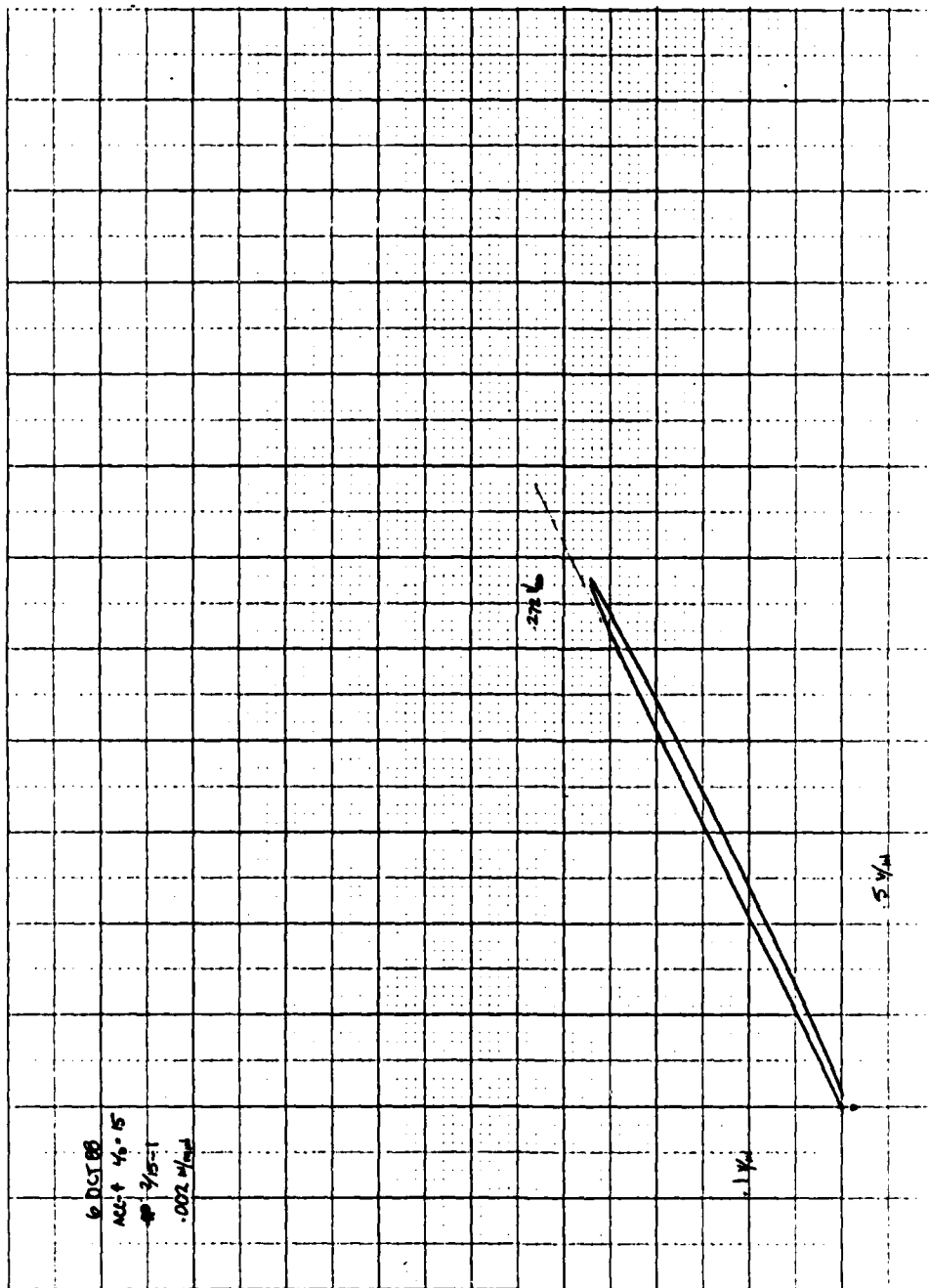


Figure 60. Load-Displacement Curve, Specimen 2/15-1, R=100%

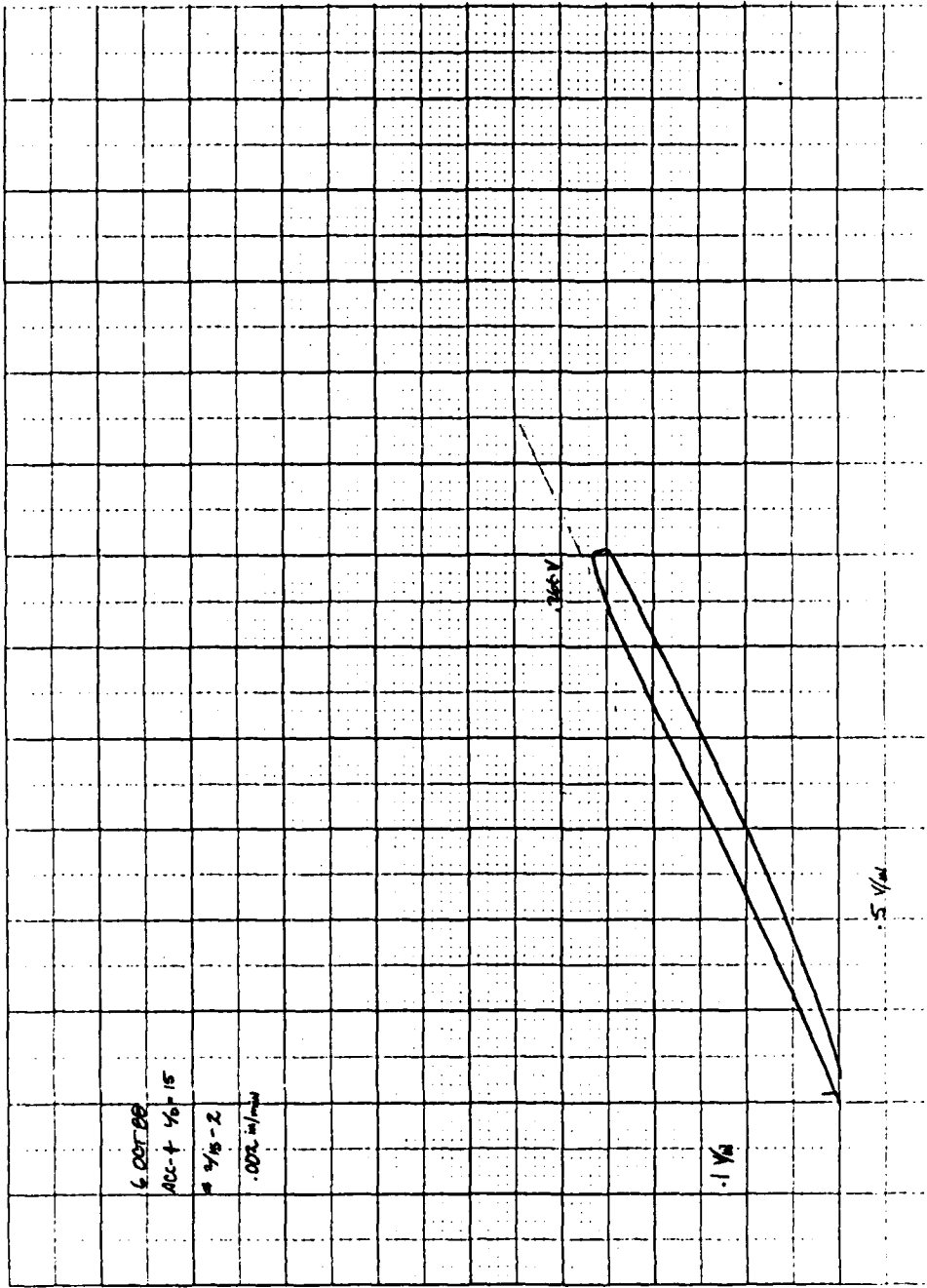


Figure 61. Load-Displacement Curve, Specimen 2/15-2, R=100%

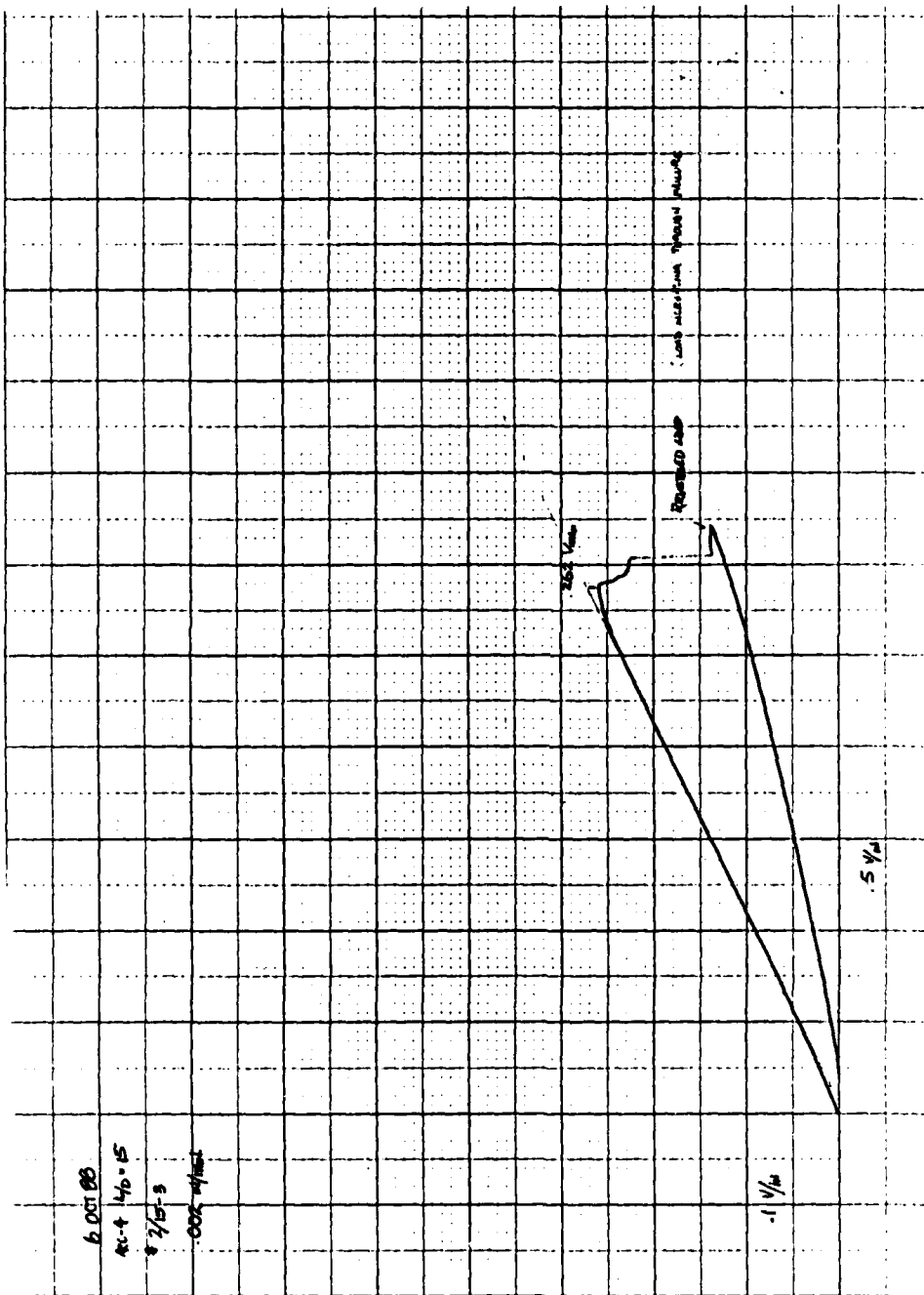


Figure 62. Load-Displacement Curve, Specimen 2/15-3, R=100%

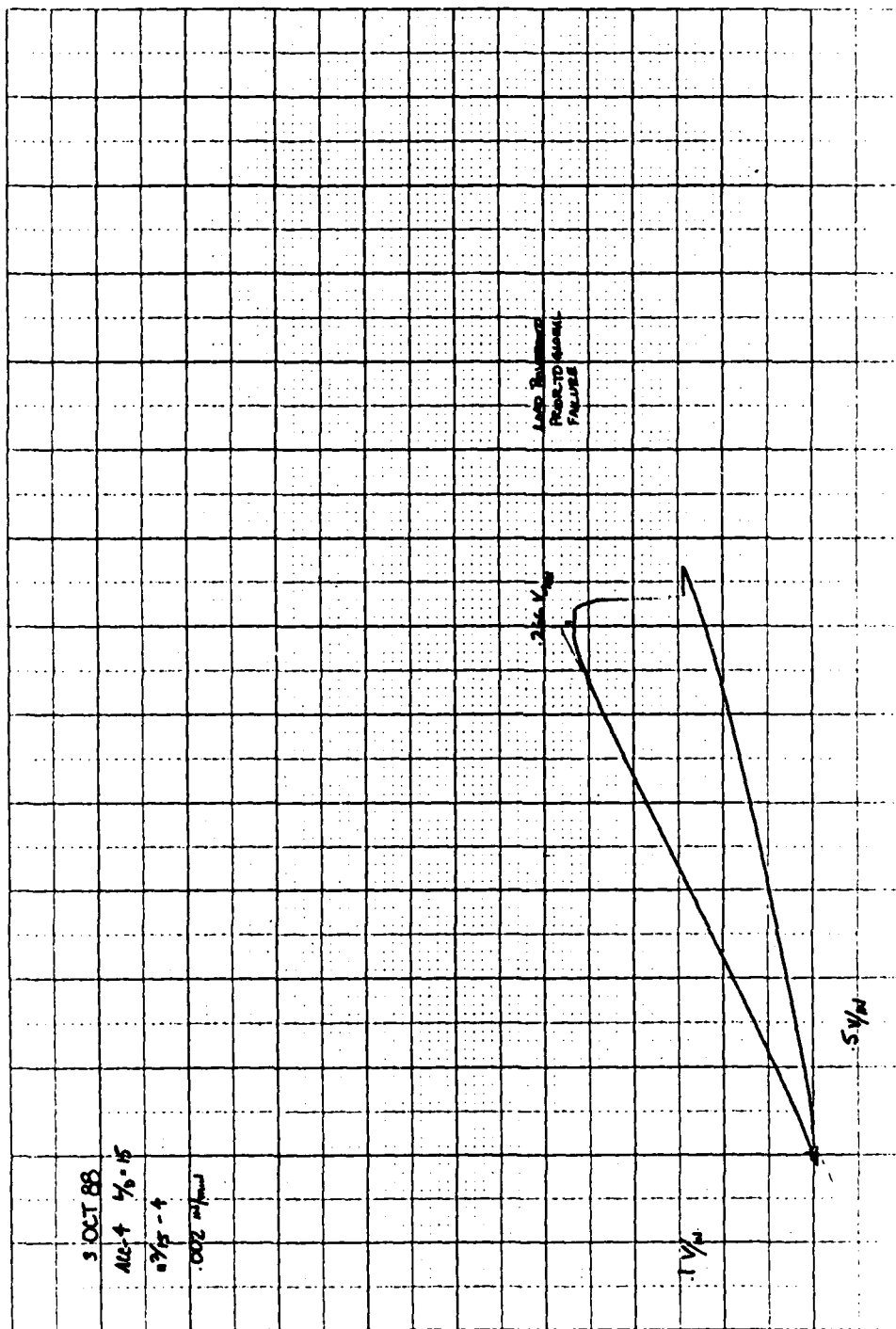


Figure 63. Load-Displacement Curve, Specimen 2/15-4, R=100%

Captain James C. Dendis [REDACTED]  
[REDACTED]  
[REDACTED]

[REDACTED] in 1978 [REDACTED] attended the Pennsylvania State University, from which he received the degree of Bachelor of Science in Aerospace Engineering in May, 1982. Upon graduation, he was commissioned in the US Air Force through the Reserve Officer Training Corps. His first assignments were as an Aircraft Structures Engineer, and two years later, Chief of the Aerodynamics and Performance Engineering Section within the Directorate of Material Management at the San Antonio Air Logistics Center, Kelly AFB, Texas. During his tour at Kelly AFB, he completed Squadron Officer School both by correspondence, and in residence at Maxwell AFB, Alabama. He was transferred to Wright-Patterson AFB and entered the School of Engineering, Air Force Institute of Technology, in June of 1987.

[REDACTED]  
[REDACTED]

AD A 363 617

REPORT DOCUMENTATION PAGE

Form Approved  
OMB No. 0704-0188

1a. REPORT SECURITY CLASSIFICATION UNCLASSIFIED		1b. RESTRICTIVE MARKINGS	
SECURITY CLASSIFICATION AUTHORITY		3. DISTRIBUTION / AVAILABILITY OF REPORT Approved for public release; Distribution Unlimited.	
2b. DECLASSIFICATION / DOWNGRADING SCHEDULE		5. MONITORING ORGANIZATION REPORT NUMBER(S)	
4. PERFORMING ORGANIZATION REPORT NUMBER(S) AFIT/GAE/AA/88D-7		7a. NAME OF MONITORING ORGANIZATION AF Aero Propulsion Laboratory AF Wright Aeronautical Labs	
6a. NAME OF PERFORMING ORGANIZATION School of Engineering	6b. OFFICE SYMBOL (If applicable) AFIT/ENY	7b. ADDRESS (City, State, and ZIP Code) AFWAL/POTA Wright-Patterson AFB, OH 45433-6563	
6c. ADDRESS (City, State, and ZIP Code) Air Force Institute of Technology (AU) Wright-Patterson AFB, OH 45433-6583		9. PROCUREMENT INSTRUMENT IDENTIFICATION NUMBER Advice No. 88HS174	
8a. NAME OF FUNDING / SPONSORING ORGANIZATION AF Aero Propulsion Lab	8b. OFFICE SYMBOL (If applicable) AFWAL/POTA	10. SOURCE OF FUNDING NUMBERS	
8c. ADDRESS (City, State, and ZIP Code) AFWAL/POTA Wright-Patterson AFB, OH 45433		PROGRAM ELEMENT NO. 62203F	TASK NO. 3066
		WORK UNIT ACCESSION NO. 12	28
11. TITLE (Include Security Classification) (see block 19)			
12. PERSONAL AUTHOR(S) James C. Dendis, Captain, USAF			
a. TYPE OF REPORT MS Thesis	13b. TIME COVERED FROM _____ TO _____	14. DATE OF REPORT (Year, Month, Day) 1988, December	15. PAGE COUNT 133
16. SUPPLEMENTARY NOTATION			
17. COSATI CODES		18. SUBJECT TERMS (Continue on reverse if necessary and identify by block number)	
FIELD	GROUP	Carbon-Carbon Composites, Materials (Composite Materials), Failure (Mechanics), Mechanical Properties (Flexural Properties)	
11	04		
19. ABSTRACT (Continue on reverse if necessary and identify by block number)			
TITLE: Damage Initiation in Two-Dimensional, Woven Carbon-Carbon Composites (Unclassified)			
THESIS CHAIRMAN: Paul D. Copp, Major, USAF Associate Professor of Aeronautical Engineering			
Abstract on Reverse			
20. DISTRIBUTION / AVAILABILITY OF ABSTRACT <input checked="" type="checkbox"/> UNCLASSIFIED/UNLIMITED <input type="checkbox"/> SAME AS RPT. <input type="checkbox"/> DTIC USERS		21. ABSTRACT SECURITY CLASSIFICATION Unclassified	
22a. NAME OF RESPONSIBLE INDIVIDUAL Paul D. Copp, Major, USAF		22b. TELEPHONE (Include Area Code) (513) 255-2632	22c. OFFICE SYMBOL AFIT/ENY

*James C. Dendis*  
12 Jan 1989

19. This thesis examines the failure initiation characteristics of uncoated, 2-D, warp-aligned, ACC-4 Carbon-Carbon Composites in standard three-point bend experiments. ASTM-2344 short beam shear tests were run on specimens with a span-to-depth ratio of four, five, and fifteen. Failure load and indications of failure initiation were recorded on a load-displacement curve. Actual specimen mid-span displacement was recorded instead of the usual cross-head displacement. Specimens were micro photographed for pre- and post-test comparisons. Halftone reproductions of the photographs are included to show similarities and differences in failures of the various length specimens. A linear elastic NASTRAN™ finite element model was used to predict the global stress field. Displacements predicted by this model are within 5% of mean experimental values. Failure initiation sites and loads were predicted with contour plots of the Tsai-Wu and Tsai-Hill failure criteria. This model predicts failure initiation at loads near 50% of maximum load in the short specimens. A series of increasing step load tests were run to collect photos of specimen damage at loads less than maximum. The results are consistent with model predictions with initial damage occurring at 45% of max load in the short beam. (Unclassified)

(20/1/85)